FINAL REPORT

Structural Integrity Assessment Using Laser Measured Surface Vibration

SERDP Project SI-1655

April 2009

Dr. J.A. Bucaro
SET, Inc at Navy Research laboratory

Strategic Environmental Research and Development Program

This report was prepared under contract to the Department of Defense Strategic Environmental Research and Development Program (SERDP). The publication of this report does not indicate endorsement by the Department of Defense, nor should the contents be construed as reflecting the official policy or position of the Department of Defense. Reference herein to any specific commercial product, process, or service by trade name, trademark, manufacturer, or otherwise, does not necessarily constitute or imply its endorsement, recommendation, or favoring by the Department of Defense.

REPORT DOCUMENTATION PAGE	Form Approved OMB No. 0704-0188

The public reporting burden for this collection of information is estimated to average 1 hour per response, including the time for reviewing instructions, searching existing data sources, gathering and maintaining the data needed, and completing and reviewing the collection of information. Send comments regarding this burden estimate or any other aspect of this collection of information, including suggestions for reducing the burden, to Department of Defense, Washington Headquarters Services, Directorate for Information Operations and Reports (0704-0188), 1215 Jefferson Davis Highway, Suite 1204, Arlington, VA 22202-4302. Respondents should be aware that notwithstanding any other provision of law, no person shall be subject to any penalty for failing to comply with a collection of information if it does not display a currently valid OMB control number.
PLEASE DO NOT RETURN YOUR FORM TO THE ABOVE ADDRESS.

1. REPORT DATE *(DD-MM-YYYY)*	2. REPORT TYPE	3. DATES COVERED *(From - To)*
18-12-2008		01-Jan-08 to 18-Dec-08

4. TITLE AND SUBTITLE	5a. CONTRACT NUMBER
Structural Integrity Assessment Using Laser Measured Surface Vibration	5b. GRANT NUMBER
	5c. PROGRAM ELEMENT NUMBER
6. AUTHOR(S)	5d. PROJECT NUMBER
J.A. Bucaro, A.J. Romano, S.Dey, P. Herdic, B.H. Houston, D. Amon	5e. TASK NUMBER
	5f. WORK UNIT NUMBER

7. PERFORMING ORGANIZATION NAME(S) AND ADDRESS(ES)	8. PERFORMING ORGANIZATION REPORT NUMBER
Naval Research Laboratory Washington, DC 20375-5350	
9. SPONSORING/MONITORING AGENCY NAME(S) AND ADDRESS(ES)	10. SPONSOR/MONITOR'S ACRONYM(S)
SERDP 901 North Stuart Street Suite 303 Arlington, VA 22203	11. SPONSOR/MONITOR'S REPORT NUMBER(S)

12. DISTRIBUTION/AVAILABILITY STATEMENT

Unlimited Public Distribution

13. SUPPLEMENTARY NOTES

14. ABSTRACT

This SERDP SEED Project was focused on extending the applicability of the NRL-developed structural acoustic fault monitoring technique using laser measured surface vibration to the materials and fabrics associated with historic buildings. In this regard, flexural wave inversion was successfully demonstrated numerically on thin plates of plaster, steel, and concrete and on thick plaster and steel plates with flaws at different depths. A new orthotropic inversion algorithm was developed and demonstrated on a similarly generated numerical data base on a wood slab. Two novel adaptive inversion approaches were developed and demonstrated, one using the flexural wave and generalized force algorithms sequentially, and the other based on high order equations of motion with unknown coefficients. A finite element-based study of a plaster dome ceiling with a detached section and a deconsolidated inclusion was carried out using acoustic speaker excitation. A model was developed for predicting flaw size detectability and for generalizing to other ceiling conditions. A new conformal spatial transform was developed and applied to the elliptical dome ceiling showing marked differences in the wave-number spectra associated with the two flaw types. Finally, a laboratory demonstration was carried out on a large wooden ceiling support beam in whose interior was created a small, thin cavity filled with sawdust. Direct observation of the band-averaged SLDV scans clearly detected and localized the defect. The orthotropic inversions indicated very large spatial variations in the wood beam elastic properties.

15. SUBJECT TERMS

historic building structural assessment, fault detection and localization

16. SECURITY CLASSIFICATION OF:			17. LIMITATION OF ABSTRACT	18. NUMBER OF PAGES	19a. NAME OF RESPONSIBLE PERSON
a. REPORT	b. ABSTRACT	c. THIS PAGE			Dr. B. H. Houston
U	U	U		72	19b. TELEPHONE NUMBER *(Include area code)* 202-404-3840

Standard Form 298 (Rev. 8/98)
Prescribed by ANSI Std. Z39.18

TABLE OF CONTENTS

I. TABLE OF ACRONYMS 5

II. LIST OF FIGURES 5

III. LIST OF TABLES 8

IV. ACKNOWLEDGEMENTS 9

V. EXECUTIVE SUMMARY 11

VI. OBJECTIVE 15

VII. BACKGROUND 15
- Direct Observation of High Contrast Motion 17
- Local Inversion 17
- Generalized Force Mapping 18
- ω- k Mapping 18
- Previous Success: Assessing Wall Paintings and Underlying Structure at the U.S. Capitol Building 19

VIII. MATERIALS AND METHODS 20
- Differing Materials –Thin and Thick Plates 21
- Orthotropic Wooden Slabs 21
- Adaptive Inversion 21
- Modern Classifiers 22
- Plaster Dome Ceiling: A Numerical Study 22
- Novel Spatial Transform 24
- Laboratory Demonstration 24

IX. RESULTS AND ACCOMPLISHMENTS 24
- Thin and Thick Plates of Various Materials: Numerical Studies at Three Frequencies. 24
  - Isotropic Thin Plates Made of Steel, Concrete, and Plaster. 25
  - Isotropic Thick Plates Made of Steel and Plaster. 29
- Orthotropic Inversion Operators and Application to Wood Slabs 36
  - Orthotropic Inversion 37
  - Orthotropic Generalized Force Mapping 38
  - Wooden Plate Detail 38
  - Finite Element Data Base 39
  - Results 40
- Adaptive Algorithms 45
  - Adaptive GFM by Prior Inversion 45
  - The Fundamental Concept – Adaptive Coefficients 46
  - The Training Criteria 47
- Modern Classifiers 50

Plaster Dome Ceiling 50
Ceiling Structure 51
Numerical Code 51
Ceiling Conditions 52
Analysis & Results 52
Detached Defect 54
Deconsolidation Defect 58
Findings from Ceiling Study 60
Novel Spatial Transforms for Arbitrarily-Shaped Surfaces 61
Laboratory Demonstration 63
Conclusions 69
References: 70

X. Appendices 72

I. TABLE OF ACRONYMS

CFR	Code of Federal Regulations
CGLS	conjugate gradient least squares
DoD	Department of Defense
FFT	fast Fourier transform
GFI	generalized force inversion
GFM	generalized force mapping
HMM	hidden Markov model
ICRMP	integrated cultural resources management plans
ID	identification
KMP	kernel matching pursuits
LDV	laser Doppler vibrometer
MRE	magnetic resonance elastography
NRL	Naval Research Laboratory
RHS	right hand side
RVM	relevance vector machine
SEED	SERDP Exploratory Development
SLDV	scanning laser Doppler vibrometer
SOH	state of health
SON	statement of need
SNR	signal to noise ratio
SPL	sound pressure level
STARS	structural acoustics radiation and scattering
UXO	unexploded ordnance
WFWI	weak flexural wave inversion

II. LIST OF FIGURES

Figure 1. Depiction of the structural acoustic fault monitoring methodology applied to a variety of structures.

Figure 2. (Left) Experimental arrangement for plaster wall assessments at the U.S. Capitol Building showing the SLDV monitoring system, a shaker used to excite the art-laden walls, and

a lap - top computer data acquisition system in the Brumidi Corridor; (Right) a photograph of the President's Room where extensive measurements were made on the walls and ceiling.

Figure 3. A comparison of the faults found by our structural acoustic technique (left) and by a tap test (right) in a fresco panel in the Brumidi Corridor of The U.S. Senate.

Figure 4. Co-ordinate system and plate geometry used in the finite element calculations of normal surface displacement for point excited plates with and without an internal flaw.

Figure 5. Numerically generated displacements at 1, 5, and 10 kHz and flexural wave inversions for thin plaster plates with flaw and no flaw.

Figure 6. Numerically generated displacements at 1, 5, and 10 kHz and flexural wave inversions for thin concrete plates with flaw and no flaw.

Figure 7. Numerically generated displacements at 1, 5, and 10 kHz and flexural wave inversions for thin steel plates with flaw and no flaw.

Figure 8. Cross section of thick plate showing flaws at three different depths

Figure 9. Numerically generated displacements at 1 kHz and flexural wave inversions for thick steel plates with no flaw and flaws at three different depths.

Figure 10. Numerically generated displacements at 5 kHz and flexural wave inversions for thick steel plates with no flaw and flaws at three different depths.

Figure 11. Numerically generated displacements at 10 kHz and flexural wave inversions for thick steel plates with no flaw and flaws at three different depths.

Figure 12. Numerically generated displacements at 1 kHz and flexural wave inversions for thick plaster plates with no flaw and flaws at three different depths.

Figure 13. Numerically generated displacements at 5 kHz and flexural wave inversions for thick plaster plates with no flaw and flaws at three different depths.

Figure 14, Numerically generated displacements at 10 kHz and flexural wave inversions for thick plaster with no flaw and flaws at three different depths.

Figure 15. Wooden plate and Cartesian axes system.

Figure 16. Calculated color-coded surface displacement at 5 kHz and 10 kHz when the shaker in the lower left position is excited at each frequency.

Figure 17. Result of applying weak flexural wave inversion operator (WFWI) developed for the isotropic case, Eq. (5), to the displacement data (lower left driver excited) at each frequency for both the homogeneous wooden plate and the flawed wooden plate.

Figure 18. Result of applying the weak flexural wave inversion operator (WFWI) developed for the orthotropic case, Eq. (11), to the displacement data at each frequency for the homogeneous wooden plate to obtain the three stiffness parameters $D_x/\rho h$, $D_{xy}/\rho h$, and $D_y/\rho h$.

Figure 19. Result of applying the weak flexural wave inversion operator (WFWI) developed for the orthotropic case, Eq. (11), to the displacement data at each frequency for the flawed wooden plate to obtain the three stiffness parameters $D_x/\rho h$, $D_{xy}/\rho h$, and $D_y/\rho h$.

Figure 20. Result of applying the generalized force mapping operator (GFM) developed for the orthotropic case, Eq. (12), to the displacement data at each frequency for the homogeneous and flawed wooden plates when the driver in the lower left is excited.

Figure 21. Result of applying the generalized force mapping operator (GFM) developed for the orthotropic case, Eq. (12), to the displacement data at each frequency for the homogeneous and flawed wooden plates when the driver in the lower left is excited.

Figure 22. Adaptive algorithm chooses correct shear wave equation upon locally sampling 2-D slice of internal displacement map measured in Agar using magnetic resonance elastography.

Figure 23. Adaptive algorithm chooses correct isotropic plate wave equation upon locally sampling surface displacement map computed by finite element model.

Figure 24. Adaptive algorithm chooses correct orthotropic plate wave equation upon locally sampling surface displacement map computed by finite element model.

Figure 25. (a) the geometry of the elliptical ceiling and location of the acoustic source (viewed from beneath the ceiling); (b) the boundary conditions assumed in the finite element calculation; (c) the mesh used in conjunction with the hp-finite element code (viewed from above the ceiling).

Figure 26. (a) the geometry of the defect (plan view from above the ceiling). The insert shows a circular flaw having the same area as the pie-shaped flaw; (b) the boundary conditions for the ceiling with detached defect; (c) the boundary conditions for the ceiling with deconsolidated defect.

Figure 27. Normal displacement levels for the unflawed ceiling calculated with the STARS3D code for four frequencies (displayed on the exposed surface of the ceiling).

Figure 28. Surface pressure levels for a perfectly rigid elliptical ceiling calculated with the STARS3D code for four frequencies (displayed on the exposed surface of the ceiling).

Figure 29. The ratio of detached flaw displacement to that of the healthy ceiling versus the circular flaw radius computed from the static expression of Eq. (25) for three plaster thicknesses.

Figure 30. The resonance frequency versus circular flaw radius computed using Eq. (27) based on a lumped parameter model for two plaster thicknesses.

Figure 31. Normal displacement levels for the flawed ceiling (detached segment) calculated with the STARS3D code for four frequencies (displayed on the exposed surface of the ceiling).

Figure 32. Normal displacement levels for the flawed ceiling in an area around the flaw calculated with the STARS3D code for four frequencies (displayed on the exposed surface of the ceiling): (a) detached flaw; (b) deconsolidated flaw.

Figure 33. New spatial transform applied to the detached ceiling flaw.

Figure 34. New spatial transform applied to the deconsolidated ceiling flaw.

Figure 35. Drawing of beam with faults, shaker, and scan area locations. This view is from SLDV side. Shakers actually mounted on backside of beam.

Figure 36. Laboratory study of flawed wooden support beam. Scanning laser Doppler vibrometer shown in background. Dynamic shaker mounted on upper right corner of beam. Larger interior flaw depicted by rectangle drawn on beam.

Figure 37. Polytec Inc. PSV-400 laser Doppler vibrometer scanning head.

Figure 38. Normal surface velocity ((m/s)/N) magnitude displays at 431.25 Hz, 1260.94 Hz, and 7162.50 Hz. The horizontal dimension is along the length of the flawed beam and the vertical dimension is across the width of flawed beam

Figure 39. Band averaged displacements. Lower display is average over complete band; Upper display is average over resonance band. The defect centered at about scan point 80 is clearly evident in both maps.

Figure 40. Direct displacement at 7900 Hz showing flaw.

Figure 41. Displacement (left) and filtered displacement (middle) for the three shaker positions. Orthotropic inversion of displacement data for (right) for $D_x/\rho h$, $D_{xy}/\rho h$, and $D_y/\rho h$ on top, center, and bottom, respectively.

III. LIST OF TABLES

Table 1: Plate Material Parameters

Table 2: Nine independent stiffness matrix elements for Douglas fir (10^8 Pa).

Table 3. Dynamic Displacements, Total Force Acting on Flaw, and Wavelengths

IV. ACKNOWLEDGEMENTS

We are grateful to the Department of Defense's Strategic Environmental Research and Development Program (SERDP) for providing the funding for this project which enabled us to undertake this project. Appreciation for technical assistance is extended to Dr. John Hall, Sustainable Infrastructure Program Manager and to the HydroGeoLogic, Inc., staff for their administrative assistance.

This project was carried out as a joint effort among three organizations.

Principal Investigator:	Dr. Joseph A. Bucaro, SET, Inc. as an on-site contractor at the Naval Laboratory
Associate Investigators:	Dr. Anthony J. Romano, the Naval Research Laboratory
	Dr. Saikat Dey, Global Strategies Group (North America), Inc. as an on-site contractor at the Naval Research Laboratory
	Dr. Peter H. Herdic, Global Strategies Group (North America), Inc. as an on-site contractor at the Naval Research Laboratory
	Dr. Brian H. Houston, the Naval Research Laboratory
	Mr. Dan Amon, Global Strategies Group (North America), Inc. as an on-site contractor at the Naval Research Laboratory

V. EXECUTIVE SUMMARY

This SEED Project was focused on extending the applicability of the NRL-developed structural fault monitoring technique using laser measured surface vibration to the materials and fabrics associated with historic buildings. The DoD controls an estimated 90,000 buildings and structures that were built over 60 years ago. In accordance with federal statutes, federal agencies make every effort to rehabilitate historically significant buildings and structures, whenever possible. Prior to initiating a rehabilitation project, project managers may undertake a study to determine the conditions of the various buildings, features, and finishes, including heating, plumbing, and structural elements. Developing a toolkit of nondestructive methods to "look behind the walls" of historic and under-documented structures would provide necessary data to make real-time decisions for cost effective management options.

In this vibration monitoring, structural acoustics- based approach, the dynamic surface displacements of a structure caused by very weak externally produced forces (acoustic speakers or shakers) are spatially and spectrally mapped with a scanning laser Doppler vibrometer (SLDV). A number of inversion algorithms developed at NRL are then used to invert these spatial vibration scans into various material parameter maps which then serve to locate subsurface faults.

In this SEED program we carried out a one year program of research aimed at providing proof of concept related to extension of this approach to more general structures and faults. Demonstrating proof of concept of the applicability of this structural acoustic/SLDV/inversion algorithm technology beyond that already demonstrated for plaster walls would address directly the Statement of Need (SON) for the Sustainable Infrastructure (SI) Seed New Start. It would provide new techniques for effectively and efficiently assessing the structural integrity of the fabric of historic buildings and structures in non-invasive, non-destructive manners.

Our objectives were to:

1. Extend our structural acoustic/SLDV/inversion technique by developing advanced inversion algorithms. This would allow monitoring of faults at various depths and determination of depth dependences, more accurate physical description of the flawed region, and application to non-planar geometries and general materials. Such advanced algorithms would include adaptive inversion algorithms which do not require a-priori information regarding the equations of motion of the structure being probed and identification algorithms which utilize new spatial transforms and modern day classifiers.
2. Assess the efficacy of applying these new techniques to various parts of a building fabric or structure including those fabricated from concrete, brick, masonry, iron, steel, wood, etc.
3. Demonstrate proof of concept in the laboratory.

In determining the feasibility for extending our SLDV/inversion approach augmented with new developments to various parts of a building fabric and structure including those fabricated from concrete, steel, wood, etc., a study was carried out using a numerically generated vibration data base using advanced h-p adaptive, finite element–based structural acoustic codes developed in our group in other programs. The isotropic structures for which numerical data was generated included: (1) thin plates of plaster, steel, and concrete; (2) thick plates of plaster and

steel wherein flaws at three depths could be studied; and (3) a slab of wood with internal flaws. The first two cases were successfully handled using the isotropic flexural wave inversion algorithms. The last case is much more complex than the previous materials in that the wood is orthotropic.

In the case of wood, we had to take into account the orthotropic nature of the material. In particular, we explored the extension of these inversion algorithms to the orthotropic thin plate case by developing a *variational* form of the differential equation for transverse bending and solving for the orthotropic flexural rigidities. As expected, operation of the original isotropic algorithms on the wooden plate surface displacements was shown to fail in recovering the uniform elastic parameters or in detecting and locating the fault. The new algorithms based on the wave equation for a thin, *orthotropic* plate successfully converted the surface displacements on the uniform wooden plate to the correct elastic parameter maps which then served to detect and localize the inclusion in the flawed plates. The results at the higher frequency indicate that the onset of failure in the thin plate approximation is impacting both the inversion and the generalized force mapping accuracy. However, in this case use of the inversion algorithm to obtain modified wave equation coefficients followed by operation of the force mapping algorithm with these new parameters inserted is shown to successfully mitigate this effect.

Current algorithms which invert measured vibration maps into internal elastic parameters require knowledge of the equations of motion appropriate for the structure under study which restricts their areas of application. Using our extensive experience in the development of inversion algorithms, we addressed the development of novel training algorithms for fault detection which do not depend on a-priori knowledge of the structural equations of motion or the related parameters.

In one such adaptive approach, we explored the idea of cascading various algorithms. One promising approach applied to thick plate structures used the flexural inversion operator appropriate to thin plates. The “effective” stiffness parameters so obtained were then inserted into the generalized force equation method which locates regions with non-zero forces and identifies those as faults. This “adaptive” approach was shown to be very successful.

In a second approach, we defined a set of differential equations which have arbitrary coefficients that multiply sets of spatial and temporal derivatives of the measured displacements. In this formulation, the equations appear as homogeneous sets of partial differential equations whose coefficients are generally unknown, yet which can be “trained”" for any particular structure. Therefore, given a sufficient number of measurements on a control section, the coefficients can be determined, thereby “training” the algorithm to detect fluctuations due to material parameter or structural differences. As with our previous inversion techniques, the trained algorithm would also provide *local* properties thus providing locations of any faults. Further, we explored validation criteria for this adaptive coefficient approach based on the fact that the coefficients associated with the most appropriate solution should have a minimum variance normalized by the mean square value. Initial studies utilizing earlier data demonstrate that this algorithm is robust in the presence of noise and should be adaptable to many situations in fault detection and material parameter variation. In particular, we used three existing data sets for proof of concept: interior displacements maps on agar tissue phantoms taken with magnetic

resonance elastography and surface displacement maps on steel plates and on wooden slabs generated numerically.

A fourth area we explored albeit briefly involved exploiting modern identification (ID) algorithms that use the unique feature spaces derived from the previously described algorithms. The Physical Acoustics Branch has extensive experience in applying such ID algorithms in our on-going work on underwater mine and UXO identification. These algorithms include hidden Markov models (HMM), relevance vector machines (RVM), and kernel matching pursuits (KMP). We expected that application of these algorithms as well as fusion of their modalities might provide both improved performance for fault detection and material parameter determination as well as determination of depth profiles of faults or material parameter fluctuations. Due to time constraints, this effort was not completed.

A fifth area we explored involved plaster domed ceilings. In a number of the truly historic buildings whose finish layers often consist of plaster, walls and/or ceilings often bear precious artwork such as mosaic or frescoed images. In the case of the latter, where the paintings were created on wet plaster, the current physical and mechanical condition of the plaster layer(s) determines for the most part the near to mid term viability of the artwork. Particularly for the case of a ceiling, the development of defects can eventually lead to catastrophic failure of the plaster ceiling and the unrecoverable loss of priceless artwork. In the SEED study, we used a simulated data base of surface vibration generated using an advanced structural acoustic finite element-based code. In particular, we explored application of the speaker-based technique to what we consider to be a generic domed ceiling – a common structure found in historic buildings and residences - in which a plaster layer is attached to, and takes the shape of, a backing structure considered to be relatively rigid such as brick or mortar. Aided by static analysis, we addressed the effectiveness of using the "measured" surface displacements resulting from acoustic speaker excitation to detect and localize two different defect types: (A) detachment of the plaster layer from the supporting brick or mortar, and (B) an internal region in the plaster which has become deconsolidated. Specific questions we wished to resolve include: (1) Is acoustic excitation effective at producing readily measured surface displacements which could be used in detecting these flaws? (2) In general, what issues and/or benefits are introduced by using acoustic speaker versus force actuator excitation? (3) Are typical defects of the type mentioned above detectable by straightforward observation of the acoustically excited spatial displacement maps and how does this depend on flaw size and ceiling thickness? (4) What is the minimum detectable defect size? And (5) if a defect is detected, might one be able to differentiate between detachment and deconsolidation?

The plaster dome ceiling study was very productive. We have provided the first (to our knowledge) models allowing one to predict flaw size detectability or to generalize to different conditions for our general surface vibration approach. We have demonstrated that even relatively small defects result in large displacement levels which stand out against those of the healthy plaster and that even away from defect resonances, practical levels of speaker excitation produce easily measured defect surface vibration. Defects as small as 0.07 m (2a for the circular defect) should have displacement levels which are detectable with commercially available laser vibrometers. Unlike the use of locally applied shaker excitation, when using speakers the architectural acoustics of the room (walls and ceilings) must be taken into account. In the

frequency range studied here, we found that the spatial (wave-number) structure in the displacement maps beneath the defect may provide a wavenumber-based feature which could separate plaster detachment from the other types of defects such as deconsolidation.

A sixth area we explored is based on our new ideas in novel transform methods in structural and physical acoustics. Presently, Fourier decompositions of spatial vibrations are in practice restricted to surfaces defined by separable geometry systems for a meaningful interpretation of their spectra. In our new technique, we define and develop a purely local spectral analysis approach which uses spatially conformal Fourier decompositions. This allows us to analyze dispersion behavior on any surface or structure irrespective of its shape. This leads to an important augmentation of our ω - k mapping[5] technique in which local differences in the dispersion curves from those observed or expected in unflawed structures indicate variations in wave types or in their speeds which are directly related to material parameter variations associated with the development of flaws. We also anticipate that this new transform approach will lead to heretofore unexploited spectral features for classification and vibration analysis. In particular, we applied this new technique to fault identification on an elliptical plaster dome ceiling in order to differentiate defect types.

Finally, we carried out a successful laboratory-based SLDV demonstration on a generic structure as an additional demonstration of proof of concept and efficacy of this overall approach. The structure chosen was a long 2” × 10” ceiling support beam in which was created a 2” × 2.5” × 5/8” thick internal defect at its mid-plane which approximated decay or termite-like damage to the wood. Broadband SLDV scans were obtained across the available surface of the structure providing dynamic displacement fields in the usual manner. These data bases were analyzed in two ways. First, the displacement maps were examined without any inversion to determine if the defect was observable by direct observation of the contrast in the spatially mapped displacements. This was indeed found to be the case in that the internal defect displacements were more than 15 dB above the normal wood displacements. Secondly, the displacement measurements were operated on by the various processing algorithms developed in the program. These inversion operators indicated that the wooden beam had considerable variations in its spatial properties, and this is under further investigation.

Overall, we met our program objectives and in some areas went beyond what we had originally intended. The results of this effort clearly demonstrate the viability and utility of applying the laser-based structural acoustic health monitoring technique to structural integrity assessment work in historic buildings.

VI. OBJECTIVE

The Physical Acoustics Branch at the Naval Research Laboratory (NRL) has made significant progress in what we call "Fault Detection and Localization Using Laser-Measured Surface Vibration." In this structural acoustics- based approach[1,2], the dynamic surface displacements of a structure caused by very weak externally produced forces (acoustic speakers or shakers) are spatially and spectrally mapped with a scanning laser Doppler vibrometer (SLDV). A number of inversion algorithms developed at NRL are then used to invert these spatial vibration scans into various material parameter maps which then serve to locate subsurface faults. In one particularly exciting and relevant application of this approach, we carried out exploratory studies in the U.S. Capitol Building to evaluate the ability of our techniques for assessing the integrity of fresco-bearing plaster walls and ceilings in various rooms of the Senate and the House. Each of these regions contains expansive areas of precious frescoes painted on the plaster walls and ceilings by the artist Constantino Brumidi during the middle decades of the 19th century. The frescoes were painted on wet plaster typically three layers thick. In this pilot program, we were able to locate many fault areas of various sizes related to plaster deconsolidation, layer delamination, and loss of attachment to the supporting mortar structure. Some of these results were recently described in an award winning publication[3] in the Association for Preservation Technology's scientific journal.

In this SEED program we carried out a one year program of research aimed at providing proof of concept related to extension of this approach to more general structures and faults. Demonstrating proof of concept of the applicability of this structural acoustic/SLDV/inversion algorithm technology beyond that already demonstrated for plaster walls would address directly the Statement of Need (SON) for the Sustainable Infrastructure (SI) Seed New Start. It would provide new techniques for effectively and efficiently assessing the structural integrity of the fabric of historic buildings and structures in non-invasive, non-destructive manners.

Our objectives were to:

1. Extend our structural acoustic/SLDV/inversion technique by developing advanced inversion algorithms. This would allow monitoring of faults at various depths and determination of depth dependences, more accurate physical description of the flawed region, and application to non-planar geometries and general materials. Such advanced algorithms would include adaptive inversion algorithms which do not require a-priori information regarding the equations of motion of the structure being probed and identification algorithms which utilize new spatial transforms and modern day classifiers.
2. Assess the efficacy of applying these new techniques to various parts of a building fabric or structure including those fabricated from concrete, brick, masonry, iron, steel, wood, etc.
3. Demonstrate proof of concept in the laboratory.

VII. BACKGROUND

The DoD controls an estimated 90,000 buildings and structures that were built over 60 years ago. In accordance with federal statutes, federal agencies make every effort to rehabilitate historically significant buildings and structures, whenever possible. Prior to initiating a

rehabilitation project, project managers may undertake a study to determine the conditions of the various buildings, features, and finishes, including heating, plumbing, and structural elements. These condition assessments are necessary to develop cost effective and timely management plans for heritage assets. Unless a building is so severely deteriorated that structural elements are visible, it may be necessary to remove part of the building's interior or exterior envelope to determine structural integrity. This method, though sometimes necessary, is expensive and damages intact historic materials. Furthermore, results are not always guaranteed. Developing a toolkit of nondestructive methods to "look behind the walls" of historic and under-documented structures would provide necessary data to make real-time decisions for cost effective management options.

Federal buildings and structures must be evaluated for eligibility for the National register of Historic Places as they approach the age , usually 50 years, when eligibility is possible under the terms of 36 CFR Part 60. Evaluation includes a determination of whether the structure has enough historic integrity to convey its significance. Following a determination of eligibility, an evaluation of whether a building can be renovated in an economically and operationally appropriate manner relies heavily on structural assessments. These assessments are part of the preservation requirements of several federal laws and state statutes that are incorporated into Integrated Cultural Resources Management Plans (ICRMP) that are developed and followed for the assessment and preservation of numerous historic buildings and other structures found on most DoD installations. The DoD installation personnel require assessment tools which would allow them to rapidly and effectively assess the conditions of historic structures without damaging them or otherwise affecting the historic nature of the structure.

In response to the need for effective unobtrusive structural health monitoring techniques, we have been exploring the feasibility of structural acoustic techniques for monitoring the mechanical condition of structures. The focus of our structural acoustic development efforts thus far can be summarized by the following question: Given sufficient but readily accessible displacement information over the surface of a vibrating structure, can we develop and implement corresponding local inversion algorithms for mapping material parameter variations, detecting and localizing flaws (cracks, voids, delaminations, etc.), and uncovering the depth profiles of such. Mechanical fault monitoring using the dynamic response of a structure excited by externally applied forces is not new. For the most part, traditional methods involve some application of modal analysis techniques which typically extract changes in resonance frequencies and/or associated mode shapes. One drawback of such modal approaches results from the fact that local changes in a structure caused by a fault often produce only very small changes in these global modal parameters whereas unavoidable environmental changes can have a large impact on these measured characteristics. In addition, even when modal analysis is used successfully to indicate a structural problem, localization of the detected flaw is in general difficult.

Our focus has been to develop techniques which also use the mechanical dynamic response but that, however, are able to detect and characterize *local* changes in the structural dynamics caused by the presence of a fault. The methodology is illustrated in Fig. 1. Our new methods use measurements of surface displacement associated with vibration of the structure caused by weak externally applied forces. These forces can be created simply by a local actuator in direct contact with the structure or by an incident airborne acoustic wave generated by a

speaker. The measured normal surface displacements, $u_z(x,y)$, are then inverted locally using various mathematically optimized algorithms in order to obtain a desired material parameter - for example, the elastic modulus - whose spatial variation then serves to detect and localize the fault. We choose to rely on surface displacements because these are readily accessible for all materials and most structures using existing scanned sensor technologies such as scanned laser Doppler vibrometry (SLDV).

Figure 1. Depiction of the structural acoustic fault monitoring methodology applied to a variety of structures. Surface displacements are monitored over the area of interest due to structural vibrations induced either by an applied shaker or an acoustic source. The displacements measured over the surface with a commercially available laser Doppler vibrometer are algorithmically inverted to produce a map of a desired material parameter which serves to detect and locate the flaw.

To a large extent, the power of the fault detection techniques pursued here depends on the successful development of a compatible set of inversion algorithms which can operate efficiently and in the presence of noise on the scanned surface displacements of the vibrating structure to produce a meaningful map of some fault-sensitive mechanical parameter. Below we discuss four such approaches with which we have had various degrees of success.

Direct Observation of High Contrast Motion

We have demonstrated that in some cases even relatively small defects result in large displacement levels which stand out against those of the healthy areas of the structure and that typically LDV scans of the surface vibration can serve to detect and localize the defect. This was generally the situation in our work at the Capitol Building to detect and locate defects such as mortar detachment in the plaster walls[1,3].

Local Inversion

In the local inversion approach[4], we seek to invert the equations of motion for the structure. For the vibration of general elastic media at frequency ω, the fundamental equation is given as:

$$\sigma_{ij,j}[\vec{u}] + \rho\omega^2 u_i = f_i \tag{1}$$

where σ_{ij} is the stress, the subscript j denotes the partial derivative with respect to co-ordinates x_j, $\vec{u}$ is the displacement, ρ the density, and $\vec{f}$ the applied force used to vibrate the structure.

Without detailing the mathematics here, in locations away from the applied force, a variational form of the above equation is constructed through multiplication by a smoothly varying "virtual" function having specifically designed boundary conditions and insertion of the relevant relationship between stress and strain. The resulting equation is then inverted to obtain an effective elastic modulus in terms of the measurable displacements, $\vec{u}$. For the case of a plate structure of thickness *h*, Young's modulus *E*, and Poisson ratio υ, the inversion results in the relatively simple relationship

$$M(E, v, \rho, h) = \omega^2 G(u_z) \tag{2}$$

where *M* is the *local* plate stiffness/(ρh) and *G* is an integral function over the surface whose integrand depends upon the measured $u_z\ (x,y)$ and which by design contains no spatial derivatives of *u* beyond the first. This latter property, which results from introduction of the virtual functions, is extremely important because of its ability to greatly reduce the effects of spatially dependent noise on the inversion result. The simple application of Eq. (2) upon the measured displacements can thus provide local mechanical information involving E, v, ρ, and *h*.

Generalized Force Mapping

In contrast to direct inversion, the generalized force mapping technique[4] uses the known values of the elastic moduli, density, and thickness together with the measured displacement $u_z\ (x,y)$ across the surface to compute the left hand side of Eq. (1). Away from the applied force, a non-zero result here as a function of position identifies a generalized force which now exists in the structure as a consequence of the presence of the flaw. The appearance of these forces together with their position then serve to detect and locate the fault. In principal, the details of the derived force could be used to further characterize the fault although we have not yet exploited this possibility.

ω- k Mapping

In ω - k mapping[5], a two dimensional temporal and spatial FFT is performed on the measured displacement data thus providing a frequency (ω) - wavenumber (k) representation of the elastic vibration. These transforms are spatially windowed to provide local information. For elastic wave propagation, this format displays characteristic "dispersion" curves indicating the elastic wave types present (e.g. compressive, shear, flexural, etc.) and the frequency dependent velocities. Local differences in these curves from those observed or expected in unflawed structures indicate variations in wave types or in their speeds which are directly related to material parameter variations associated with the development of flaws. This Fourier acoustic technique has been particularly successful when applied to delamination effects in layered structures. In such cases, slow flexural waves excited in the detached layer present their unmistakable $\sqrt{\omega}$ dispersion curves in distinct contrast to the nearly vertical lines of the faster waves traveling in the uncompromised, adhered structure.

Previous Success: Assessing Wall Paintings and Underlying Structure at the U.S. Capitol Building

Figure 2. (Left) Experimental arrangement for plaster wall assessments at the U.S. Capitol Building showing the SLDV monitoring system, a shaker used to excite the art-laden walls, and a lap - top computer data acquisition system in the Brumidi Corridor; (Right) a photograph of the President's Room where extensive measurements were made on the walls and ceiling.

The authors were invited to demonstrate and evaluate their new fault detection and localization techniques for assessing the integrity of art-bearing walls and ceilings in various rooms in the US Capitol. The United States Capitol Building (both House and Senate) has large expanses of important fine art and decorative paintings[6] executed directly on the original lime plaster. In support of a comprehensive infrastructure modernization program in the building, the integrity of the supporting structures are being evaluated so that degradations underlying the artwork can first be located and repaired. The frescoes were painted in the nineteenth century by the Italian artist Constantino Brumidi[6] on a roughly two-centimeter thick structure consisting of three layers of plaster of varying composition supported by a thick masonry foundation. A successful non-destructive evaluation technique must be able to detect throughout the structure defects including loss of cohesion within a plaster layer and delaminations between the layers or at the attachment of the mortar to the supporting wall structure. The left insert in Fig. 2 shows the typical set-up we used to carry out preliminary diagnostic studies, in this particular case for the Brumidi Corridor of the Senate Wing. Panels on the wall or ceiling were excited over a band of frequencies by the use of either a broadband shaker applied directly at a point on the structure or an acoustic speaker which exposed the walls and ceiling to acoustic energy.

As depicted, a scanning laser Doppler vibrometer was used to map the fine scale vibratory motion of the wall or ceiling over the area of interest using a serpentine grid pattern with a spacing of several centimeters. In addition to the Brumidi Corridor, measurements were also carried out in the Senate Reception Room, The President's Room (see Fig. 2), The House Appropriations Committee Room, The Parliamentarian's Office, and the Office of The Speaker of The House.

In general, our techniques were very successful at detecting and locating faults when they existed in the structure underlying the art. We were able to identify a variety of problems including areas of unconsolidated plaster, various size regions having delaminations between plaster layers, and places where there is complete detachment of the plaster from its typically brick foundation. Overall, our SLDV-based structural acoustic approach compared favorably to other techniques used at the Capitol including those employing radar and thermal imaging.

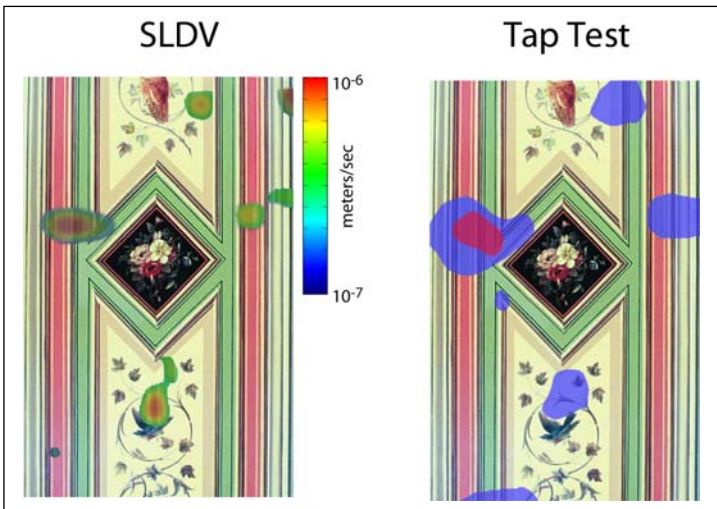

Figure 3. A comparison of the faults found by our structural acoustic technique (left) and by a tap test (right) in a fresco panel in the Brumidi Corridor of The U.S. Senate. Displayed on the left is the result of the VV algorithm and the color scale shows velocity in m/sec for a one newton force applied to the wall. The tap test is a labor intensive, time-consuming process wherein a skilled practitioner taps with a small hammer-like tool sequentially on a large number of points on the surface while listening with his unaided ear to the audible response of the wall from which he locates underlying faults.*

Fig. 3 shows a result we obtained on a panel in the Brumidi Corridor. On the left is shown a quantitative color map representing our measured displacement data after processing with the |VV*| algorithm[1,3] which sums the absolute magnitude of the measured normal velocity at each spatial point and over each frequency bin. This clearly indicates six or so localized faults. They are attributed to simple, small areas of delamination between the innermost plaster layer and its attachment to the brick supporting structure. In this particular case, the results can be compared to the available findings from what is called a "tap" test. In this age-old technique, a skilled conservator literally taps with a small hammer-like tool sequentially on a large number of points on the surface while carefully listening with his unaided ear to the audible response of the wall from which a qualitative fault map is generated. Although an experienced, skilled practitioner can often identify the existence (and sometimes type) of inhomogeneity, using this method it is impractical to gather - much less record - such information, especially over large expanses. None-the-less, Fig. 3 shows satisfying agreement between our laser-automated, quantitative, rapid method and the time consuming, human-discerned result.

We have also studied and successfully demonstrated our structural acoustic fault detection methods on a number of relatively simple laboratory structures. These include metal plates with flaws, lap joints with varying degrees of attachment, and thin, stiffened panels with segments of frame detachment[7].

VIII. MATERIALS AND METHODS

In this SEED program, we extended our SLDV/inversion structural health monitoring technique by: developing advanced inversion algorithms; combining several inversion

algorithms for improved fault detection; applying the these techniques to various parts of a building fabric including simple structures fabricated from concrete, brick, plaster, steel, wood, etc.; and demonstrating proof of concept in the laboratory. In particular, the following investigations were carried out.

Differing Materials –Thin and Thick Plates

We determined the feasibility for extending our SLDV/inversion approach augmented with new developments beyond its successful application on plaster walls to various parts of a building fabric and structure including those fabricated from concrete, steel, wood, etc. This effort was carried out using a numerically generated vibration data base using advanced h-p adaptive, finite element–based structural acoustic codes developed in our group in other programs. The structures for which numerical data was generated included: (1) thin plates of plaster, steel, and concrete with and without internal flaws; (2) thick plates of plaster and steel wherein flaws at three depths could be studied; and (3) a slab of wood with and without internal flaws. The first two cases were successfully handled using the isotropic flexural wave inversion algorithms. The last case is much more complex than the previous materials in that the wood is orthotropic, and this required the development of an orthotropic inversion operator.

Orthotropic Wooden Slabs

In the case of wood, we had to take into account the orthotropic nature of the material. In particular, we explored the extension of these inversion algorithms to the orthotropic thin plate case by developing a variational form of the differential equation for transverse bending and solving for the orthotropic flexural rigidities. The extended techniques are applied to a finite-element generated numerical data base for point excited wooden plates with and without an internal inclusion at 5 kHz and 10 kHz. Operation of the original isotropic algorithms on the wooden plate surface displacements is shown to fail in recovering the uniform elastic parameters or in detecting and locating the fault. The new algorithms based on the wave equation for a thin, orthotropic plate successfully convert the surface displacements on the uniform wooden plate to elastic parameter maps which serve to detect and localize the inclusion in the flawed plate. The results, particularly at the higher frequency, indicate that the onset of failure in the thin plate approximation is impacting both the inversion and the generalized force mapping accuracy. However, in this case use of the inversion algorithm to obtain modified wave equation coefficients followed by operation of the force mapping algorithm with these new parameters inserted is shown to successfully mitigate this effect.

Adaptive Inversion

Current algorithms which invert measured vibration maps into internal elastic parameters require knowledge of the equations of motion appropriate for the structure under study which restricts their areas of application. Using our extensive experience in the development of inversion algorithms for material parameter characterization and fault detection which use

dynamic surface displacement measurements obtained with SLDV[1,2,3,7] or interior displacements obtained using Magnetic Resonance Elastography (MRE)[8,9], we addressed the development of novel training algorithms for fault detection which do not depend on a-priori knowledge of the structural equations of motion.

In one such adaptive approach, we explored the idea of cascading various algorithms. One promising approach applied to thick plate structures used the flexural inversion operator appropriate to thin plates. The "effective" stiffness parameters so obtained were then inserted into the generalized force equation method which locates regions with non-zero forces and identifies those as faults.

In a second approach, we defined a set of equations which have arbitrary coefficients that multiply sets of spatial and temporal derivatives of the measured displacements. In this formulation, the equations appear as homogeneous sets of partial differential equations whose coefficients are generally unknown, yet which can be "trained" for any particular structure. Therefore, given a sufficient number of measurements on a control section, the coefficients can be determined, thereby "training" the algorithm to detect fluctuations due to material parameter or structural differences. As with our previous inversion techniques, the trained algorithm would also provide *local* properties thus providing locations of any faults. Further, we explored validation criteria for this adaptive coefficient approach based on the fact that the coefficients associated with the most appropriate solution should have a minimum variance normalized by the mean square value.

Modern Classifiers

A fourth area we explored albeit briefly involved exploiting modern identification (ID) algorithms that use the unique feature spaces derived from the previously described algorithms. The Physical Acoustics Branch has extensive experience in applying such ID algorithms in our on-going work[10-14] on underwater targets and UXO identification. These algorithms include hidden Markov models (HMM), relevance vector machines (RVM), and kernel matching pursuits (KMP). We expected that application of these algorithms as well as fusion of their modalities might provide both improved performance for fault detection and material parameter determination as well as determination of depth profiles of faults or material parameter fluctuations. This effort was not completed.

Plaster Dome Ceiling: A Numerical Study

A fifth area we explored involved plaster domed ceilings. In a number of the truly historic buildings whose finish layers often consist of plaster, walls and/or ceilings often bear precious artwork such as mosaic or frescoed images. In the case of the latter, where the paintings were created on wet plaster, the current physical and mechanical condition of the plaster layer(s) determines for the most part the near to mid term viability of the artwork. Particularly for the case of a ceiling, the development of defects such as detachment of the plaster layer from its

supporting brick or mortar structure or pockets of plaster deconsolidation can eventually lead to catastrophic failure of the plaster ceiling and the unrecoverable loss of priceless artwork.

Several years ago, Bucaro et. al.[1] and Vignola et. al.[3] reported the successful use of externally produced vibration to evaluate the state-of-health (SOH) of highly frescoed plaster walls in the U.S. Capitol Building. In this technique, a low level broadband force was applied locally to the wall using an electro-dynamic shaker, and the resulting spatially dependent surface vibrations were mapped over the frescoed wall using a SLDV. Direct observation of the scanned displacement maps allowed those authors to detect and locate plaster defects whose presence was subsequently confirmed by conventional tapping tests. These studies were empirical in nature, and little supporting vibration analysis was reported which would allow one to generalize these results to other situations.

In this SEED effort we considered a related approach in which a broadband *acoustic speaker* rather than a shaker is used to excite the structure. As in the shaker excitation case, the resulting vibrational response of the structure would be mapped over its surface using a scanning laser Doppler vibrometer. Use of a speaker is an especially attractive approach for ceilings in that both the excitation and the scanning could be carried out remotely eliminating the requirement for scaffolding. Although such an acoustic speaker approach had been introduced and applied to frescoes by Castellini, et. al.[15] and later applied by Tornari et. al.[16] to mosaics, ceramics, inlaid wood, and easel paintings, both these and subsequent studies using speaker (or for that matter shaker excitation) did not provide sufficient analytical results which would allow one to predict the sensitivity of the technique to defect detail such as type and size and how well the approach might perform more generally.

In the SEED study, we used a simulated data base of surface vibration generated using an advanced structural acoustic finite element-based code. In particular, we explored application of the speaker-based technique to what we consider to be a generic domed ceiling – a common structure found in historic buildings and residences - in which a plaster layer is attached to, and takes the shape of, a backing structure considered to be relatively rigid such as brick or mortar. Aided by static analysis, we addressed the effectiveness of using the "measured" surface displacements resulting from acoustic speaker excitation to detect and localize two different defect types: (A) detachment of the plaster layer from the supporting brick or mortar, and (B) an internal region in the plaster which has become deconsolidated. Specific questions we wished to resolve are: (1) Is acoustic excitation effective at producing readily measured surface displacements which could be used in detecting these flaws? (2) In general, what issues and/or benefits are introduced by using acoustic speaker versus force actuator excitation? (3) Are typical defects of the type mentioned above detectable by straightforward observation of the acoustically excited spatial displacement maps and how does this depend on flaw size and ceiling thickness? (4) What is the minimum detectable defect size? And (5) if a defect is detected, might one be able to differentiate between detachment and deconsolidation?

Novel Spatial Transform

A sixth area we explored is based on our new ideas in novel transform methods[17] in structural and physical acoustics. Presently, Fourier decompositions of spatial vibrations are in practice restricted to surfaces defined by separable geometry systems for a meaningful interpretation of their spectra. In our new technique, we define and develop a purely local spectral analysis approach which uses spatially conformal Fourier decompositions. This allows us to analyze dispersion behavior on any surface or structure irrespective of its shape. This leads to an important augmentation of our ω - k mapping[5] technique in which local differences in the dispersion curves from those observed or expected in unflawed structures indicate variations in wave types or in their speeds which are directly related to material parameter variations associated with the development of flaws. We also anticipate that this new transform approach will lead to heretofore unexploited spectral features for classification and vibration analysis. In particular, we applied this new technique to fault identification on an elliptical plaster dome ceiling.

Laboratory Demonstration

Finally, we carried out a laboratory–based SLDV demonstration on a generic structure as an additional demonstration of proof of concept and efficacy of this overall approach. The structure chosen was a long 2” × 10” ceiling support beam in the interior of which was created a 2” × 2.5” × 5/8” thick defect at its mid-plane which approximated decay or termite-like damage to the wood. Broadband SLDV scans were obtained across the available surface of the structure providing dynamic displacement fields in the usual manner. These data bases were analyzed in two ways. First, the displacement maps were examined without any inversion to determine if the defect was observable by direct observation of the contrast in the spatially mapped displacements. This was indeed found to be the case in a frequency band which included the resonance frequency of the defect. Secondly, the displacement measurements were operated on by the various processing algorithms developed in the program. These inversion operators indicated that the wooden beam had considerable variations in its spatial properties, and this result requires further study.

IX. RESULTS AND ACCOMPLISHMENTS

Thin and Thick Plates of Various Materials: Numerical Studies at Three Frequencies.

We determined the feasibility for extending our SLDV/inversion approach augmented beyond its successful application on plaster walls to various parts of a building fabric and structure including those fabricated from concrete, steel, wood, etc. This effort was carried out using a numerically generated vibration data base using advanced h-p adaptive, finite element–based structural acoustic codes developed in our group in other programs. The structures for which numerical data was generated included: (1) thin plates of plaster, steel, and concrete with

and without an internal flaw; (2) thick plates of plaster and steel wherein flaws at three depths could be studied; and (3) a slab of wood with and without an internal flaw.

Isotropic Thin Plates Made of Steel, Concrete, and Plaster.

In this section, we apply our inversion method to a finite element database, simulating the dynamic response of point-driven, solid, homogeneous plates of dimensions length = 60 cm, width = 30 cm, and thickness = 2.54 cm, with and without an internal flaw. These plates were comprised of steel, concrete, and plaster, and the material parameters utilized in our studies are provided below. The flaw was modeled as an inclusion (see Fig. 4) of length = 2 cm, width = 1.5 cm, and thickness = 0.5cm (centered at x = -8.7 cm, y = 19 cm, and z = 1.27 cm). In each case, while the plates and the inclusions have the same Poisson's ratio, density, and attenuation, the Young's moduli differ. Specifically, there were two variations of the material stiffness comprising the inclusion. In the inversions below, Flaw1 has a Young's modulus 1000 times less than that of the surrounding plate, while Flaw2 has a Young's modulus 20 times less than that of the surrounding plate structure. In the Table 1 below, we show these material parameters.

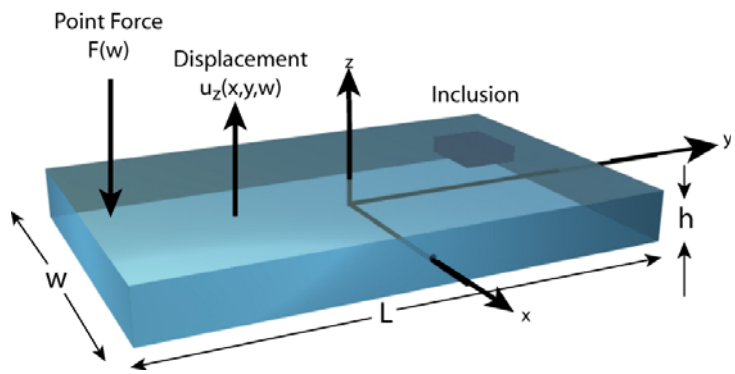

Figure 4. Co-ordinate system and plate geometry used in the finite element calculations of normal surface displacement for point excited plates with and without an internal flaw.

The plates were dynamically excited at a point at 1 kHz, 5 kHz, and 10 kHz, respectively, and the displacements were calculated using the finite element method. The plates were modeled as 3D solids fixed on the all the side faces. The spatial mesh for both the thin and the thick plate model had a total of 9000 hexahedral volume elements. Based on a p-convergence study of the given mesh a cubic-degree (p = 3) approximation was utilized for the response computations. For the thin plate model this resulted in a total of 34038 complex-valued unknowns out of which 3240 were constrained and the remaining were free. For the thick plate model this resulted in a total of 223608 complex-valued unknowns out of which 15120 were constrained and the remaining were free.

Table 1: Plate Material Parameters

	Young's modulus (Pa)	Density (Kg/M^3)	Poisson's Ratio	Attenuation
Steel	200×10^9	7900	0.3	0.01
Concrete	26×10^9	2300	0.22	0.02
Plaster	7×10^9	1444	0.2	0.02

The flexural wave inversion operator[4] we are applying is shown mathematically below:

$$\frac{Eh^2}{12\left(1-\upsilon^2\right)\rho} = \omega^2 \frac{\int u_z v_z dxdy}{I} \tag{3a}$$

where the denominator is given by:

$$\begin{aligned} I = \int_y \left[\frac{\partial^2 v_z}{\partial x^2} \frac{\partial u_z}{\partial x}\bigg|_x - \frac{\partial^3 v_z}{\partial x^3} u_z \bigg|_x + \int_x u_z \frac{\partial^4 v_z}{\partial x^4} dx \right] dy \\ + 2\int_x \int_y u_z \frac{\partial^4 v_z}{\partial x^2 dy^2} dxdy \\ + \int_x \left[\frac{\partial^2 v_z}{\partial y^2} \frac{\partial u_z}{\partial y}\bigg|_y - \frac{\partial^3 v_z}{\partial y^3} u_z \bigg|_y + \int_y u_z \frac{\partial^4 v_z}{\partial y^4} dy \right] dx. \end{aligned} \tag{3b}$$

As discussed in Ref. 4, this is a specially designed inversion operator in which a virtual function, *v*, is introduced in such a way that the higher order spatial derivatives, rather than operating on the "measured" displacement *u(x,y)*, operate on the virtual function *v* which are not only analytic but can be chosen with beneficial boundary values. We show the results of applying the inversion operator on the plaster, concrete, and steel thin plates in Figs. 5-7 together with the displacement maps for the plates with and without the flaw.

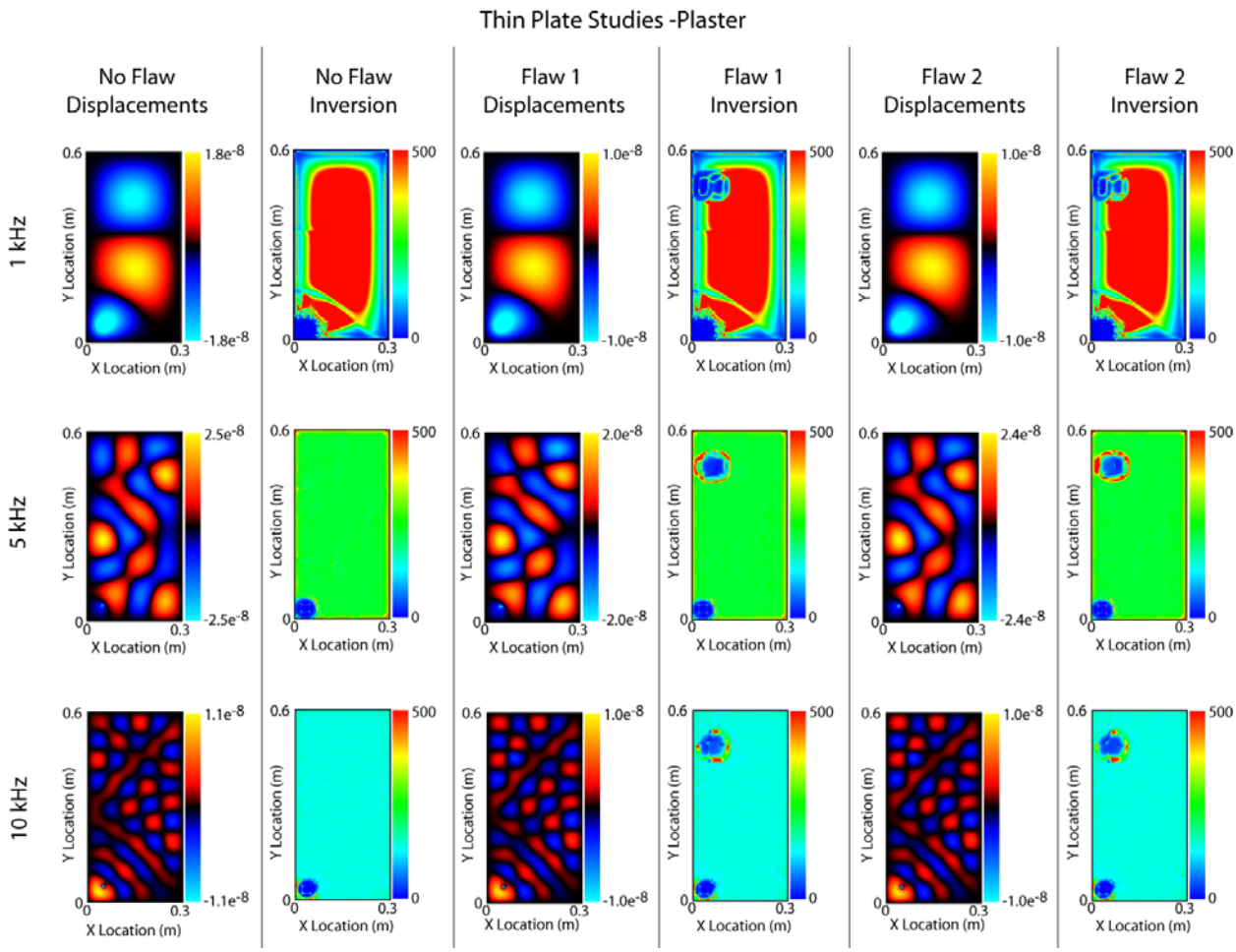

Figure 5. Numerically generated displacements at 1, 5, and 10 kHz and flexural wave inversions for thin plaster plates with flaw and no flaw.

As can be seen in Fig. 5 for the plaster, the faults are not apparent in the displacement maps themselves. However, operation of the inversion operator clearly indicates the presence and location of both internal faults. Surprisingly, this is the case even for the lowest frequency where there is only perhaps one and one half flexural wavelengths across the plate.

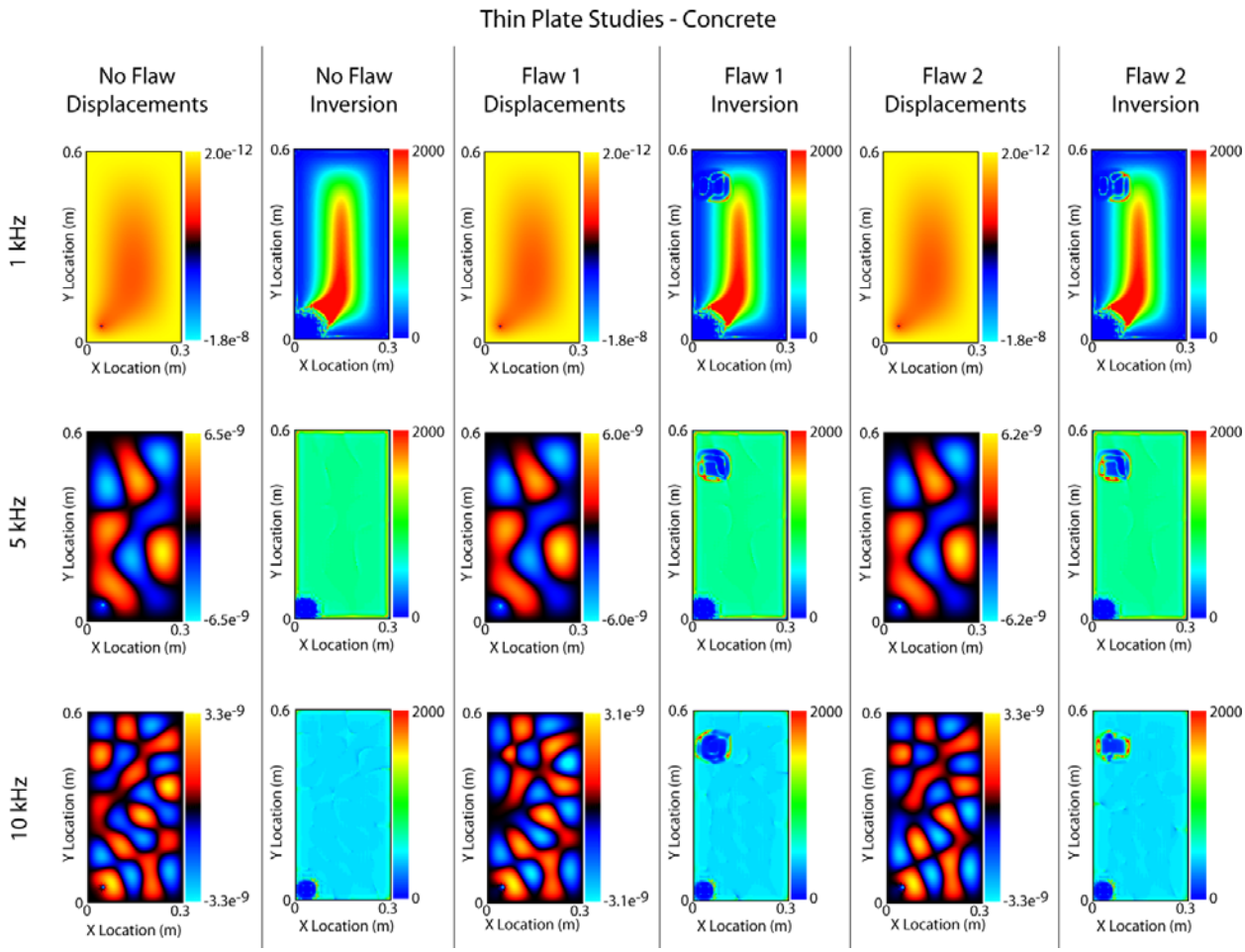

Figure 6. Numerically generated displacements at 1, 5, and 10 kHz and flexural wave inversions for thin concrete plates with flaw and no flaw.

Again in the case of concrete, as can be seen in Fig. 6, the faults are not apparent in the displacement maps themselves. However, operation of the inversion operator clearly indicates the presence and location of both internal faults. And again this is the case even for the lowest frequency where there is now only perhaps one half flexural wavelengths across the plate.

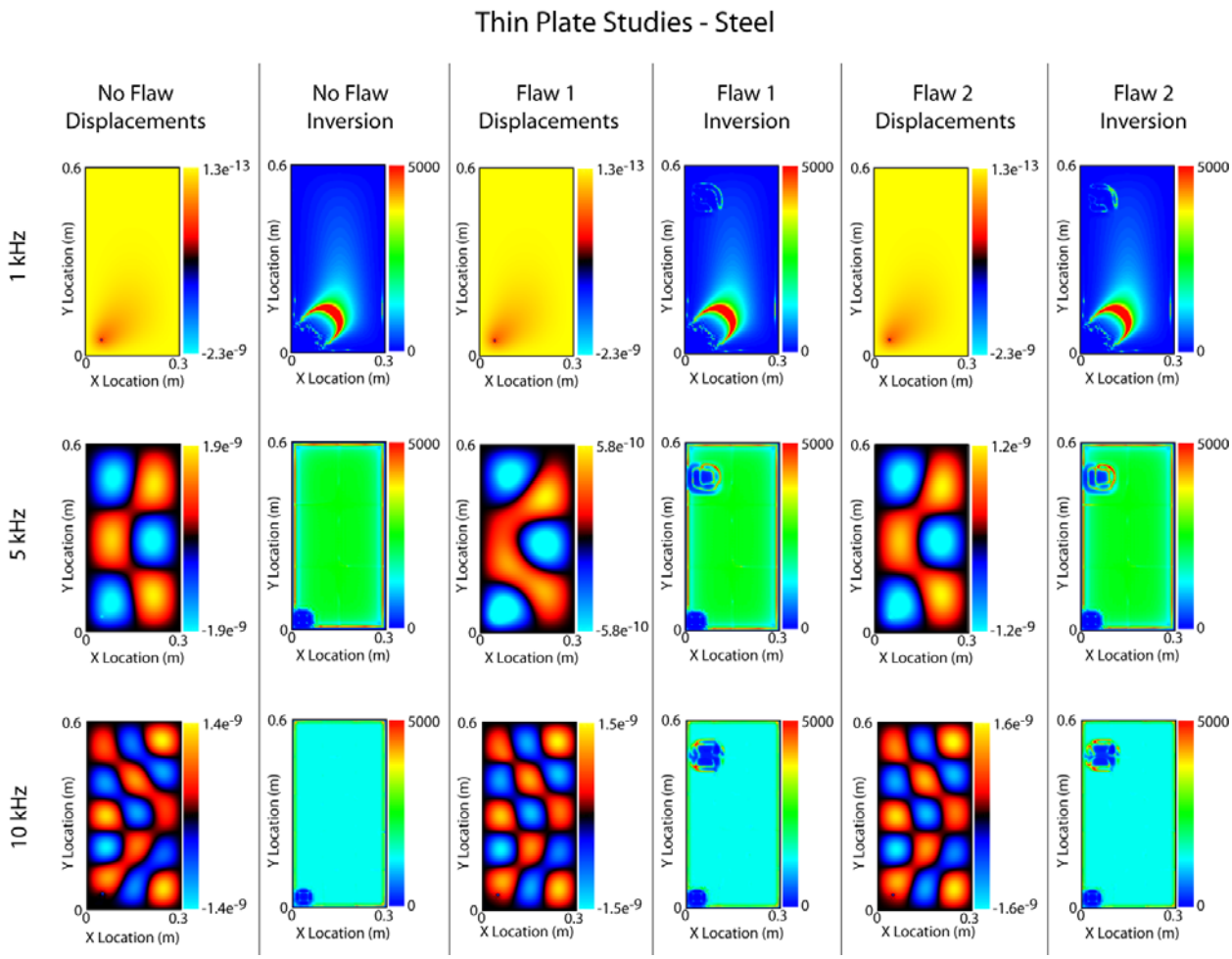

Figure 7. Numerically generated displacements at 1, 5, and 10 kHz and flexural wave inversions for thin steel plates with flaw and no flaw.

Finally, in the case of steel, as can be seen in Fig. 7, the faults are again not apparent in the displacement maps themselves. However, now only at the higher frequencies, operation of the inversion operator clearly indicates the presence and location of both internal faults. This lower performance at the lowest frequency is quite expected and is related to the fact that for the very high wave-speed in steel, only a small fraction of a flexural wavelength exists across the plate.

Isotropic Thick Plates Made of Steel and Plaster.

In this section, we apply our inversion method to a finite element database, simulating the dynamic response of point-driven, solid, homogeneous plates of dimensions length = 60 cm, width = 30 cm, and thickness = 5 cm, without and with internal flaws at three different depths. These plates were comprised of steel and plaster, and the material parameters utilized in our studies are provided below. The flaws were modeled as inclusions of length = 2 cm, width = 1.5

cm, and thickness = 0.5 cm (centered at x = 8.7 cm, y = 19 cm, and three separate locations (see Fig. 8) across the thickness: z_1 = 1.27 cm (Top), z_2 = 0.0 cm (Mid), and z_3 = -1.27 (Bottom)). In each case, while the plates and the inclusions have the same Poisson's ratio, density, and attenuation, the Young's moduli differ. Specifically, there were two variations of the material stiffness comprising the inclusion. In the inversions below, Flaw1 has a Young's modulus 1000 times less than that of the surrounding plate, while Flaw2 has a Young's modulus 20 times less than that of the surrounding plate structure. The plate material parameters are again shown in Table 1. As before, the plates were dynamically excited at 1 kHz, 5 kHz, and 10 kHz, respectively. Again, the flexural wave inversion operator[4] shown mathematically in Eq. (3) was applied to the calculated surface displacement data base.

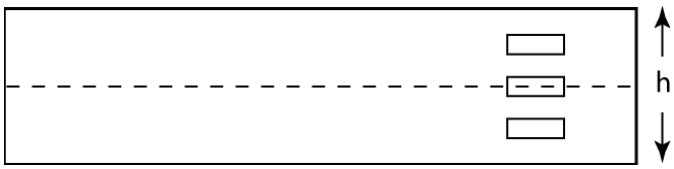

Figure 8. Cross section of thick plate showing flaws at three different depths.

As can be seen in Figs. 9 - 11, the inversions for the thick steel case show the presence of all three flaws for any of the three frequencies. As in the thin plate case, the flaws are not noticeable in any of the displacement maps themselves. The inversion at the lowest frequency (1 kHz) shows an anomalous feature across the top of the plate; and although its origin is not understood, we are not surprised that the lowest frequency which has only a fraction of a wavelength across the plate has the poorest performance. The flaws are quite dominant in the inversion maps for the two higher frequencies.

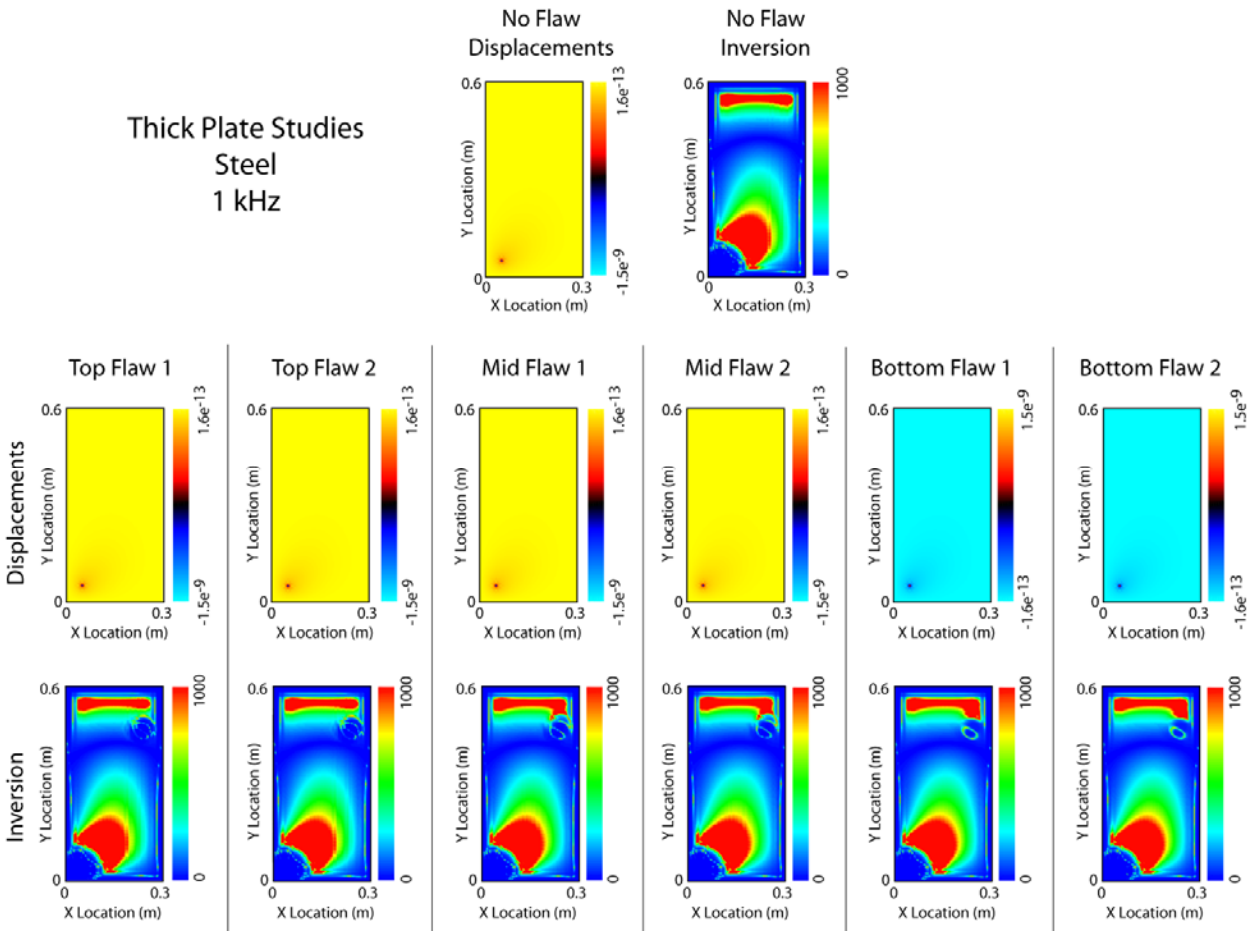

Figure 9. Numerically generated displacements at 1 kHz and flexural wave inversions for thick steel plates with no flaw and flaws at three different depths.

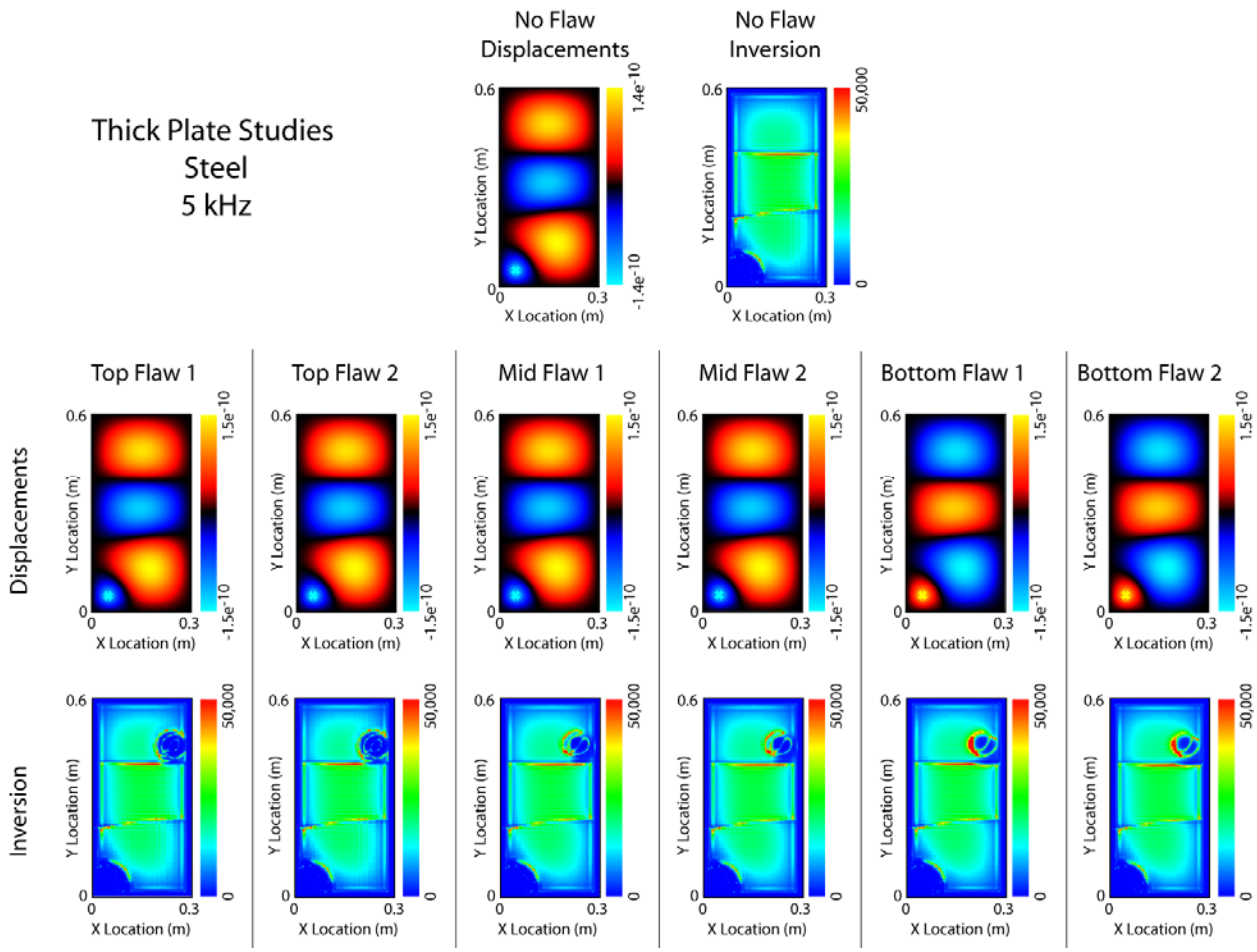

Figure 10. Numerically generated displacements at 5 kHz and flexural wave inversions for thick steel plates with no flaw and flaws at three different depths.

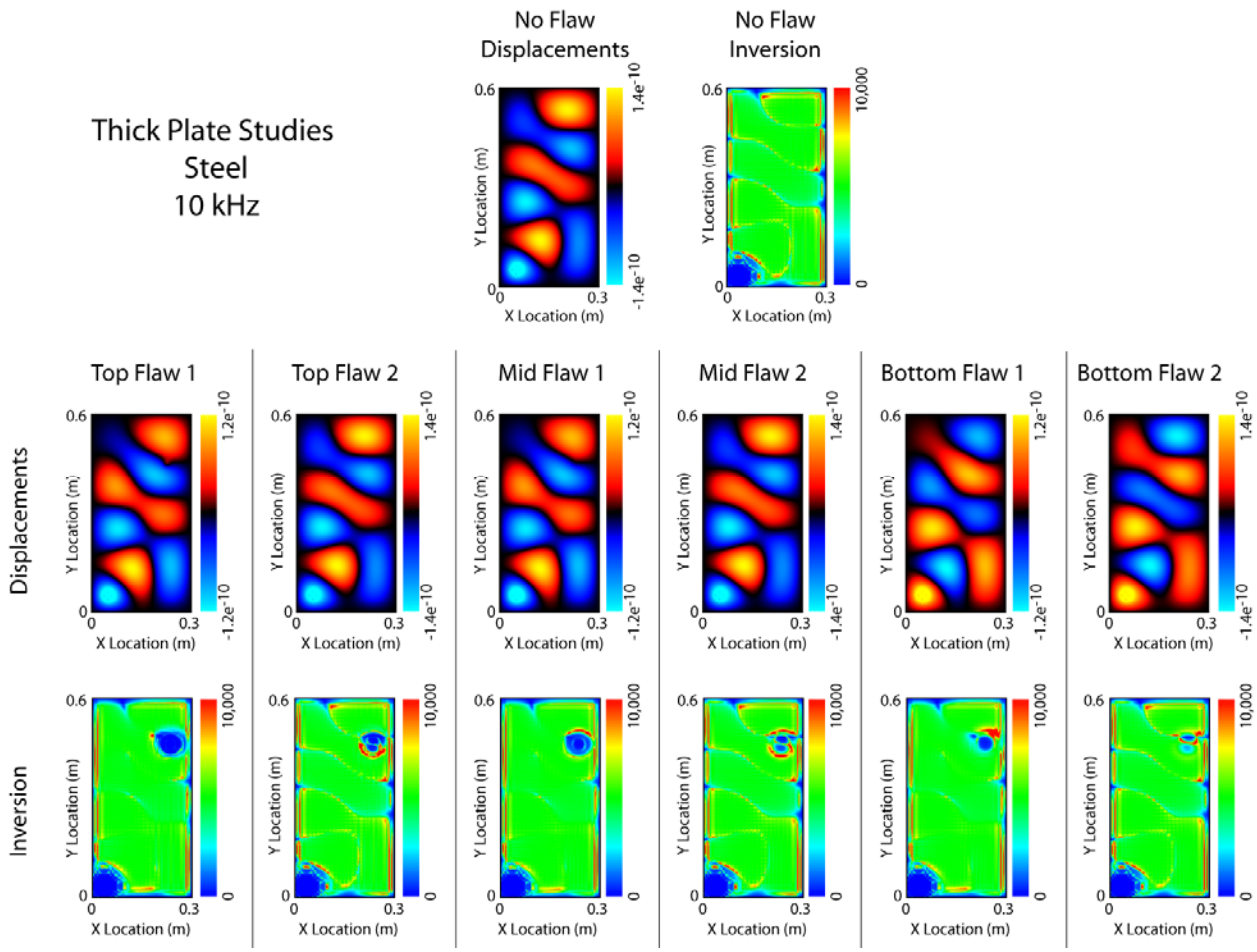

Figure 11. Numerically generated displacements at 10 kHz and flexural wave inversions for thick steel plates with no flaw and flaws at three different depths.

Next we show the inversions for the thick plaster plate case in Figs. 12 - 14. In contrast to the case for steel, all three flaws are noticeable in the inversion maps only for the highest frequency (10 kHz). In this case they are barely visible in the lowest frequency maps (1 kHz), and in addition there is a dominant artifact in the lower left near the shaker position. At 5 kHz, the top flaw and mid-plane flaw are visible but not the deepest one.

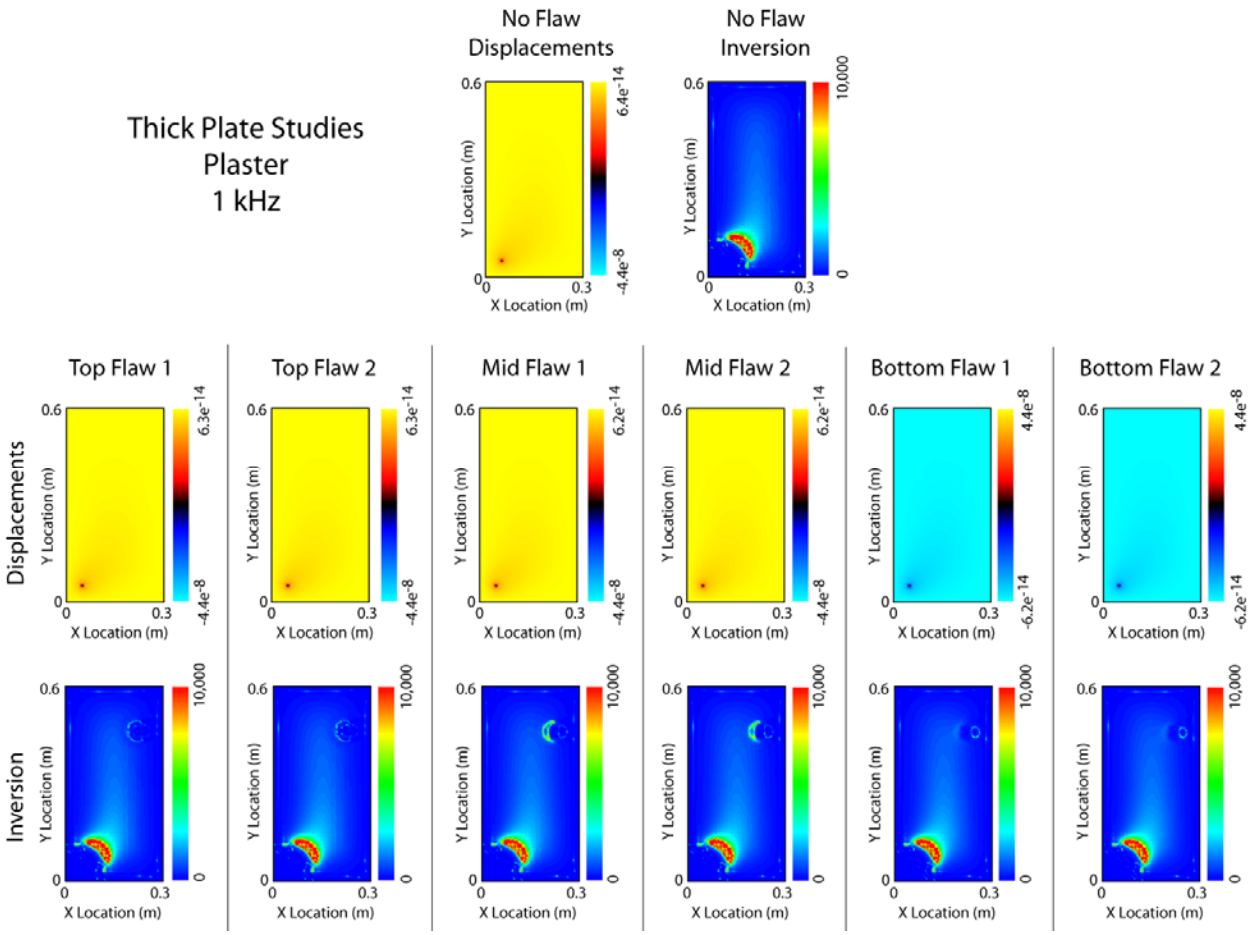

Figure 12. Numerically generated displacements at 1 kHz and flexural wave inversions for thick plaster plates with no flaw and flaws at three different depths.

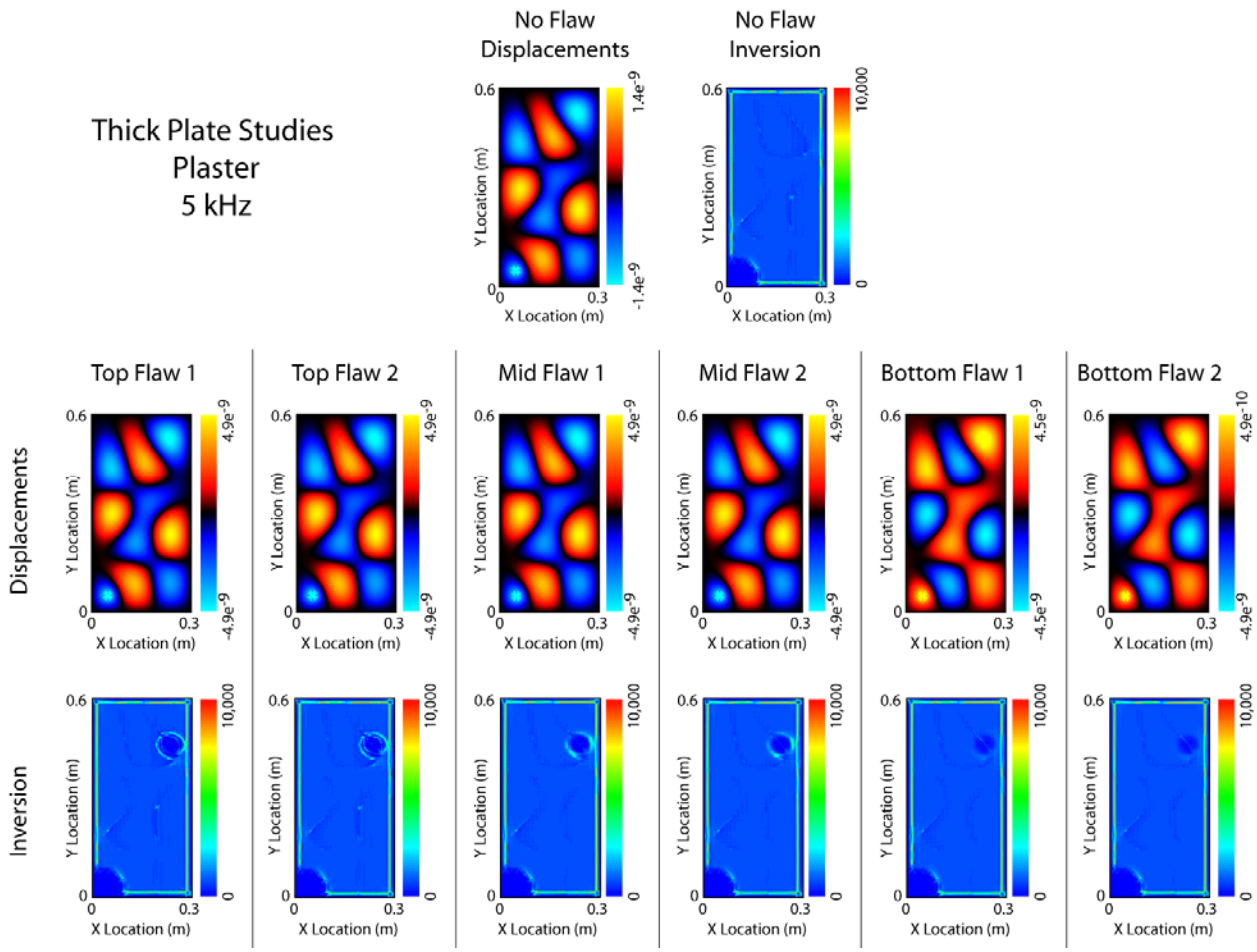

Figure 13. Numerically generated displacements at 5 kHz and flexural wave inversions for thick plaster plates with no flaw and flaws at three different depths.

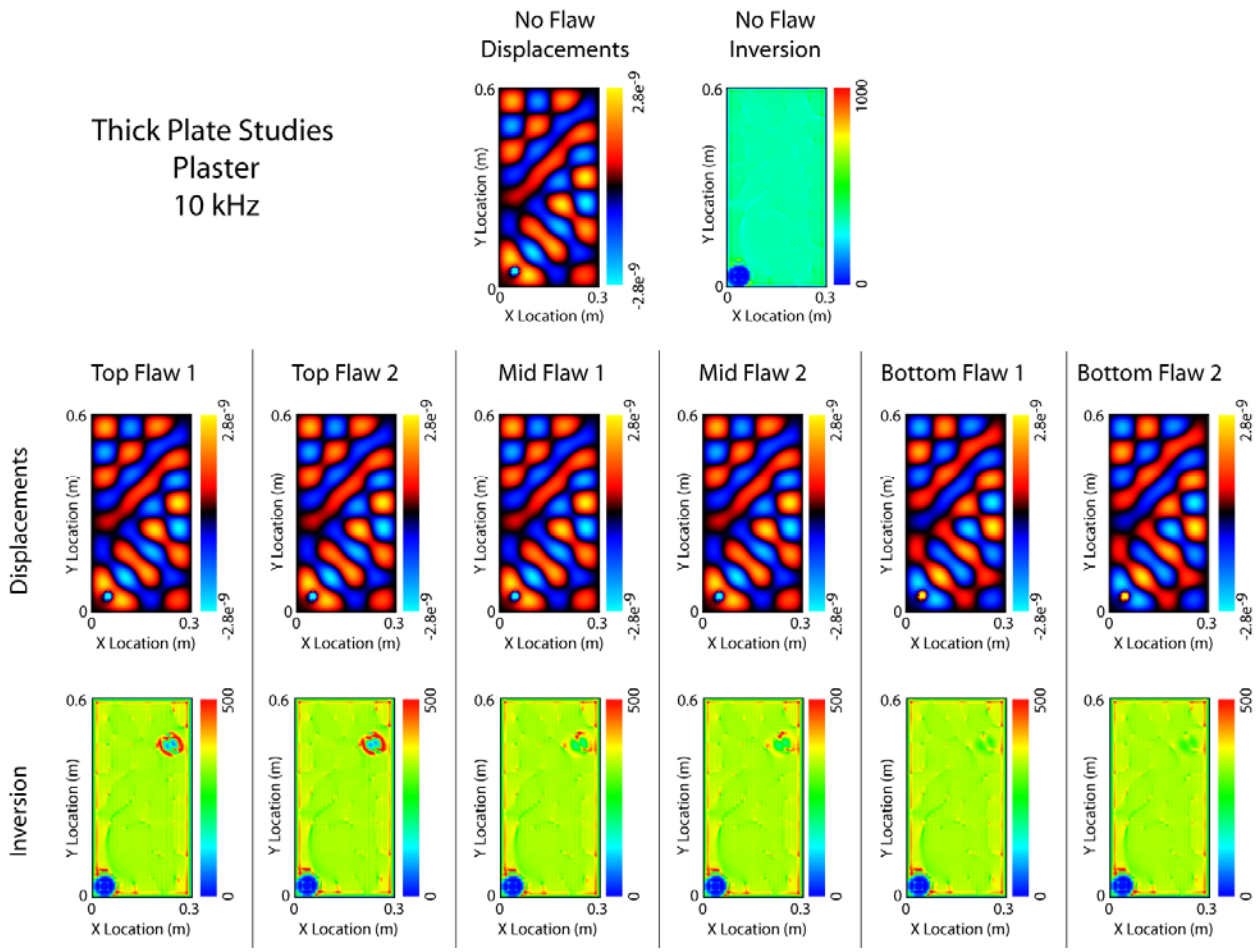

Figure 14, Numerically generated displacements at 10 kHz and flexural wave inversions for thick plaster plates with no flaw and flaws at three different depths.

The best performance for the thick plaster plate is that at 10 kHz where all flaws are visible. However, the deepest flaw has the poorest definition. Although we did not run the data for the thick concrete plate, we expect that as in the thin plate case the inversions would be similar to that for the plaster case.

Orthotropic Inversion Operators and Application to Wood Slabs

Wood materials are orthotropic and we would not expect inversion operators derived from the isotropic flexural wave equation to be effective. Accordingly, we developed an analogous inversion operator based for orthotropic materials. In the case of an orthotropic thin plate, the differential equation for the transverse bending is given by Leissa[18]

$$D_x \frac{\partial^4 u_z}{\partial x^4} + 2D_{xy} \frac{\partial^4 u_z}{\partial x^2 \partial y^2} + D_y \frac{\partial^4 u_z}{\partial y^4} - \rho\omega^2 h u_z = f_z(x, y, \omega), \tag{4}$$

where

$$\left.\begin{aligned} D_x &= \frac{E_x h^3}{12(1-\nu_{xy}\nu_{yx})} \\ D_y &= \frac{E_y h^3}{12(1-\nu_{xy}\nu_{yx})} \\ D_{xy} &= D_x \nu_{yx} + 2D_k \\ D_k &= \frac{G_{yx} h^3}{12} \end{aligned}\right\} \tag{5}$$

In these equations D_x, D_y and D_{xy} are the flexural rigidities, E_x, E_y and G_{yx} are the orthotropic elastic moduli, and ν_{xy},ν_{yx} the relevant Poisson's ratios. The equivalent variational form can be expressed as

$$\int_x \int_y \left(v_z \left(D_x \frac{\partial^4 u_z}{\partial x^4} + 2D_{xy} \frac{\partial^4 u_z}{\partial x^2 \partial y^2} + D_y \frac{\partial^4 u_z}{\partial y^4} \right) - v_z \rho \omega^2 h u_z \right) dxdy = \int \int v_z f_z(x,y,\omega) dxdy, \tag{6}$$

where the virtual functions, v_z , are defined above. Integration of Eq. (6) by parts four times yields

$$\begin{aligned} & D_x \left[\int_y \frac{\partial^2 v_z}{\partial x^2} \frac{\partial u_z}{\partial x}\bigg|_x - \frac{\partial^3 v_z}{\partial x^3} u_z \bigg|_x + \int_x u_z \frac{\partial^4 v_z}{\partial x^4} dx \right] dy + 2D_{xy} \left[\int_x \int_y u_z \frac{\partial^4 v_z}{\partial x^2 \partial y^2} dxdy \right] \\ & + D_y \left[\int_x \frac{\partial^2 v_z}{\partial y^2} \frac{\partial u_z}{\partial y}\bigg|_y - \frac{\partial^3 v_z}{\partial y^3} u_z \bigg|_y + \int_y u_z \frac{\partial^4 v_z}{\partial y^4} dy \right] dx \\ & - \int_x \int_y \rho \omega^2 h v_z u_z dxdy = \int_x \int_y v_z f_z(x,y,\omega) dxdy. \end{aligned} \tag{7}$$

As before, one can see that the variational form has forced all but first order derivatives onto the virtual functions thereby reducing the effects of spatially varying noise in the process of calculating higher order derivatives.

Orthotropic Inversion

As in the isotropic case, Eq. (7) can be utilized to solve for the orthotropic flexural rigidities away from any applied force (where $f_z(x,y,\omega)$=0). Since there are now three unknowns, a minimum of three excitation locations is required to provide a linearly independent set of equations. Labeling the integrals in Eq. (7) as $A_{ij,i,j}$=1,2,3, and the displacements due to each excitation as u_z^i, the set of equations may be expressed in matrix form as

$$\begin{bmatrix} A_{11} & A_{12} & A_{13} \\ A_{21} & A_{22} & A_{23} \\ A_{31} & A_{32} & A_{33} \end{bmatrix} \begin{bmatrix} \dfrac{D_x}{\rho h} \\ \dfrac{D_{xy}}{\rho h} \\ \dfrac{D_y}{\rho h} \end{bmatrix}_m = \begin{bmatrix} \iint_{xy} \omega^2 v_z u_z^1 dxdy \\ \iint_{xy} \omega^2 v_z u_z^2 dxdy \\ \iint_{xy} \omega^2 v_z u_z^3 dxdy \end{bmatrix}. \tag{8}$$

Letting the 3 × 3 matrix in Eq. (8) be represented as A, the unknown flexural rigidity column matrix as D, and the RHS as R, then the solution can be expressed as $D = A^{-1}R$, (Det $A \neq 0$). This set of equations may additionally be over specified and solved using algorithms such as the Conjugate Gradient Least Squares (Hansen[19]) method to site one example. For orthotropic plates, Eq. (8) replaces Eq. (3), its counterpart for the isotropic case.

Orthotropic Generalized Force Mapping

In the case of orthotropic plates, the Generalized Force Mapping operator assumes the following form

$$\int_x \int_y \left(v_z \left(\frac{D_x}{\rho h} \frac{\partial^4 u_z}{\partial x^4} + 2\frac{D_{xy}}{\rho h} \frac{\partial^4 u_z}{\partial x^2 \partial y^2} + \frac{D_y}{\rho h} \frac{\partial^4 u_z}{\partial y^4} \right) - v_z \omega^2 u_z \right) dxdy = \begin{cases} 0, \text{if the plate is homogeneous} \\ G_m \text{if a force or flaw is present} \end{cases} \tag{9}$$

where, as discussed above D_x, D_{xy}, and D_y are the orthotropic flexural rigidities, ρ and h the density and plate thickness, respectively, and $G_m = \int_x \int_y \left(v_z f_z(x, y, \omega) / \rho h \right) dxdy$ As the left-hand side of Eq. (9) is calculated at each two-dimensional voxel centered at the location x_m, y_m over the surface of the plate, non-zero values illuminate and map the spatial distributions of any faults (or applied forces).

This particular representation will be applied in two different ways. The first is one in which we utilize the "known" values for the flexural rigidities which are based on the elastic moduli used in the forward finite element calculations. The second is one in which we utilize the values for the flexural rigidities obtained from the orthotropic inversions. In this latter method, the values in Eq. (9) are therefore "calibrated" to the solution as provided by the application of the inversions. As will be seen, such an approach can have a dramatic effect in the performance of the GFI method.

Wooden Plate Detail

We focus our study and demonstration of these techniques on a solid, homogeneous, orthotropic wooden plate of dimensions length = 60 cm, width = 30 cm, and thickness = 2.54 cm with and without an internal inclusion. As depicted in Fig.15, we take the x, y, and z axes to be aligned with tangential, longitudinal (fiber), and radial wood grain and growth ring directions, respectively. The nine independent stiffness constants and density (450 kg/m^3) are taken to be that of Douglas coastal fir (see Table 2) as computed from the elastic and Poisson's ratios

reported by Green et. al.[20] . The flaw is in the form of a rectangular inclusion (see figure 1) of length = 2 cm, width = 1.5 cm, and thickness = 0.5 cm (centered at x = -8.7 cm, y = 19 cm, z = 1.27 cm) with the density unchanged but with each of the nine stiffness constants reduced to 0.05 its value in the normal wood.

Table 2. Nine independent stiffness matrix elements for Douglas fir (10^8 Pa).

C_{11}	C_{22}	C_{33}	C_{44}	C_{55}	C_{66}	C_{12}	C_{13}	C_{23}
8.450	150.6	11.44	11.50	1.030	9.430	4.784	3.390	4.851

The damping factor is taken to be 5 % and is accounted for by adding the appropriate imaginary component to each elastic moduli (Hosten[21]). Some support we can offer for choosing 5% is that the 2 dB/cm and 15 dB/cm longitudinal and shear attenuations in Douglas fir at 1MHz reported by Bucur[22] correspond to damping factors of 4.4 % and 2.2 %, respectively. Of course, our results are obtained at much lower frequencies (5 - 10 kHz) and for flexural waves. Also, damping factors for various wave types in white oak reported by Kerlin[23] fall anywhere between 1 % and 3 % in our frequency band. We favored erring on too high rather than too low a damping factor recognizing that the performance of our inversions are expected to decline with larger attenuation. In any case, the results we will present should not be too dependent on the actual damping number used in the range given above.

Finite Element Data Base

The displacement response of the orthotropic wood plate was obtained using a parallel hp-version finite element technique (Dey and Datta[24]) with a mesh consisting of 9000 volume elements. After a p-convergence check, a cubic (p = 3) discretization was used consisting of 208,448 complex-valued displacement degrees of freedom. The surface displacements were obtained resulting from a normal point force applied one at a time to three different positions on the plate, one near the lower left corner, one directly above it halfway up the plate, and the third near the upper left corner. (See Fig. 15.) In the finite element model, the boundary conditions were taken to be fixed, i.e. all three displacement components at the edges are zero. Particular boundary conditions should have little effect on our inversions since the latter are based on infinite plate, free-wave propagation. And

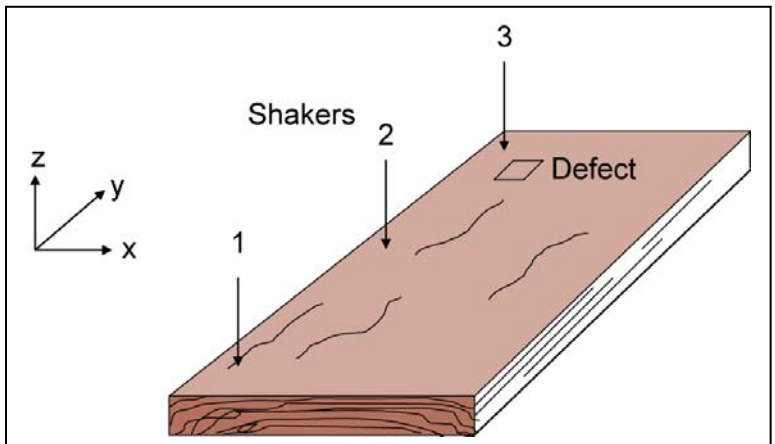

Figure 15. Wooden plate and Cartesian axes system. The x and z axes are along the wood tangential and radial growth ring directions, and the z axis along the longitudinal or fiber direction. The flaw is in the form of a rectangular inclusion centered midway through the plate depth. Also shown are three independent shakers used to excite the plate.

except for "edge distortion" at positions very near the boundaries of the plate (i.e. within distances << structural wavelength), the displacement responses are well-represented by linear combinations of the infinite plate, free-wave solutions (Skudrzyk[25]).

The responses were computed for two frequencies (5 kHz and 10 kHz) defining a band which we believe would be practical from both a force application and a scanned surface displacement measurement point of view. For each case we compute the normal surface displacement u_z (x,y,ω) on a rectangular grid with a spacing of 0.25 cm. The displacements at each frequency are shown in Fig. 16 for both the homogeneous plate and the flawed plate. It should be pointed out that the displacement maps themselves show little indication of the presence of the internal flaw.

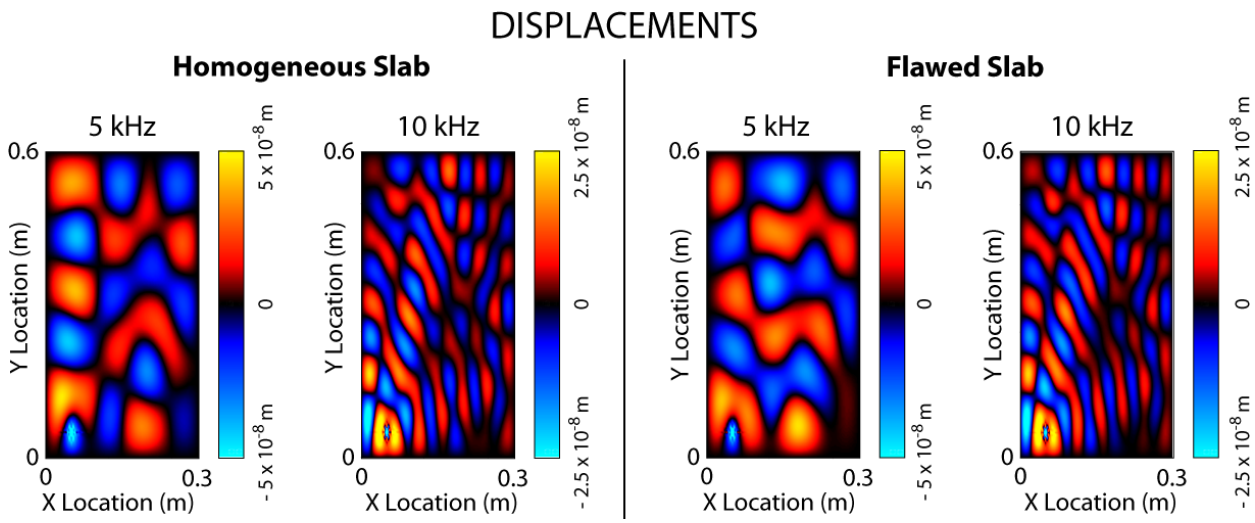

Figure 16. Calculated color-coded surface displacement at 5 kHz and 10 kHz when the shaker in the lower left position is excited at each frequency. Positive and negative relative phase is indicated by red to yellow and dark to light blue, respectively.

Results

To provide the inversion results, the integrations in Eq. (8) were calculated over 16 × 16 data points, centered at each of 106 × 226 pixels (x_m,y_m), i.e. $x_m \pm 8\Delta x$, $y_m \pm 8\Delta y$, yielding surface elements with sides $L_m^x = L_m^y = 4cm$. First, we can apply the inversion operator, Eq. (3), developed from the isotropic wave equation to the numerical data base of displacement on the wooden plates. In Fig. 17 we show the result of this operation on both the homogeneous plate and on the flawed plate for one of the driver positions (lower left). As can be seen – and as expected– the inversion algorithm fails in two respects: (1) it does not recover the known spatial uniformity of the effective plate stiffness for either plate (note the presence of large stiffness parameter values at a number of locations); and (2) it does not do well in detecting and localizing the internal flaw. These failures are not surprising and are a consequence of applying an

inversion operator built on the isotropic wave equation to an orthotropic structure. The same problems persisted when inverting the data associated with the other two shaker locations as well, although the results are not shown here.

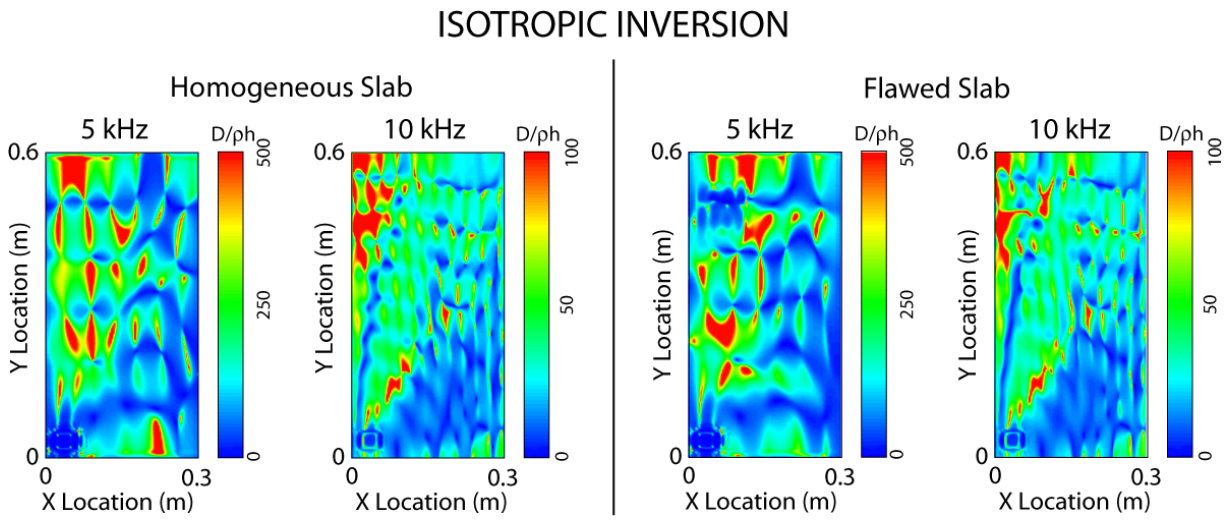

Figure 17. Result of applying weak flexural wave inversion operator (WFWI) developed for the isotropic case, Eq. (5), to the displacement data (lower left driver excited) at each frequency for both the homogeneous wooden plate and the flawed wooden plate. The magnitude of the inversion in units of D/ph is color coded from blue to red.

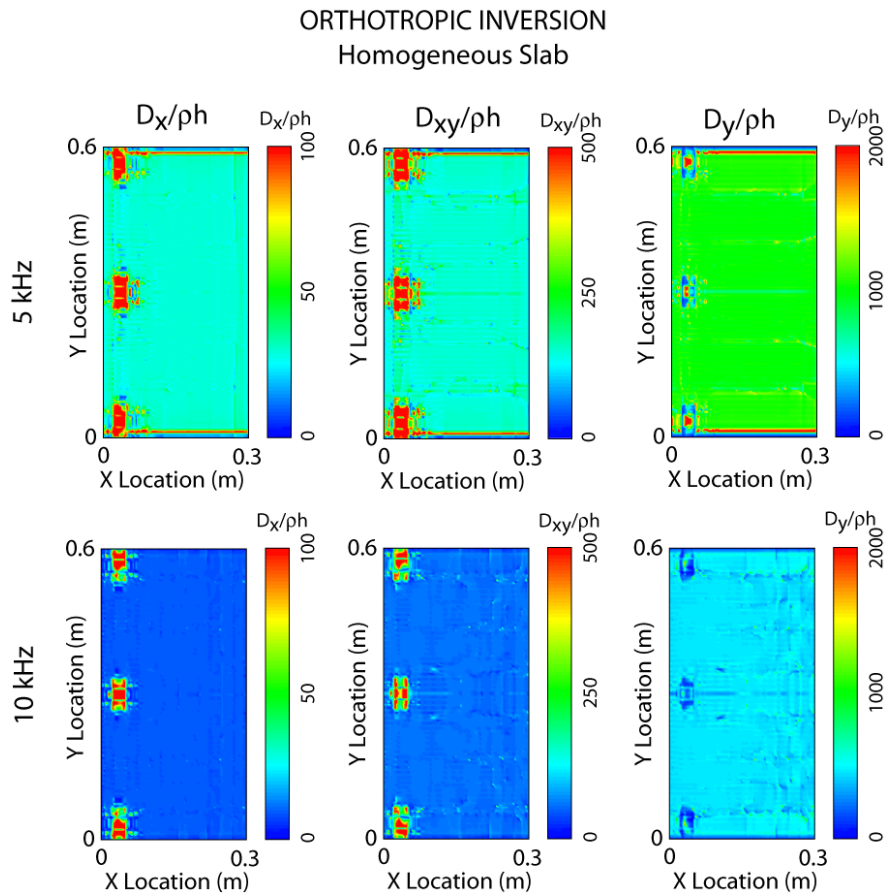

Figure 18. Result of applying the weak flexural wave inversion operator (WFWI) developed for the orthotropic case, Eq. (11), to the displacement data at each frequency for the homogeneous wooden plate to obtain the three stiffness parameters $D_x/\rho h$, $D_{xy}/\rho h$, and $D_y/\rho h$. The magnitude of the inversion in units of the respective D/ρh values is color coded from blue to red. The three artifacts seen in each figure are due to the presence of the shakers.

Next, we apply the orthotropic inversion algorithm as described in Eq. (8). Fig. 18 shows the inversions yielding the three stiffness parameters $D_x/\rho h$, $D_{xy}/\rho h$, and $D_y/\rho h$, respectively, mapped spatially over the homogeneous wooden plate. As can be seen, away from the three shaker positions, each inversion correctly produces a spatially uniform stiffness parameter. In Fig. 19 we show the inversion results for the flawed plate. As can be seen, all three inversions successfully detect and localize the rectangular internal inclusion through the three D coefficients. From the perspective of contrast, the inversion yielding $D_y/\rho h$ seems somewhat superior in performance to that for $D_x/\rho h$ or $D_{xy}/\rho h$. This is perhaps related to the fact that the displacement response may be determined predominantly through D_y as appears to be the case based on the modal spatial patterns seen in Fig. 16. For example, from these displays we find an estimate of the dominant structural wavenumber, k, to be consistent with $\omega/k = \omega^{1/2} (D_y /\rho h)^{1/4}$, the latter being the phase speed of a flexural wave in a plate with stiffness given by D_y. In any case, these results confirm the efficacy and correctness of our extension of the flexural wave inversion technique to the orthotropic case.

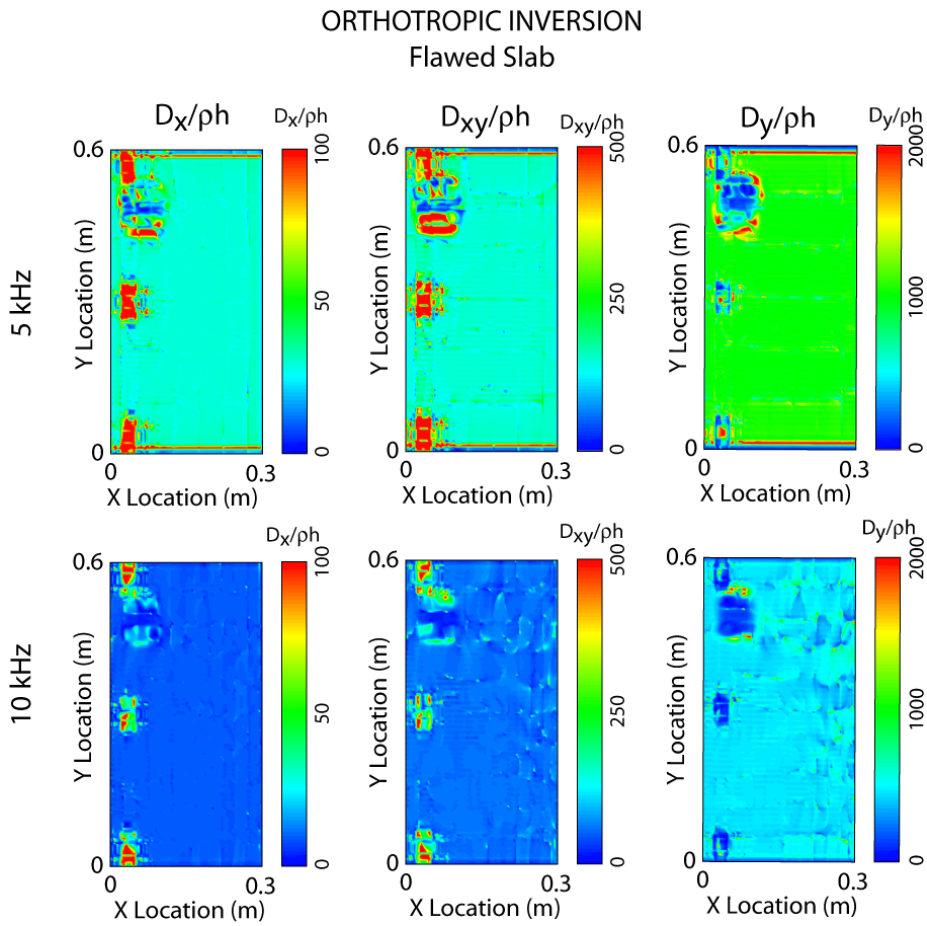

Figure 19. Result of applying the weak flexural wave inversion operator (WFWI) developed for the orthotropic case, Eq. (11), to the displacement data at each frequency for the flawed wooden plate to obtain the three stiffness parameters $D_x/\rho h$, $D_{xy}/\rho h$, and $D_y/\rho h$. The magnitude of the inversion in units of the respective D/ρh values is color coded from blue to red. The three artifacts again seen in each figure are due to the presence of the shakers. The flaw which is located in the upper left of the wooden plate can be seen in each display.

Although not unexpected, the actual numerical values for the D's obtained through the inversions are different from the values used in the forward finite element calculations. At 5 kHz the ratios of the values obtained through inversion to the known values are 0.4, 0.5, and 0.6 for D_x, D_{xy}, and D_y, respectively, and at 10 kHz 0.1, 0.2, and 0.3. We surmise that these inconsistencies are related to the use of the thin plate approximation inherent in the free-space wave equation, Eq. (7), which is increasingly in error as frequency increases. For example, Cremer and Heckl[26] argue that failure in this approximation results in less than a 10 % difference in the computed flexural wave speed when the flexural wavelength, $\lambda_f > 6h$. At 5 kHz, for our plate thickness we have $\lambda_f/h \sim 8$ and 3.7 in the y and x directions, respectively and the thin plate approximation is beginning to breakdown, albeit weakly. However, at 10 kHz we have $\lambda_f/h \sim 5.9$ and 2.7 for y and x directions. The computed flexural wave speeds are now off by 10 % or more, and this should begin to have a significant impact on the inversions. A rough argument as to the magnitude of this error can be made by thinking of the inversion operator as a λ estimator and recognizing that a generalized modulus, M, would be given by $M = \rho C^2$ with $C = \lambda\omega/2\pi$. Accordingly, a 20 % error in λ (or C) would give about a 40 % error in the stiffness. We believe

that this is probably responsible for the large error in the *D* coefficient values at 10 kHz. In any case, our goal in the inversions is to detect spatial anomalies in the local stiffness and thus to detect the presence of a fault causing this variation. In this respect, errors in the magnitude of the stiffness obtained as a by-product of the inversions are not of any serious consequence.

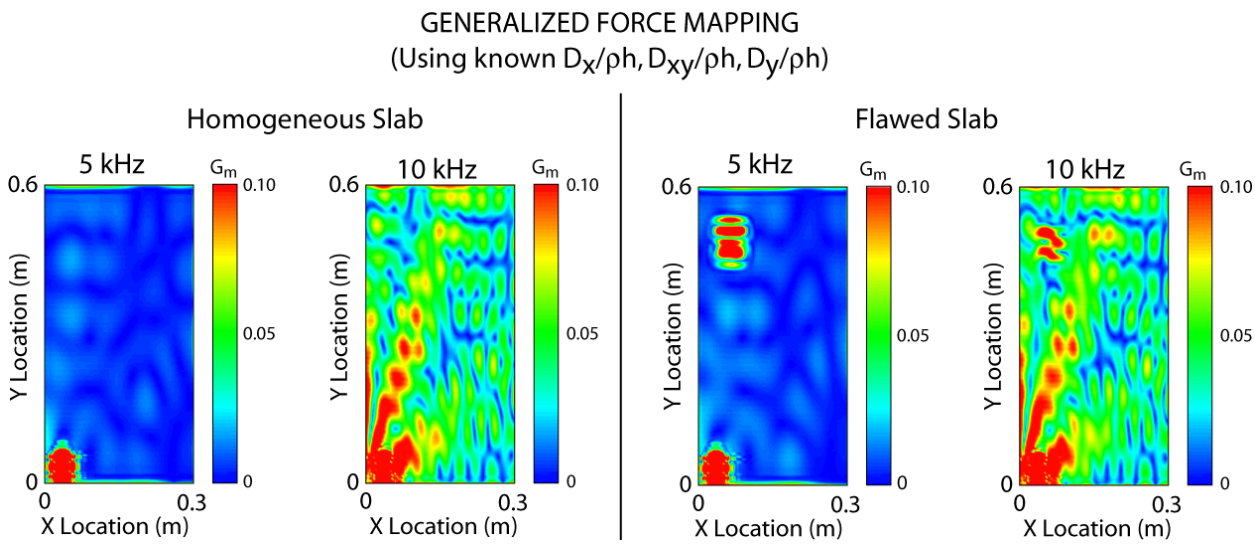

Figure 20. Result of applying the generalized force mapping operator (GFM) developed for the orthotropic case, Eq. (12), to the displacement data at each frequency for the homogeneous and flawed wooden plates when the driver in the lower left is excited. The resulting generalized force values are shown color coded from blue to red. The operator defined in Eq. (12) has been determined inserting the values for Dx/ρh, Dxy/ρh, and Dy/ρh that were used in the forward finite element calculation of displacements. The highlight seen in each figure in the lower left is due to the presence of the shaker. The inclusion located in the upper left of the flawed wooden plate can be seen best in the 5 kHz result.

Consider next the generalized force method. Inserting the known (i.e. those used in the numerical calculations) values for $D_x/\rho h$, $D_{xy}/\rho h$, and $D_y/\rho h$ into Eq. (9), we now apply the GFM algorithm to the numerical displacement data. As can be seen in Fig. 20, the algorithm is very effective at detecting and locating the internal fault at 5 kHz. Once again the results at the higher frequency are worse, and this time they almost completely fail. Earlier we saw that the inversions produced values for the *D* coefficients which were different from those used in the calculations, presumably from the effect of the thin plate approximation, and that these differences grow with increased frequency. We expect that this effect is responsible for the very poor result observed in the GFM processing at 10 kHz. In the section on adaptive algorithms, we will show how this problem can be eliminated.

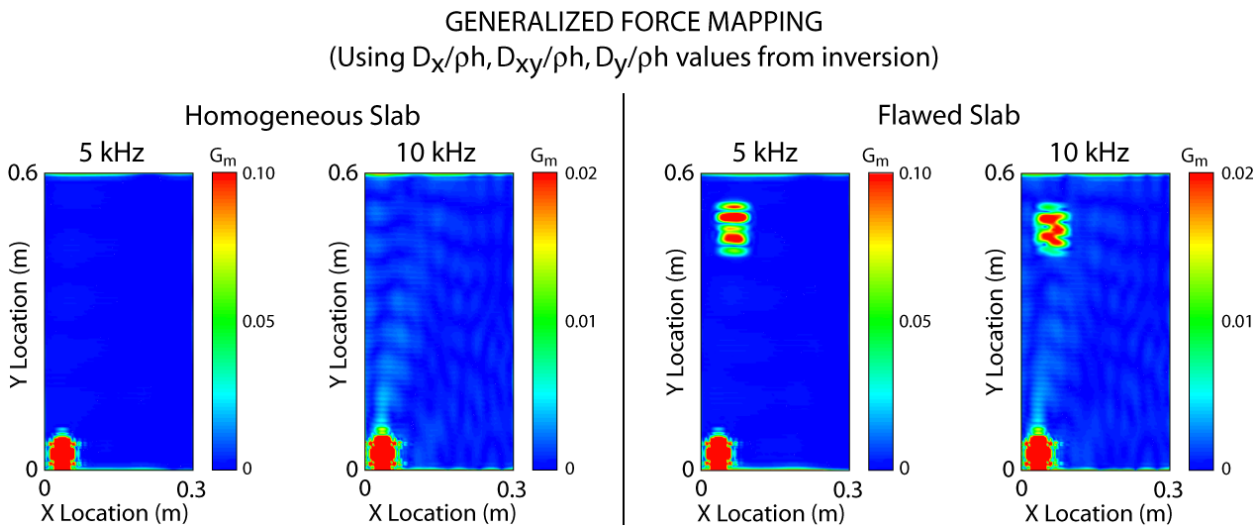

Figure 21. Result of applying the generalized force mapping operator (GFM) developed for the orthotropic case, Eq. (12), to the displacement data at each frequency for the homogeneous and flawed wooden plates when the driver in the lower left is excited. The resulting generalized force values are shown color coded from blue to red. The operator defined in Eq. (12) has been determined inserting the values for Dx/ρh, Dxy/ρh, and Dy/ρh that were obtained by applying the inversion operator to the displacement data. The highlight seen in each figure in the lower left is due to the presence of the shaker. The inclusion located in the upper left of the flawed wooden plate can be clearly seen at both frequencies.

Adaptive Algorithms

We saw earlier in the case of the wood slab that even though the orthotropic inversion operators successfully detected the internal flaw the stiffness parameters obtained through the inversion were somewhat different from those used in the finite element simulation. This was not unexpected in that the thin plate equations upon which the flexural wave inversion operator was based begin to fail at the frequencies used in the study. Further, the Generalized Force method began to fail as well. In particular, when we inserted the known (i.e. those used in the numerical calculations) values for $D_x/\rho h$, $D_{xy}/\rho h$, and $D_y/\rho h$ into Eq. (9) and applied the GFM algorithm to the numerical displacement data, as was seen in Fig. 20, the algorithm was very effective at detecting and locating the internal fault at 5 kHz. But the results at the higher frequency were considerably worse.

Adaptive GFM by Prior Inversion

In addressing this problem, we conceived of a new "adaptive" approach which could mitigate the effect of poorly known or even unknown equations of motion. The approach uses the flexural wave inversion and GFM operators sequentially in the following manner. In place of inputting the known values for the D's, we subsequently used the values produced by the flexural wave inversions and then applied the GFM algorithm; this result is shown in Fig. 21. Notice that the results at 10 kHz are no longer degraded. In fact, even the already good results at 5 kHz are now improved. Apparently, differences associated with the onset of failure of the thin plate approximation have been in a sense "corrected" in an *adaptive* sense by the inversion choosing coefficients in the wave equation (Eq. (4)) which more correctly describe the dynamics at that

particular frequency. In fact, we have been developing a more generalized adaptive inversion algorithm which works in this way.

In a second approach, we developed an algorithmic method which can potentially be trained for any surface, medium, or structure and does not rely on any a priori knowledge of the equations of motion. In this approach, we define a set of equations each with a specific operator and associated unknown coefficients, and set these equations equal to the displacements. As they appear, they resemble a set of homogeneous equations of motion with arbitrary coefficients. The displacements and their corresponding derivatives must be determined with a sufficient number of independent inputs such that the coefficients for each of the equations in the set can be solved for in a linearly independent fashion. We demonstrated that the one equation out of the entire set which is the most "appropriate" model is that whose coefficients have a minimum normalized variance within a known region of homogeneity. After having determined these "trained" coefficients, they may be utilized in the Generalized Force Mapping (GFM) technique. As the algorithm is calculated elsewhere within a medium or on a structure, if the material parameters are constant and/or there are no flaws, inclusions, or actuators, a minimized local residual will arise from the equation. In the event that the material parameters fluctuate or if there are any flaws, inclusions or actuators, a distinct and quantitatively different residual will result. The principle is identical to that which was used previously for plates, however here we have developed a corresponding generalized equation with arbitrary coefficients which can potentially adapt to any structure or situation. The coefficients are solved for using the Conjugate Gradient Least Squares (CGLS) algorithm, which is particularly efficient in the solution of ill-conditioned systems of equations or noisy data. It should be mentioned that the coefficients determined from this generalized training procedure may or may not be directly correlated with the concept of material parameters such as stiffness or flexural rigidity due to issues such as thickness, boundary condition effects, depth profiles of flaws, porosity, locally heterogeneous materials such as amorphous media, etc. In particular cases, however, they will identically represent such physical quantities.

The Fundamental Concept – Adaptive Coefficients

We begin by defining an equation based on an arbitrary set of spatial derivatives operating on known displacements with unknown coefficients and set this equation equal to the displacements as

$$M(\vec{r},\omega)\cdot L\left(\vec{u}(\vec{r},\omega)\right)=\omega^2\vec{u}(\vec{r},\omega). \tag{10}$$

In this expression, the vector $M(\vec{r},\omega)$ represents the coefficients while the expression $L\left(\vec{u}(\vec{r},\omega)\right)$ represents the operator providing the specified set of spatial derivatives on the data, $\vec{r}$ is the position vector and ω the radial frequency of dynamic excitation. Both vectors are of identical, yet arbitrary length. As it appears, it resembles a generalized homogeneous equation of motion with unknown coefficients, where $M(\vec{r},\omega)$ represents a parameter divided by the density, and possibly thickness. These components are then provided using a sufficient number of inputs such that the coefficients can be solved for, thereby "training" the algorithm to develop an appropriate "characteristic equation of motion" i.e.

$$M(\vec{r},\omega)=\omega^2\cdot L^{-1}\left(\vec{u}(\vec{r},\omega)\right)\vec{u}(\vec{r},\omega). \tag{11}$$

When the coefficients are determined by training the algorithm on a region of a structure where there are no faults, they are then considered to be independent of position. As the algorithm is calculated elsewhere on the structure utilizing these same coefficients, a non-zero value labeled as $G_m(\vec{r},\omega)$ will arise from the equation where a local force or a fault is present, or if the material parameters fluctuate. The principle is identical to that underlying the GFM algorithm described above; however in this new approach, we have developed a corresponding generalized equation with unknown coefficients which can adapt to any structure or situation. The resulting cases may be represented as

$$M(\omega)\cdot L^{-1}\left(\vec{u}(\vec{r},\omega)\right)-\omega^2\vec{u}(\vec{r},\omega)=\begin{cases}0, \text{ if the plate is homogeneous}\\ G_m(\vec{r},\omega)\text{ if a force or flaw is present}\end{cases} \tag{12}$$

The variational form of Eqs. (11) and (12) may also be obtained as previously presented, and initial results indicate that this representation, once again, tends to reduce the effects of noise in the process of obtaining spatial derivatives from measured data. Additionally, the system may be overspecified in the solution of Eq. (10) for the unknown coefficients, $M(\vec{r},\omega)$ and in this context, the CGLS Algorithm is utilized, since it has been shown to be useful in the solution of ill-conditioned systems of equations or noise contaminated data. As mentioned above, the coefficients determined from this generalized training procedure may or may not be directly correlated with the concept of material parameters such as stiffness or flexural rigidity. In particular cases, however, they will identically represent such physical quantities.

The Training Criteria

For a region of known homogeneity, Γ_H, the coefficients associated with the most appropriate solution will have a minimum variance normalized by the mean square value. Explicitly, we define the *mean value* within the homogeneous region for each coefficient $M_i(\vec{r},\omega)$ of equation *j*, (labeled $M_{ij}(\vec{r},\omega)$,

$$\mu_{M_{ij}}(\omega)=\frac{\int_{\Gamma_H} M_{ij}(\vec{r},\omega)\,dS}{\int_{\Gamma_H} dS}. \tag{13}$$

We define the *variance* within this same homogeneous region as the mean square value about the mean which can be represented as

$$\sum_{M_{ij}}^{2}(\omega)=\int_{\Gamma_H}[M_{ij}(\vec{r},\omega)dS-\mu_{M_{ij}}(\omega)]^2\,ds\,. \tag{14}$$

Therefore, the equation out of the entire set for which

$$\frac{\sum_{M_{ij}}^{2}(\omega)}{\mu^2_{M_{ij}}(\omega)} \tag{15}$$

is a minimum is the best fit for the "optimized" equation of motion. Once these coefficients, $M_{\min}(\omega)$, have been found, they are assumed to be spatially independent, and can be implemented in the GFM algorithm as shown above in Eq. (12).

Below we show examples of such "test" equations of motion with arbitrary coefficients, restricting ourselves to a two-dimensional domain.

Consider the following set of equations:

$$M_{1,1}\left(\frac{\partial^2 u_z}{\partial x^2}+\frac{\partial^2 u_z}{\partial y^2}\right)=\omega^2 u_z \tag{16}$$

$$M_{1,2}\left(\frac{\partial^2 u_z}{\partial x^2}\right)+M_{2,2}\left(\frac{\partial^2 u_z}{\partial y^2}\right)=\omega^2 u_z \tag{17}$$

$$M_{1,3}\left(\frac{\partial^2 u_z}{\partial x^2}+\frac{\partial^2 u_z}{\partial xy}+\frac{\partial^2 u_z}{\partial y^2}\right)=\omega^2 u_z \tag{18}$$

$$M_{1,4}\left(\frac{\partial^2 u_z}{\partial x^2}\right)+M_{2,4}\left(\frac{\partial^2 u_z}{\partial xy}\right)+M_{3,4}\left(\frac{\partial^2 u_z}{\partial y^2}\right)=\omega^2 u_z \tag{19}$$

$$M_{1,5}\left(\frac{\partial^4 u_z}{\partial x^4}+2\frac{\partial^4 u_z}{\partial x^2 y^2}+\frac{\partial^4 u_z}{\partial y^4}\right)=\omega^2 u_z \tag{20}$$

$$M_{1,6}\left(\frac{\partial^4 u_z}{\partial x4}\right)+M_{2,6}\left(\frac{\partial^6 u_z}{\partial x^2 y^2}\right)+M_{3,6}\left(\frac{\partial^4 u_z}{\partial y^4}\right)=\omega^2 u_z \tag{21}$$

The first equation (Eq. (16)) is a two-dimensional Laplacian representing a plane shear wave propagating in the *x-y* plane. In this instance, the coefficient, $A_{1,1}$, would represent the shear modulus divided by the density μ/ρ. The second equation (Eq. (17)) is also based on the same two-dimensional Laplacian, yet is allowed to have independent coefficients for each derivative, $A_{1,2}$ and $A_{2,2}$, respectively; therefore we may label this equation as an "anisotropic shear" equation. Equation. (18) is similar to Eq. (16); however it has an additional term representing the partial derivatives with respect to *x* and *y*, while it has one coefficient, $A_{1,3}$. Equation (19) is similar to Eq. (18); however it has three coefficients, one for each derivative, $A_{1,4}$, $A_{2,4}$ and $A_{3,4}$, respectively. Equation (20) is the fourth order plate equation wherein the single coefficient, $A_{1,5}$, represents the flexural rigidity divided by the density and the plate thickness such as $D/\rho h$. Equation. (21) is also a fourth order plate equation; however this representation is appropriate for thin, orthotropic plates, wherein $A_{1,6}=D_x/\rho h$, $A_{2,6}=(D_{xy}/\rho h)$ and $A_{3,6}=D_y/\rho h$, respectively.

Initial studies utilizing earlier data demonstrate that this algorithm is robust in the presence of noise and should be adaptable to many situations in fault detection and material parameter variation. In particular, we used three existing data sets for proof of concept: interior displacements maps on agar tissue phantoms taken with magnetic resonance elastography and surface displacement maps on steel plates and on wooden slabs generated numerically. In this study we used three of the above model equations namely the isotropic shear, isotropic plate, and

orthotropic plate equations. Figures 22-24 show how the adaptive algorithm correctly selects the correct equation of motion for each case, where the correct equation is the one having the least variance (indicated by the red box).

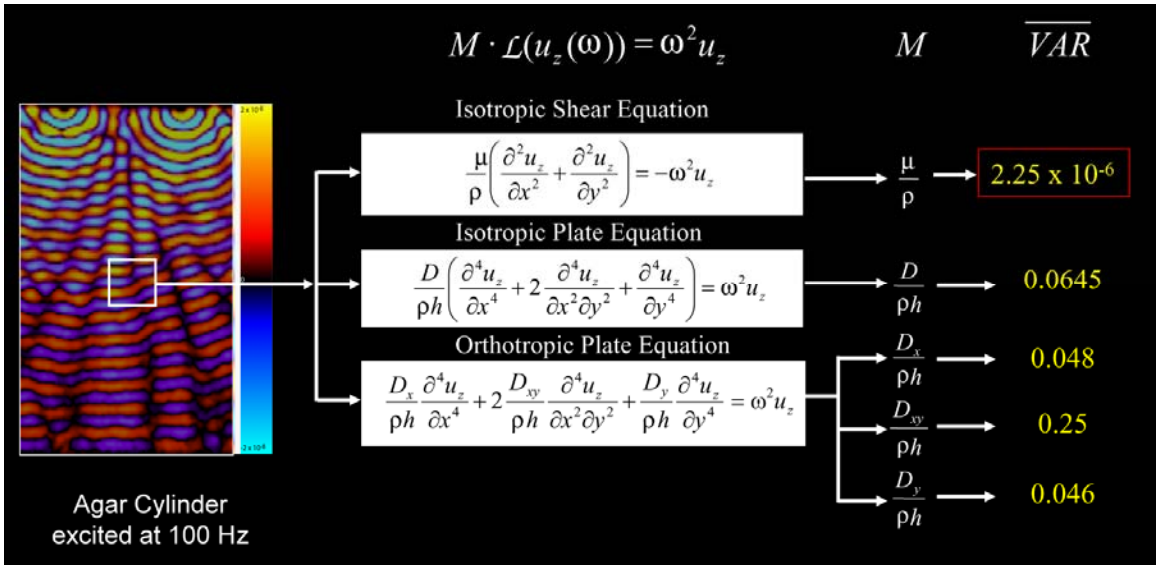

Figure 22. Adaptive algorithm chooses correct shear wave equation upon locally sampling 2-D slice of internal displacement map measured in Agar using magnetic resonance elastography.

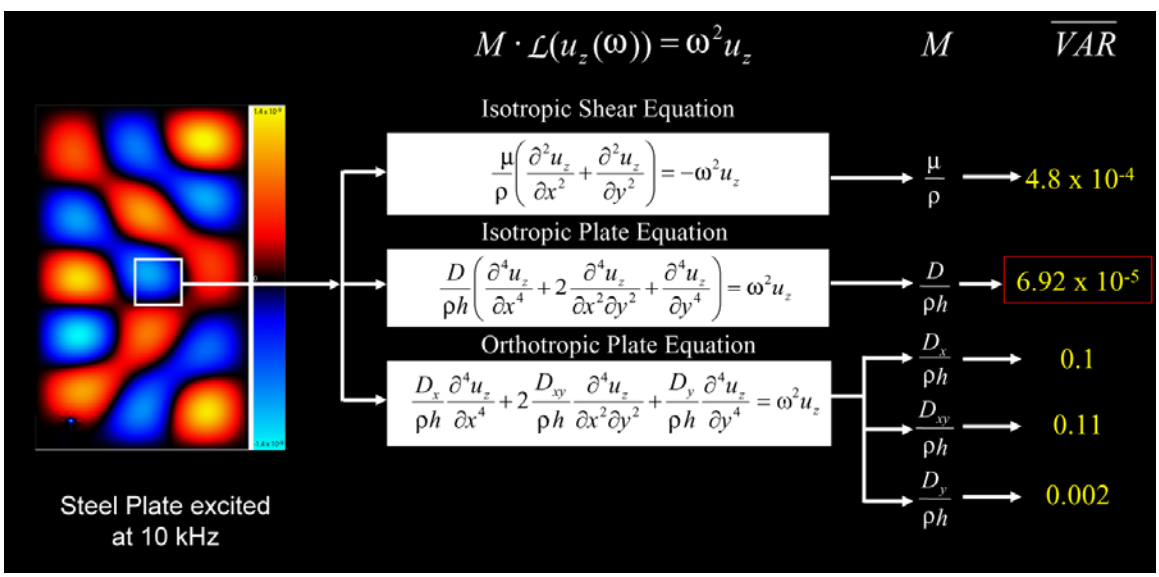

Figure 23. Adaptive algorithm chooses correct isotropic plate wave equation upon locally sampling surface displacement map computed by finite element model.

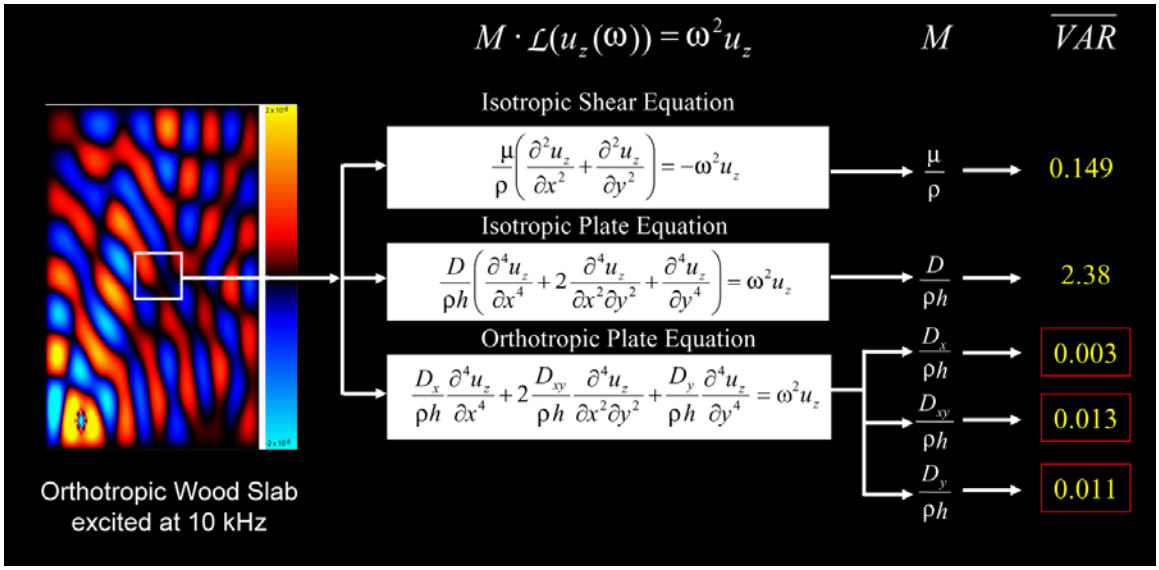

Figure 24. Adaptive algorithm chooses correct orthotropic plate wave equation upon locally sampling surface displacement map computed by finite element model.

Modern Classifiers

We also explored albeit briefly the potential for exploiting modern identification (ID) algorithms that use feature spaces derived from the displacement maps or from the spatial images derived from the previously described algorithms. The Physical Acoustics Branch has extensive experience in applying such ID algorithms in our on-going work[10-14] on underwater mine and UXO identification. These algorithms include hidden Markov models (HMM), relevance vector machines (RVM), and kernel matching pursuits (KMP). We expected that application of these algorithms as well as fusion of their modalities might provide both improved performance for fault detection and material parameter determination as well as determination of depth profiles of faults or material parameter fluctuations. Given the larger efforts we executed on what we perceived to be the more promising aspects of our SEED effort, we explored only some simple Fourier-transform derived features from the plate data. This simple effort was not successful. However, we continue to believe there is some potential in these techniques, but their merits will have to be explored in a future effort.

Plaster Dome Ceiling

Another area we explored involved plaster domed ceilings. In the SEED study, we used a simulated data base of surface vibration generated using an advanced structural acoustic finite element-based code. In particular, we explored application of the speaker-based technique to what we consider to be a generic domed ceiling – a common structure found in historic buildings and residences - in which a plaster layer is attached to, and takes the shape of, a backing structure considered to be relatively rigid such as brick or mortar.

Ceiling Structure

The ceiling structure (Fig. 25a) is modeled as a three-dimensional thin shell enclosing a volume of air. The geometry of the shell is that of half an ellipsoid with radii along x, y, and z directions given by 4.2164 m, 4.2164 m, and 1.9304 m, respectively, with a uniform thickness *t* of 0.0254 m. The somewhat shallow 3-D elliptical shape is a common dome geometry since a 13-20 % rise-to-diameter ratio guarantees virtually no bending moments. The shell is considered made of plaster which is modeled as a linear visco-elastic material having density ρ of 1444 kg/m^3, Young's modulus E of 7 GPa, Poisson's ratio σ of 0.2 and uniform damping of 2%. The air inside has density 1.25 Kg/m^3 and speed of sound 320m/s. The ceiling base (where a real ceiling would meet a supporting wall) and the outer surface (where it would meet and attach to the mortar or brick foundation) are considered rigidly fixed, and the system is subjected to acoustic excitation from a point source located 0.5 m below the center of the base of the ellipsoidal volume (Fig. 25b).

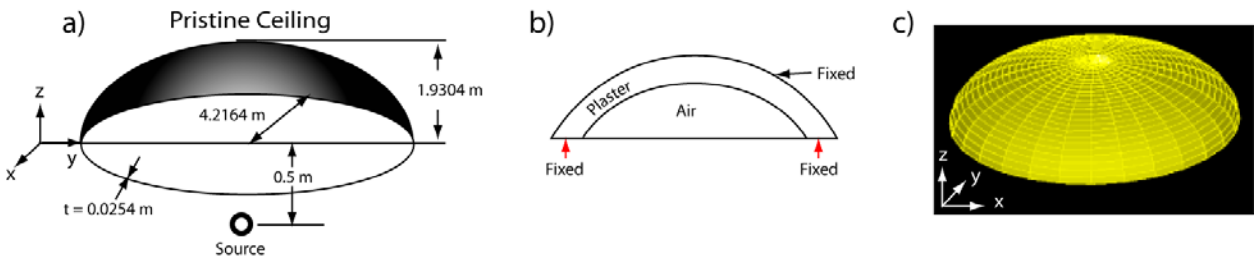

Figure 25. (a) the geometry of the elliptical ceiling and location of the acoustic source (viewed from beneath the ceiling); (b) the boundary conditions assumed in the finite element calculation; (c) the mesh used in conjunction with the hp-finite element code (viewed from above the ceiling).

Numerical Code

The coupled structural acoustic response is computed using the parallel hp-version finite element code STARS3D (Dey et. al.[27], Dey and Datta[24]) which utilizes high-order basis functions to achieve accurate results. This is necessary since in the frequency regime studied here (100 Hz to 400 Hz), structural wavenumber-thickness products reach values as high as ~ 90. For models with fixed low-order h-approximations, one must use a spatial mesh with enough refinement to satisfy the requirement of a certain number of elements per wavelength. We use a p-version approach where the dispersion error can be controlled by increasing the polynomial degree of approximation (*p*) for a fixed spatial mesh refinement (*h*). Accordingly, we use a spatial mesh (Fig. 25c) that approximates the curved shell-geometry well and then execute a p-convergence study to determine the proper polynomial degree of approximation (*p*) to use with the mesh at hand. For the present model, a p-convergence analysis indicated numerical converged solutions at cubic ($p = 3$) approximations. The numerical model is solved at 100 Hz, 200 Hz, 300 Hz, and 400 Hz to determine the complex-valued three-dimensional displacement field on the surface of the ceiling in contact with the air inside.

Ceiling Conditions

Three ceiling conditions are modeled: (1) *Pristine Ceiling*: In this model, depicted in Fig. 25b, the homogeneous ceiling is considered rigidly attached to the backing throughout the outer boundary. This implies no motion along the portions marked 'fixed'. (2) *Partial detachment*: In this model, a portion of the outer boundary of the ceiling is fully detached from the rigid backing and the boundary condition is considered to be free. The shape and location of this free patch, shown as the shaded area in Fig. 26a, resulted from the desire to have both a non-axisymmetric defect shape and the ability to derive it based on the geometric model and mesh already used for the homogeneous ceiling finite element model. To achieve this in a straightforward manner we isolated a circular portion of the homogeneous mesh and selected one quarter of it to be the defect patch region. Fig. 26b illustrates the boundary condition for this case which implies free motion of that portion of the boundary marked 'free'. (3) *Embedded deconsolidation*: In this model, depicted in Fig. 26c, we consider a small pocket of heavy fluid with the same shape and location as that of the detached segment. The thickness of the pocket, whose center is located midway through the plaster layer, is one third of the total ceiling thickness. The fluid defect, with density 1444 kg/m^3 and wave-speed 1175 m/s (compressibility = 2 GPa), is taken to represent plaster deconsolidation at least in a simple sense.

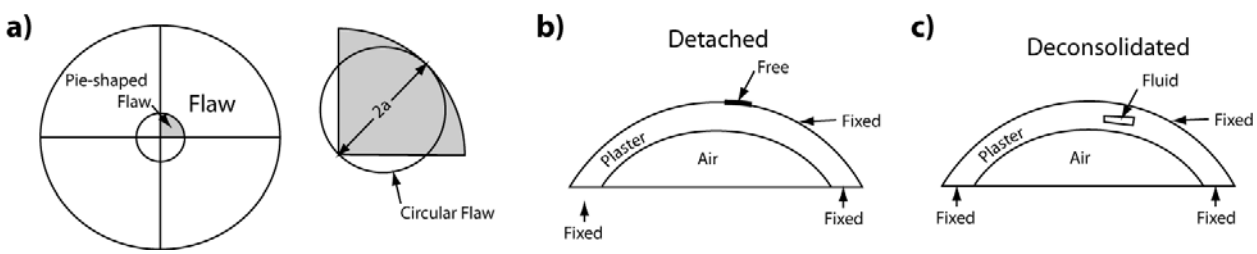

Figure 26. (a) the geometry of the defect (plan view from above the ceiling). The insert shows a circular flaw having the same area as the pie-shaped flaw; (b) the boundary conditions for the ceiling with detached defect; (c) the boundary conditions for the ceiling with deconsolidated defect.

Analysis & Results

In order to establish a response baseline, we calculate the surface displacement level for the case of an infinite flat plaster plate of thickness t under the action of an applied static pressure. For pressure P the displacement, W, would be given by

$$W \sim \frac{-Pt(1-\sigma-\sigma^2)}{E} \tag{22}$$

The finite element-based numerical simulation has modeled a pressure of 1 Pa at the source point (i.e. at a position 0.5 m below the plane at which the ceiling begins) which with spherical spreading would become $(2.43)^{-1}$ Pa at a point at the plaster surface directly above the source. For this pressure, E = 7 GPa, and t = 2.54 cm, using Eq. (22) we obtain $W \sim 0.8 \times 10^{-12}$ m.

With this base displacement level established, we now examine the normal displacement maps produced from the dynamic numerical simulation for the unflawed elliptical ceiling (Fig. 27). We consider only the normal displacements since in an actual experimental study the typical laser Doppler vibrometer would measure only this normal vibration component. As can be seen, at all four frequencies studied, the numerical computations predict somewhat complicated, nearly circularly symmetric response patterns.

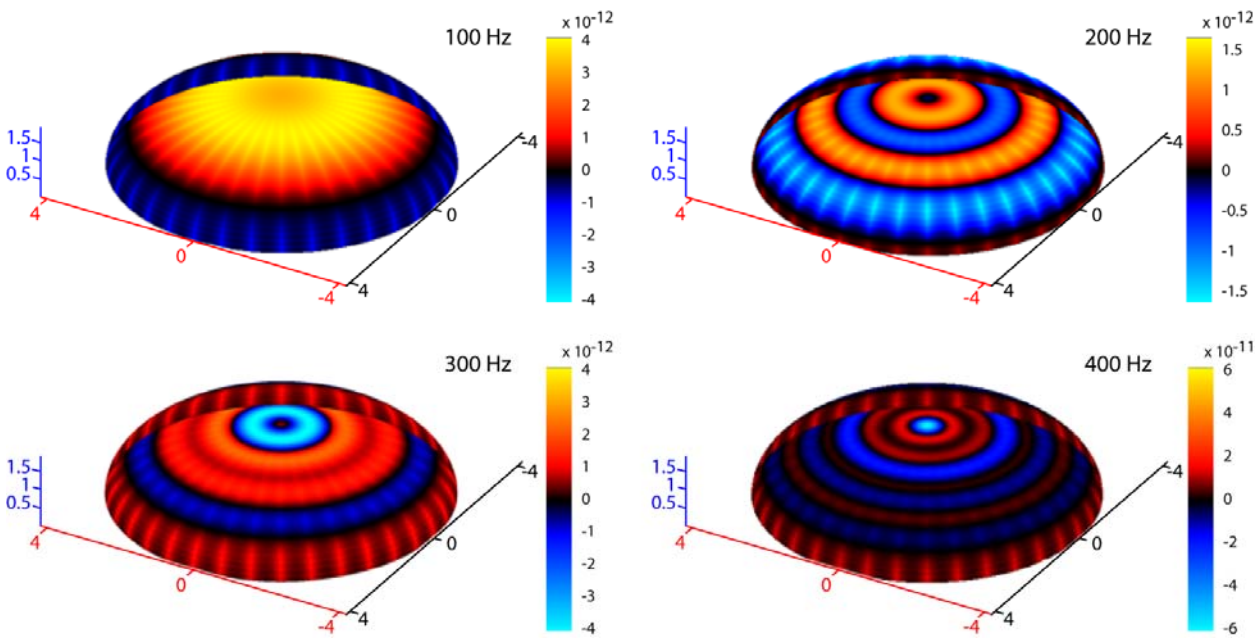

Figure 27. Normal displacement levels for the unflawed ceiling calculated with the STARS3D code for four frequencies (displayed on the exposed surface of the ceiling).

We find that these circularly symmetric frequency dependent response patterns (Fig. 27) are in fact what one would expect for the pressure interference patterns produced and determined by reflections from the elliptical ceiling surface and the incident spherical wave. Further, the azimuthally dependent superposed weaker patterns are related to elastic wave effects in the plaster layer. To test this reasoning, we also used the finite element structural acoustic code to compute the pressure on the same elliptical surface for the case in which the plaster itself is rigid, and these are shown in Fig. 28. The computed pressure patterns are almost identical to those shown in Fig. 27 for the unflawed ceiling displacements; in addition, the weaker azimuthally dependent response is now missing. Further, we find that normalizing the displacement levels shown in Fig. 27 by the pressure levels in Fig. 28 produces average normalized responses over the ceiling very close to 3×10^{-12} m/Pa which is the same value obtained for $W/P = t(1 - \sigma - \sigma^2)/E$ from Eq. (22) using our specific ceiling parameters. These facts support our contention that the prominent ceiling response patterns are related to acoustic interference and focusing effects

determined by the ceiling geometry while the much weaker structure is associated with elastic wave propagation and modal effects in the plaster layer.

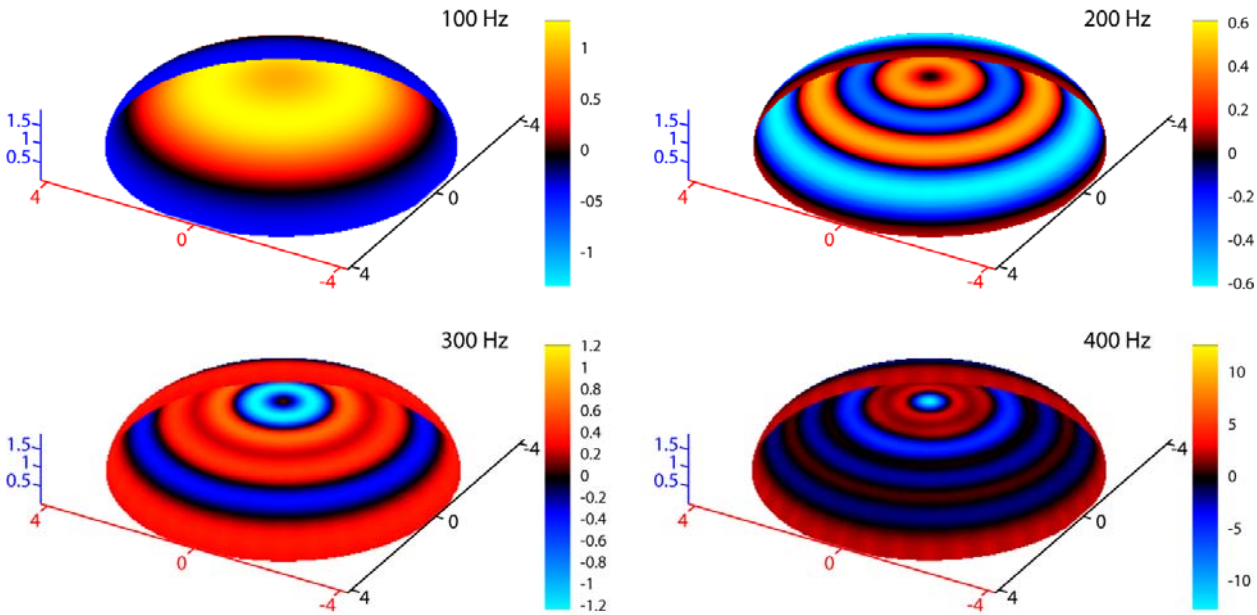

Figure 28. Surface pressure levels for a perfectly rigid elliptical ceiling calculated with the STARS3D code for four frequencies (displayed on the exposed surface of the ceiling).

This is in contrast to the case in which shakers (See Refs. 1,3) are applied to the structure locally wherein elastic waves propagating in the plaster layer and modal responses are the cause of the observed frequency and spatially dependent displacement response functions. As is well illustrated here, in using an air-borne acoustic wave to excite the ceiling, not surprisingly the "architectural acoustics" will to a large extent determine the effective spatial distribution of the pressure applied to the ceiling, and one must take these effects into account when attempting to detect defects based on local variations in the acoustically forced displacement. Of course, these patterns would be affected by both additional returns in an actual room enclosed by walls and by changes in the position of the source. These pressure interference effects could be problematic in that they can serve to confuse attempts to detect and localize a defect by direct observation of the abrupt increase in displacement level associated with a mobile flaw.

Detached Defect

Before reviewing the numerically simulated dynamic response data associated with these flaws, we estimate the displacement response one would expect for acoustically-forced detached layers and how this might depend on defect size. This is of interest since defect displacement amplitudes sufficiently high compared to the levels produced on the non-flawed areas could be

detected and localized simply by direct observation of the displacement maps themselves without further need of post-processing.

We are able to determine this in an approximate sense using available expressions in the literature for the deflection under static loading of simple geometries obeying ideal, but we think relevant, boundary conditions. In particular, we consider a circular detached plate segment of radius a in an otherwise unflawed flat plaster plate of uniform thickness, t, under the action of a uniform static pressure, P, and for fixed boundary conditions over the circular edge of the defect. For this case, the center displacement, W_C, of the defect is given by Young[28] as

$$W_C = \frac{Pa^4}{64D} \tag{23}$$

where D is the flexural rigidity given by

$$D = \frac{Et^3}{12(1-\sigma^2)} \tag{24}$$

For the above case, the ratio of the defect center displacement to the plaster layer displacement away from the defect is then given from Eqs. (22)-(23) as

$$\frac{W_C}{W} \sim \frac{3}{16}(1+\sigma)\left(\frac{a}{t}\right)^4 \tag{25}$$

We plot this expression as a function of a for three different plaster thicknesses in Fig. 29. In order that the defect displacement be clearly pronounced above any spatial structure in the plaster layer displacement maps (such as seen in Fig. 27), we require the ratio W_C / W to be large, say ≥ 4. Equation. (25) in turn requires that

$$\frac{a}{t} \geq 2\,. \tag{26}$$

The minimum directly visible defect size defined by Eq. (26) is then seen to be directly proportional to the plaster thickness, t. For our 2.5 cm thick plaster ceiling, Eq. (26) implies that defect sizes (i.e. $2a$) of about 10 cm or greater should be directly visible in the scanned displacement data. The corollary is that much smaller defects (« 10 cm's) will not stand out against the background displacement, and post processing methods such as flexural inversion (Bucaro, et. al.[4]) will be required for their detection. The analysis so far pertains to defect size requirements necessary for sufficient contrast between the background ceiling

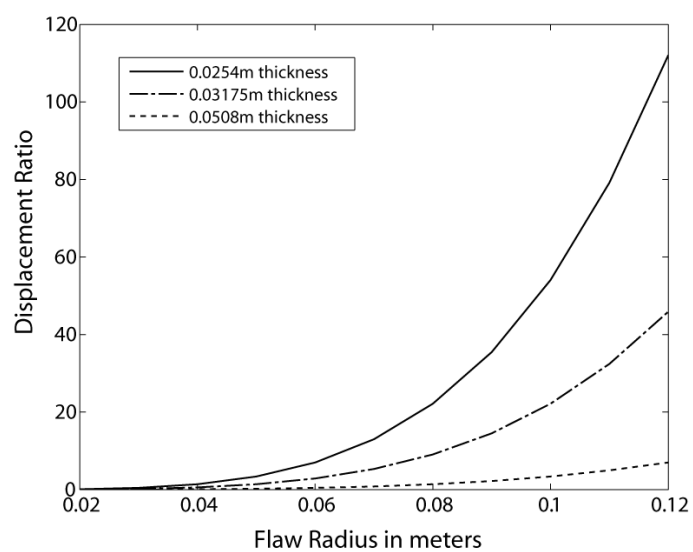

Figure 29. The ratio of detached flaw displacement to that of the healthy ceiling versus the circular flaw radius computed from the static expression of Eq. (25) for three plaster thicknesses.

displacements and those associated with the defect. We will discuss in the final section minimum displacement levels required for detection by a typical SLDV system.

The above argument is based on a static response analysis expected to be sufficient at frequencies well below the first mechanical resonance of the defect. If, however, the dynamic acoustic excitation excites a defect resonance, levels higher than those predicted above could be experienced. One can estimate the fundamental resonance frequency, f_R, of the disk-shaped defect using a lumped-mass approximation wherein the spring constant, k, would be given as $P\pi a^2/W_C$ and the mass, m, as $\pi\rho t a^2$. Then with the help of Eq. (23) we have

$$\omega_R = 2\pi f_R = \sqrt{\frac{k}{m}} = 4\pi^{-1} t a^{-2} \sqrt{\frac{E}{3p(1-\sigma^2)}}\,. \tag{27}$$

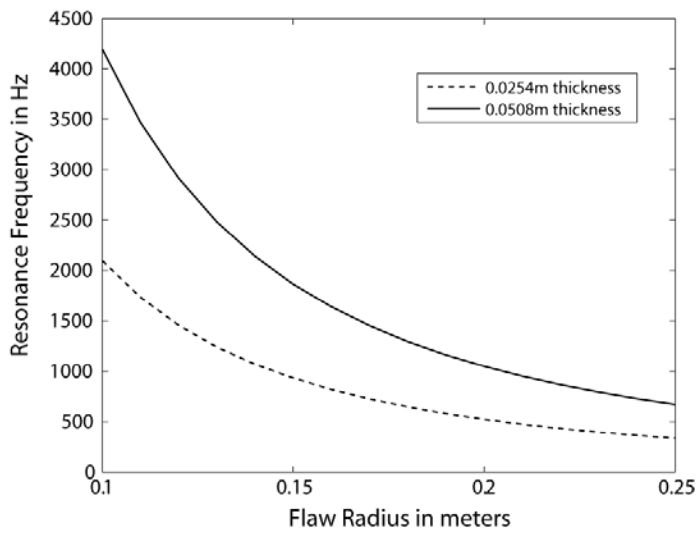

Figure 30. The resonance frequency versus circular flaw radius computed using Eq. (27) based on a lumped parameter model for two plaster thicknesses.

We plot this expression as a function of a in Fig. 30 for two plaster layer thicknesses. As can be seen, for the plaster thickness used in the simulation (t = 0.0254m), defect sizes with diameters of about 0.5 m would resonate within our current band and thus have higher displacement levels than predicted statically. However, relying on the use of resonant excitation to lower the minimum observable defect size (~10 cm for t = 0.0254m) predicted by Eq. (26) would require very high frequencies as can be seen from Eq. (27) which gives f_R > 8.4 kHz for $2a$ < 10 cm. We will discuss these resonance frequency estimates further in the discussion of the dynamic response.

For each of the four frequencies, we show in Fig. 31 the numerically computed dynamic displacement maps for the detached ceiling resulting from the point source excitation. We point out that displays using the same scale factor as in Fig. 27 (although not shown here) show almost identical interference patterns away from the defect region as expected. As can be seen in Fig. 31, the defect stands out clearly, i.e. displacements over the defect are much larger than those over the healthy plaster, and the normal plaster displacements appear as almost black on the linear scale over which these are displayed. Although the defect shape used in the finite element computations is not circular but quasi-pie-shaped (chosen for convenience to be consistent with the grid structure), we note that its area would be approximately that of a flat circular disc with radius 25 cm (see the insert in Fig. 26a). For the latter, such a defect size has a/t = 10 which easily meets the requirement specified in Eq. (26) so that we should expect the displacement levels associated with the defect to dominate the spatial maps as indeed they do (Fig. 31). Using Fig. 27 to estimate the healthy plaster displacement near the flaw location, we find the contrast

ratio to be between 1500 and 1800 over our frequency range in agreement with Eq. (25) which predicts a ratio of 2000. We also point out that for this circular disc, the displacement predicted by the static expression (Eq. (23) is 6×10^{-9} m for a pressure of 1Pa. This compares well with the dynamic displacement of 4.3×10^{-9} m at 100 Hz if we note from Fig. 28 that the dynamic pressure at the flaw is about 1 Pa.

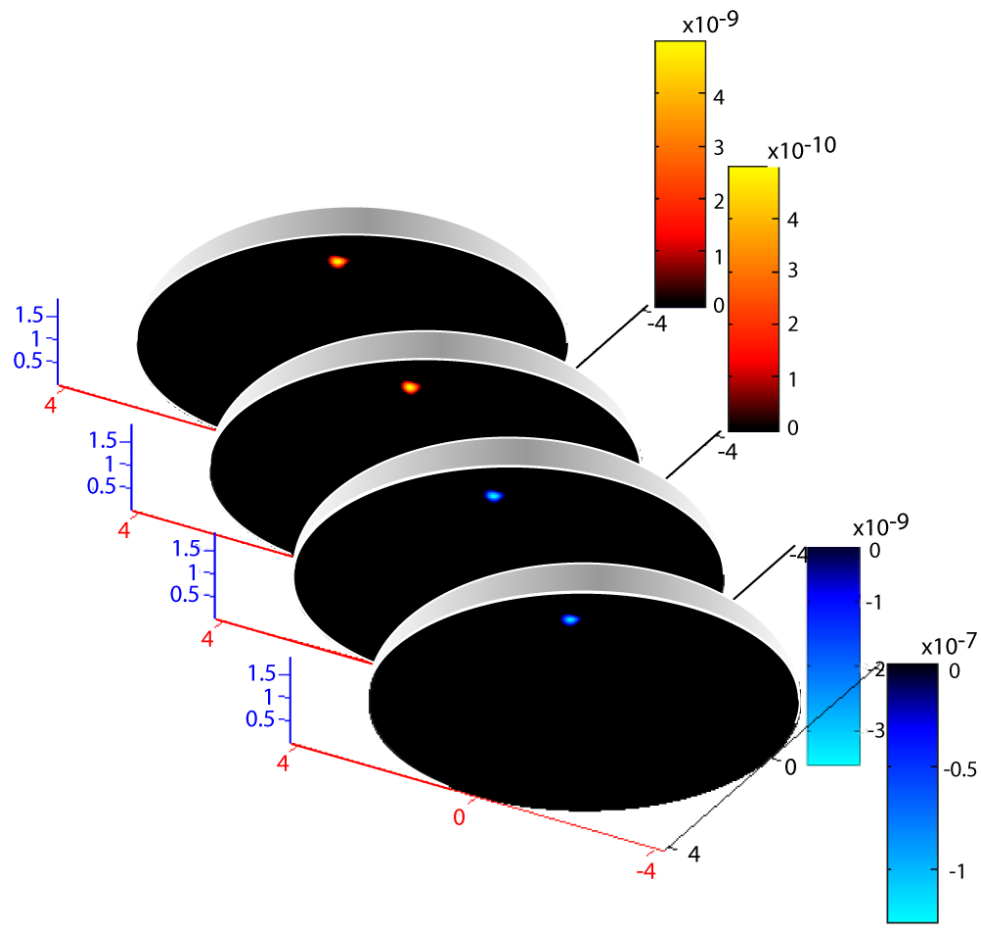

Figure 31. Normal displacement levels for the flawed ceiling (detached segment) calculated with the STARS3D code for four frequencies (displayed on the exposed surface of the ceiling).

In Table 3 we list the total normal force (real part) acting on the flaw as determined from integration of the pressures (shown in Fig. 28) over the area of the flaw. We then normalize the maximum detached flaw displacements (more clearly seen in the expanded display in Fig. 32a) by this force level and list these ratios in Table 3. As can be seen in the table, for the three lower frequencies these force-normalized displacement levels only increase weakly with frequency. However, as can be seen in column (d), the force-normalized response at 400 Hz is an order of magnitude higher. This would suggest that we are beginning to approach a resonance frequency. We say "suggest" because the actual response of the defect would not be simply proportional to the total force but would involve the spatial dependence of the force over the defect in some manner. Nonetheless, earlier using Eq. (27) we had estimated the fundamental resonance frequency of the defect as f_R = 336 Hz (with a = 25 cm, the radius of a disk whose area would be

approximately that of our pie-shaped defect). This is seen to be consistent with the conjecture that at 400 Hz we are near the first resonance of the detached segment. For much larger defects, our band would be well above f_R; and unless higher order resonances were excited, the resulting displacement levels would be greatly reduced from the levels predicted below resonance.

Table 3. Dynamic Displacements, Total Force Acting on Flaw, and Wavelengths

Frequency (Hz)	(a) Dynamic Fluid Flaw Displacement ($m \times 10^{-10}$)	(b) Dynamic Detached Flaw Displacement ($m \times 10^{-9}$)	(c) Total Force On Flaw (N)	(d) Force-Normalized Displacement (b)/(c) ($m \times 10^{-9}$/N)	(e) λ Flexural (m)	(f) λ Acoustic (m)
100	1	4.3	0.2	22	1.8	3.44
200	1.2	0.48	0.02	24	1.27	1.72
300	2.2	-3.2	-0.1	32	1.04	1.14
400	110	-90	-0.85	106	0.9	0.86

Before leaving detached defects, we point out that oftentimes a plaster wall or ceiling is formed in three or more layers. For example, in many historic structures built in the latter part of the 19th century three plaster layers were used consisting of the base or scratch-coat layer (also called Trullisatio), the middle or brown coat layer (also known as Arriccio), and the finish or white coat layer (also called Intonacco). By simple extension of the analysis leading up to Eq. (25), when the detachment involves *delamination* between two of these layers, one can show that an appropriate modification of Eq. (25) would be

$$\frac{W_C}{W} \sim \frac{3(1+\sigma^2)a}{tt_1^3} \tag{28}$$

where t_i is to be interpreted as the distance between the outer plaster surface and the delamination and we have assumed that the elastic parameters and thicknesses of the layers are the same. Since t_i is by definition less than t, smaller delaminated sections can be visualized directly. For example, for delamination of the innermost or outermost layers the discernable defect size shrinks by factors of 2.3 and 1.4, respectively.

Deconsolidation Defect

Next, we consider the second defect type, *viz.* plaster deconsolidation here modeled as a heavy fluid pocket with a somewhat smaller compressibility than the consolidated plaster. The dynamic displacement maps calculated with the finite element code are shown in Fig. 32b in the area around the flaw. The displacement levels associated with the deconsolidated segment are again seen to be much larger than those associated with the unflawed regions of the ceiling although somewhat smaller than for the detached case. Thus this defect can also be detected and localized merely by observing the displacement map itself.

As can be seen in Fig. 32b, the surface response for the fluid defect case oscillates spatially as one goes over the defect. This is in contrast to what we observed for the detached layer where the spatial response pattern fell off monotonically from the center of the flaw (Fig. 32a). Also, we show in the next section the spatial wavenumber spectra obtained by application of our newly developed transform. Although the origin of this effect is unclear at the present time, we point out that this feature may provide one the ability to distinguish between detached segments and deconsolidated defects, and this is currently under further investigation.

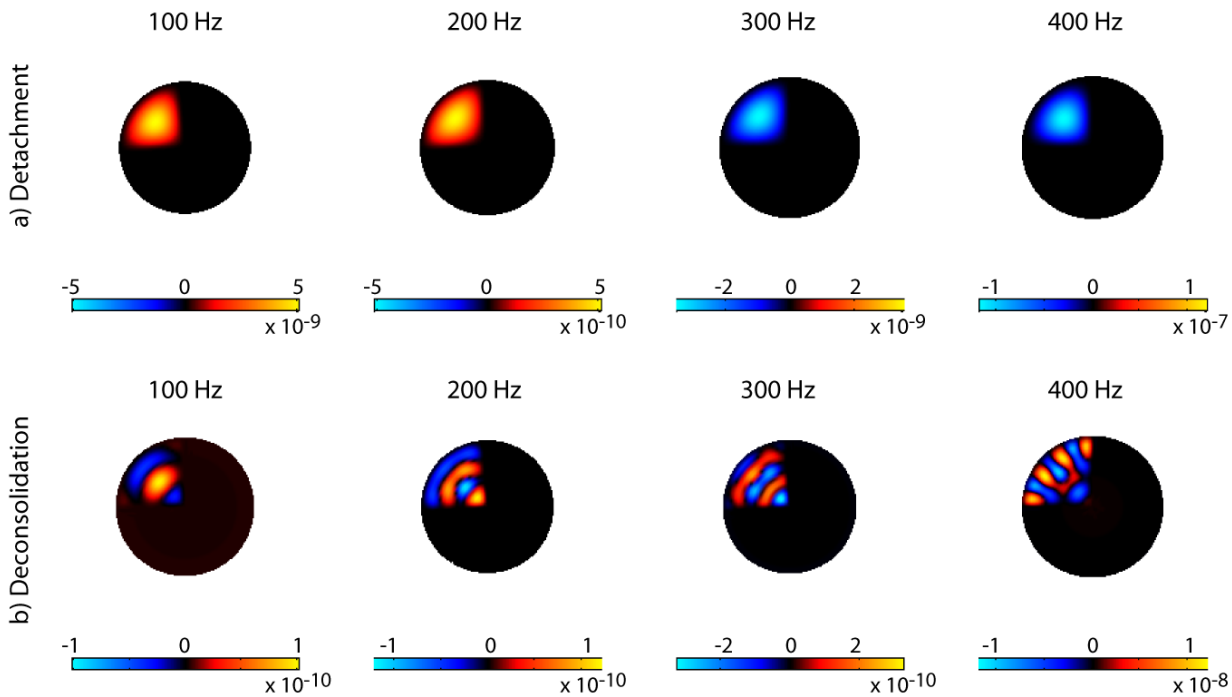

Figure 32. Normal displacement levels for the flawed ceiling in an area around the flaw calculated with the STARS3D code for four frequencies (displayed on the exposed surface of the ceiling): (a) detached flaw; (b) deconsolidated flaw.

One explanation we considered for this spatial variation of the surface displacement across the deconsolidated pocket is the following. As shown in Table 3, the flexural wavelength λ_{flex} in the 2.54 cm plaster plate is 0.9 m at 400 Hz. Beneath the deconsolidated segment, the plaster layer thickness is reduced by a factor of three; and since λ_{flex} varies as $t^{1/2}$, it becomes ~ 0.5 m in the lower plaster layer. The defected segment is now of order λ_{flex} on a side, and this could result in a pseudo standing wave spatial modulation. However, closer examination of Fig. 32b indicates much larger wavenumbers (smaller wavelengths) associated with the displacements beneath the defect than expected for the flexural wavenumber at these frequencies. This mismatch would seem to indicate that the effect is tied more to the response of the fluid layer itself than the plaster layer above it.

Findings from Ceiling Study

(1) We have demonstrated that even relatively small defects result in large displacement levels which stand out against those of the healthy plaster. But can those displacement levels be detected by a typical laser vibrometer? We find that indeed even away from defect resonances, practical levels of speaker excitation produce easily measured defect surface vibration. For example, scaling our finite element-based simulations predicts that a 74 dB SPL speaker source (0.1Pa) located ~ 2.4 m beneath the ceiling at 300 Hz produces a displacement on the order of 4.3×10^{-10} m (8×10^{-7} m/s velocity) beneath a detached pie-shaped segment of radius 0.5 m and area roughly 0.2m^2. Commercially available laser vibrometers (e.g. the Polytec PSV 400) have minimum detectable levels $< 5 \times 10^{-12}$ m/√Hz in this frequency range. Over a 1 Hz bandwidth, this corresponds to a minimum measurable displacement of $< 5 \times 10^{-12}$ m which is about a factor of 100 below the predicted defect displacement levels mentioned above. Recognizing that the defect displacement levels are proportional to the square of the defect area (see Eq. (23)) implies that defects as small as 0.15 m (2a for the circular defect) should have displacement levels which are detectable with such a system. Increasing the source level to 100 dB SPL would allow 0.07 m flaws to be detected at 300 Hz. Also, since the Doppler vibrometer measures velocity which is $\omega \times$ displacement, one could achieve still improved performance by increasing the frequency.

These minimum size estimates have assumed a plaster layer thickness of 0.0254 m which is fairly common. Since detachment displacements are proportional to t^{-3} (see Eqs. (23) and (24)), even slightly thinner detached layers would have much higher displacements. For example, for a 25 % thickness reduction, the detachment displacement levels increase by a factor of 2.4. Finally, we point out that if the delamination happens between the first and second or second and third layers, significantly smaller detachment sizes should have sufficient contrast and also be detectable (see Eq. (28)).

(2) Unlike the use of locally applied shaker excitation, the architectural acoustics of the room (walls and ceilings) must be taken into account. On the positive side, however, the plane-like waves from the speaker excite far fewer elastic excitations and modal responses in the plaster ceiling layer compared to that generated by the high spatial wavenumbers of the locally applied force of the shaker.

(3) For both the defect types and size simulated here (~ 0.5 m pie-shaped segment of detachment from the supporting structure and plaster deconsolidation), the displacement levels are considerably higher than those of the healthy plaster layer so that these flaws should be detectable by mere observation of the vibration maps.

(4) In general, the directly observable (sufficiently contrasted) minimum defect size is found to be less than 2 times the plaster layer thickness. For a typical plaster ceiling of 2.54 cm thickness, detachment segments with diameters (circular flaw) or radii (pie-shaped flaw) somewhat smaller than 10 cm should be sufficiently contrasted and thus directly observable. Much smaller sizes should nevertheless be accessible by post-processing of the displacement maps using for example successfully reported inversion operators (Bucaro, et. al.[4]) or by increasing the acoustic frequency. For delamination in ceilings comprised of several layers, and

probably for an internal pocket of deconsolidated plaster as well, these directly observable defect sizes are reduced considerably.

(5) In the frequency range studied here (100 Hz to 400 Hz), the spatial structure in the displacement maps beneath the defect may provide a wavenumber-based feature which could separate plaster detachment from the other types of defects such as deconsolidation.

Novel Spatial Transforms for Arbitrarily-Shaped Surfaces

Most of the tools (both standard as well as specialized) for understanding the relations between sound, elastic vibration, and structural detail exploit knowledge about wavenumber space (spatial Fourier analysis) and the extrapolation of wavefields from one surface to the other[5].

Up to now, the application of Fourier decomposition and analysis and the powerful techniques based upon them have been restricted to separable geometries (planes, spheres, cylinders, etc.). This is primarily because the Fourier kernels (and their corresponding basis functions) for the spatial transforms of these simple geometries provide a direct and physical interpretation of the vibrational behavior. For non-separable geometries, however, such a direct interpretation has not been available.

In the past, efforts to adapt simple Fourier decompositions to accommodate more complex structures have involved rather ad hoc remedies. These include, for example, the approximation of complex, curved structures with locally planar, piecewise continuous transform "elements" (or plates), and the axial "weighting" of the radius within a cylindrical transform as an estimation for the transforms along conical and ellipsoidal structures. Although these representations seemed logical and provided particular feature spaces, their physical interpretations were left to speculation and they did not provide a direct analysis and interpretation of the vibrational fields in a conformal wavenumber spectrum.

We have now developed a powerful new method[17] which enables two-dimensional spatial Fourier decompositions on parameterized C^1 surfaces. This is an extension of our previous work in Waveguide Constrained Magnetic Resonance Elastography[29], wherein we performed dispersion analysis along particular fiber pathways within a tapered waveguide. That study was able to extract spatially dependent velocities of propagation even though the material comprising the structure did not vary significantly throughout. We have now extended this development to surfaces.

In Ref. (17) we give the detailed theoretical development of this approach from fundamental principles using differential geometry and demonstrate how the Fourier transform representations of some simple geometries can be recovered. As a test case, we have also developed the particular form of this generalized transform applicable to a conical surface, and we analyzed the vibration of a point driven, fluid loaded conical structure whose displacements and pressures were calculated using the finite element method.

This new, general transform capability can be applied directly to our fault detection and localization method as it allows us to analyze dispersion behavior on a surface or structure irrespective of its shape. This leads to an important augmentation of our ω - k mapping[5] technique (although we have not yet applied it here) in which local differences in the dispersion curves from those observed or expected in unflawed structures indicate variations in wave types or in their speeds which are directly related to material parameter variations associated with the development of flaws. We also anticipate that this new transform approach will lead to heretofore unexploited spectral features for classification and vibration analysis. In this regard, we applied this new transform to the spatial displacement maps associated with the two flaw types studied in the elliptical dome plaster ceiling study.

We used this new transform machinery to obtain the k_x,k_y wavenumber spectra associated with the two flaw types in our elliptically-shaped ceiling having the displacement x,y maps shown in Fig. 32 at the four frequencies. This was accomplished by taking the general expression for the forward conformal transform from Ref. 17 and expressing it in ellipsoidal coordinates. Over the patch, we defined the wavenumbers as k_ϕ (ϕ being in the circumferential direction) and k_θ (θ being in the vertical direction, i.e. top to bottom along the ellipsoid). We also defined k_ϕ as being $(2 \times n \times \pi)/(2 \times \pi \times c \times \sin(\theta))$, c the height of the ellipsoid, and k_θ as being $(2\times m \times \pi)/(20 \times a \times d\theta)$, a the radius of the base of the ellipsoid (being equal to b), and 20 is the number of spatial locations along the θ direction providing the total arclength from top to bottom of the flaw. Therefore, k_ϕ varies with respect to the angle, θ, yet is pointed in the phi direction (around the circumference of the ellipsoid). k_θ does not vary with respect to angle but is pointed in the θ direction (top to bottom). We then performed the integral transforms with these kernals and appropriate surface areas, and the resulting wavenumber spectra are displayed in Figs. 33 and 34 labeled with the indices n and m.

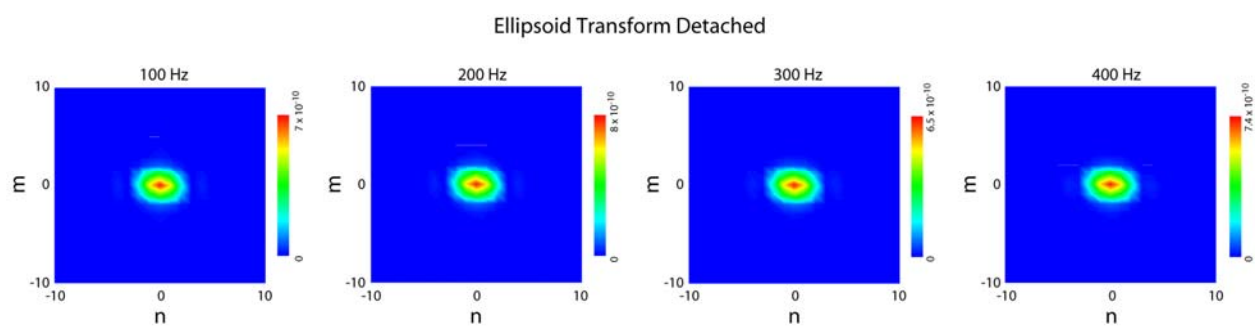

Figure 33. New spatial transform applied to the detached ceiling flaw.

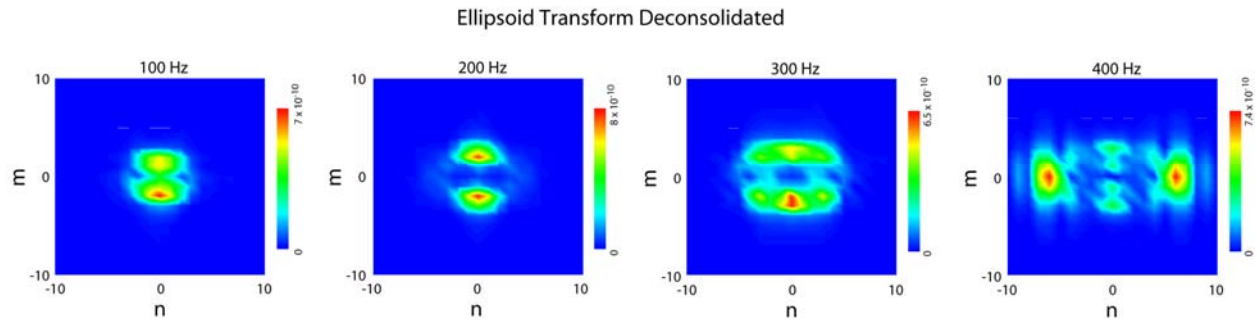

Figure 34. New spatial transform applied to the deconsolidated ceiling flaw.

As can be observed, for the detached flaw, each of the transforms has only one dominant $k_\phi = k_\theta = 0$ component. This implies that there is essentially no modal structure and the patch is simply moving uniformly back and forth, irrespective of frequency.

For the deconsolidation, however, as can be seen in Fig. 34 there is different modal structure at each frequency. For 100 Hz, the transform shows that there is only a $k_\phi = 0$ (n = 0) component, meaning that the mode shape is constant over the flaw with respect to the circumferential direction, ϕ, while there is a standing wave or sorts in the θ direction, with k_θ having two wave components for m = -2, and m = +1. For 200 Hz, again, the dominant mode in the ϕ direction is $k_\phi = 0$ (n = 0), meaning that the wave is constant with respect to ϕ, while k_θ has two dominant wavenumber components for m = -2 and m = +2, representing a standing wave along the θ direction. For 300 Hz, the transform image is somewhat smeared around the ϕ direction, with dominant modes for k_ϕ appearing at n = -3, 0, and +3, representing a standing wave in the ϕ direction and the modal structure can be seen in the images. In the θ direction, these k_ϕ modes can be seen to be coupled with the k_θ modes of m = -2 and +2, as for the 200 Hz case. For 400 Hz, there are some residual wavenumber components for k_θ at the modes m = -3, -1, and +1, +3, coupled with $k_\phi = 0$ (n = 0), while another set of modes is coupled at $k_\theta = 0$ (n = 0) with k_ϕ modes n = -6 and +6. While there do not appear to be 6 complete waves within the displacement image around the circumference, the transform implies that the resulting field is composed of all of these modes.

While at the present time, we have not gone further in using the spatial transforms to understand more clearly the dynamic response associated with the deconsolidated inclusion, clearly the differences in these transforms and their related features can be used to differentiate in a formal way between the two types of flaws.

Laboratory Demonstration

The experimental component of this program focused on application of our LDV-based approach to the study of a long 2” × 10” ceiling support beam in which was created an internal 2” × 2.5” × 5/8” thick defect at its mid-plane filled with saw dust which approximated decay or

termite-like damage to the wood (see Fig. 35). In addition, a similar smaller 1” × 1.25” defect was also included. Of all the cases studied in the numerical component of this SEED program, the wood beam case represents the most challenging owing to the orthotropic nature of the material. In addition, although we have in the past carried out experimental structural acoustic work in a number of other materials, we had not done so for wood. For convenience, we used an available 2” × 10” untreated Douglas fir beam which is typical of what one would find at a home building supply store.

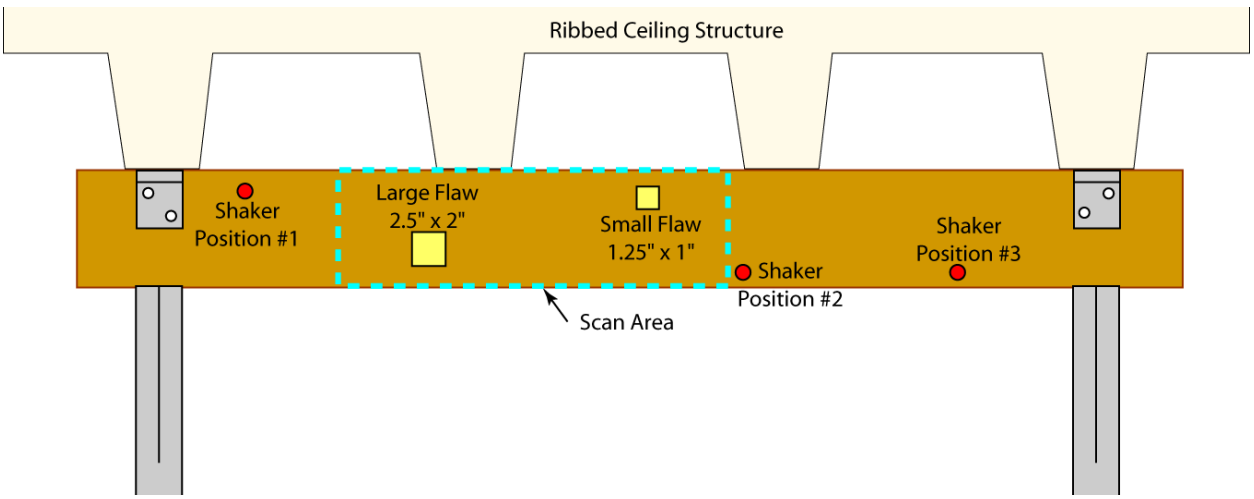

Figure 35. Drawing of beam with faults, shaker, and scan area locations. This view is from SLDV side. Shakers actually mounted on backside of beam.

Broadband SLDV scans were obtained across one surface of the wooden beam (side opposite the shaker) providing dynamic normal velocity (derivative of displacement) fields in the usual manner. A photograph of the laboratory set-up is shown in Fig. 36. In the background, one can see the tripod-mounted Polytech SLDV. A separate photograph of the SLDV is shown in Fig. 37.

The structural response was measured for three cases due to point force excitation applied by a 1 lb-force Wilcoxon F3/F9 shaker attached sequentially at three separate locations on the beam as shown in Fig, 35. The shaker #1 location is ~17.0 cm from the left edge of the scan, and shaker #2 and #3 locations are ~1.6 cm and ~ 60 cm from the right edge of the scan, respectively. The shaker contains both an electromagnetic and piezoceramic element to generate force over the entire frequency band of interest. One of the mounted shakers can be seen in photograph in Fig. 36. The force normalized measurements were conducted using a chirp waveform which covered a band from 200 to 10000 Hz with 1.6 Hz resolution. The wooden experimental beam was loaded by two jack screw bars which pushed it up against ribbed concrete ceiling supports. The highly spatially sampled scans for the flawed beam consisted of 47 vertical and 209 horizontal points, yielding a total of 9823 measurement locations. The measurements were made with 4.3 mm spatial resolution over a 0.2 × 0.9 m scan area which included the two flaws. The

typical signal-to-noise ratio (SNR) varies from approximately 50 dB at low frequency near the shaker #1 location to approximately 15 dB at the high end of the frequency band near the far end of the scan area away from the shaker.

Figure 36. Laboratory study of flawed wooden support beam. Scanning laser Doppler vibrometer shown in background. Dynamic shaker mounted on upper right corner of beam. Larger interior flaw depicted by rectangle drawn on beam.

Figure 37. Polytec Inc. PSV-400 laser Doppler vibrometer scanning head.

Three examples of the LDV scanned measurement results are shown in Fig. 38 for 431.25 Hz, 1260.94 Hz, and 7162.50 Hz. The displays show the magnitude of the normal surface response level in (meter/second)/Newton over the scanned area for each frequency. The modal structure of the beam at 431.25 Hz has approximately 2 half wavelengths along the length of the beam (horizontal in display) and one half wavelength across the width (vertical in display). At 1260 Hz, ~4 half wavelengths are found in the length direction and 1 to 2 half wavelengths in the width direction, and the modal structure at 7162.50 Hz shows much higher mode numbers. The very small dots observed in the display at 7162.50 Hz are believed to be real very local responses

due to the non-homogenous nature of the beam. It should also be noted that the SNR is reduced at this higher frequency.

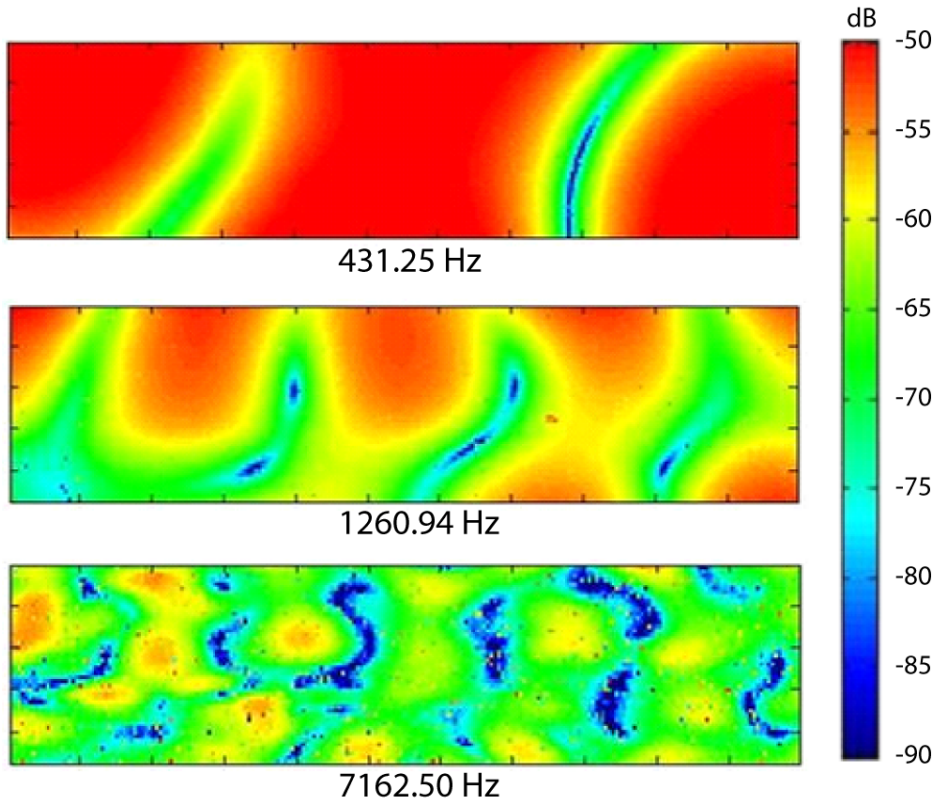

Figure 38. Normal surface velocity ((m/s)/N) magnitude displays at 431.25 Hz, 1260.94 Hz, and 7162.50 Hz. The horizontal dimension is along the length of the flawed beam and the vertical dimension is across the width of flawed beam

The broadband data bases were analyzed in two ways: direct observation of the displacement maps in search of high contrast motion and application of the orthotropic thin plate inversion algorithm. First, the displacement maps were examined without any inversion to determine if the defect was observable by direct observation of the contrast in the spatially mapped displacements. As discussed by Bucaro et. al.[1] and Vignola et. al.[3], direct observation is most effective when the displacement maps are first averaged over appropriate frequency bands in order to remove the artifacts caused by the frequency dependent modal response structure of the beam itself. (See the modal patterns in Fig. 38.) When this is done, the internal defect is clearly visible as is shown in the maps in Fig. 39. The lower display has been magnitude averaged over the entire band while the upper display over the band 7600 Hz to 8000 Hz. The artifacts in the upper left corner are associated with the shaker itself. In an actual fault assessment exercise, the region around a shaker would automatically be ignored.

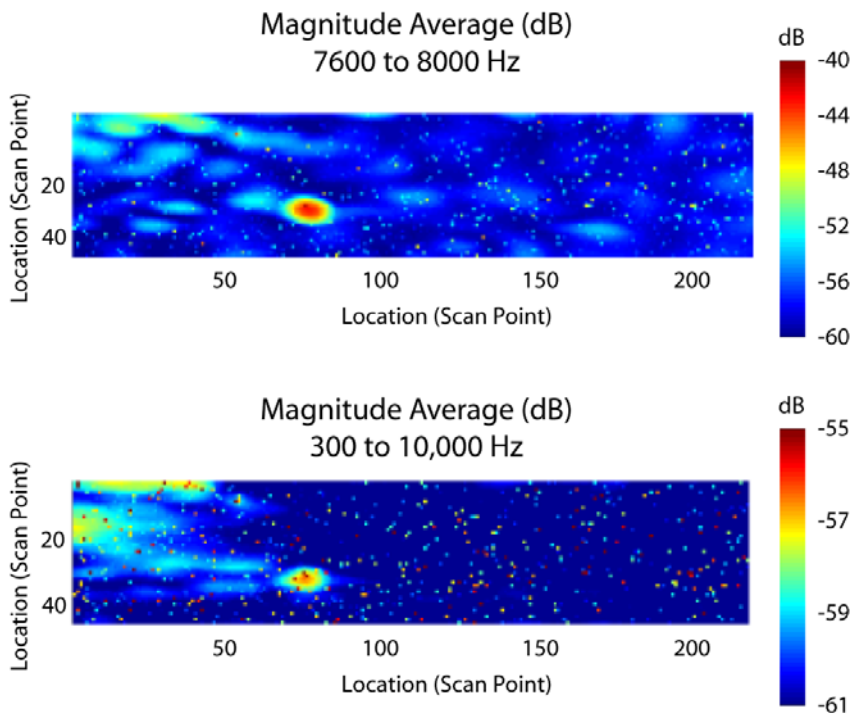

Figure 39. Band averaged displacements. Lower display is average over complete band; Upper display is average over resonance band. The defect centered at about scan point 80 is clearly evident in both maps.

We can estimate the frequency at which there would be a resonant response at the flaw by calculating the frequency at which there would be one half a flexural wavelength across the flaw. We estimate this to be at about 8 kHz where the flexural wavelength in the wood layers above and below the fault would be twice the flaw size, and this is in agreement with the strong flaw response we see at 7900 Hz in Fig. 40 below.

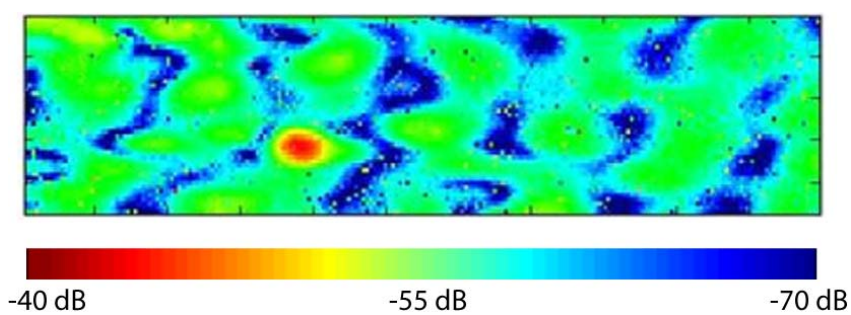

Figure 40. Direct displacement at 7900 Hz showing flaw.

Using similar reasoning to that leading up to Eqs. (22)–(25) for an *acoustically excited* ceiling flaw, we can intuit that the contrast ratio for the displacement levels of the wood away from the flaw to that over the flaw for *shaker excitation* would be simply approximated by the cube of the ratio of wood thickness to flaw depth. This would predict a vibration level contrast

ratio of $(1.6''/0.8'')^3$ = 8 or 18 dB. Since the red spot in Fig. 40 is 15 dB above the green level, this simple estimate appears to be valid.

Turning to the smaller defect, we estimate the resonance frequency to be double that of the larger defect, i.e. ~ 16 kHz, which is well above our current measurement band. Thus we would not expect to be able to observe this defect by direct observation of the displacement maps which indeed turns out to be the case.

Next, we applied the orthotropic inversion operator to the three displacement fields generated by the three shakers excited one at a time according to the expressions indicated in Eq. (8). The inversions for the three stiffness parameters $D_x/\rho h$, $D_{xy}/\rho h$, and $D_y/\rho h$ are shown in Fig. 41 for 8609 Hz. As can be seen, where we were expecting a uniform stiffness mapping across the beam we instead see a significant variation. This is in contrast to the orthotropic inversions shown earlier in Fig. 18 for the numerical simulation of a homogeneous wooden slab. For example, the inversion maps for the real wood beam show fluctuations in $D_y/\rho h$ that range from about 2 to 2000 Pa m^5kg^{-1} whereas for uniform Douglas fir we would have expected a constant value of 1100. Also, we fail to see either flaw impression on this map.

This result is under further investigation. At the current time, we do not believe the problem is associated with unknown measurement system issues such as noise or operation of the LDV. We are exploring the possibility that these fluctuating stiffness maps are in fact correct and are due to the poor wood quality of our support beam.

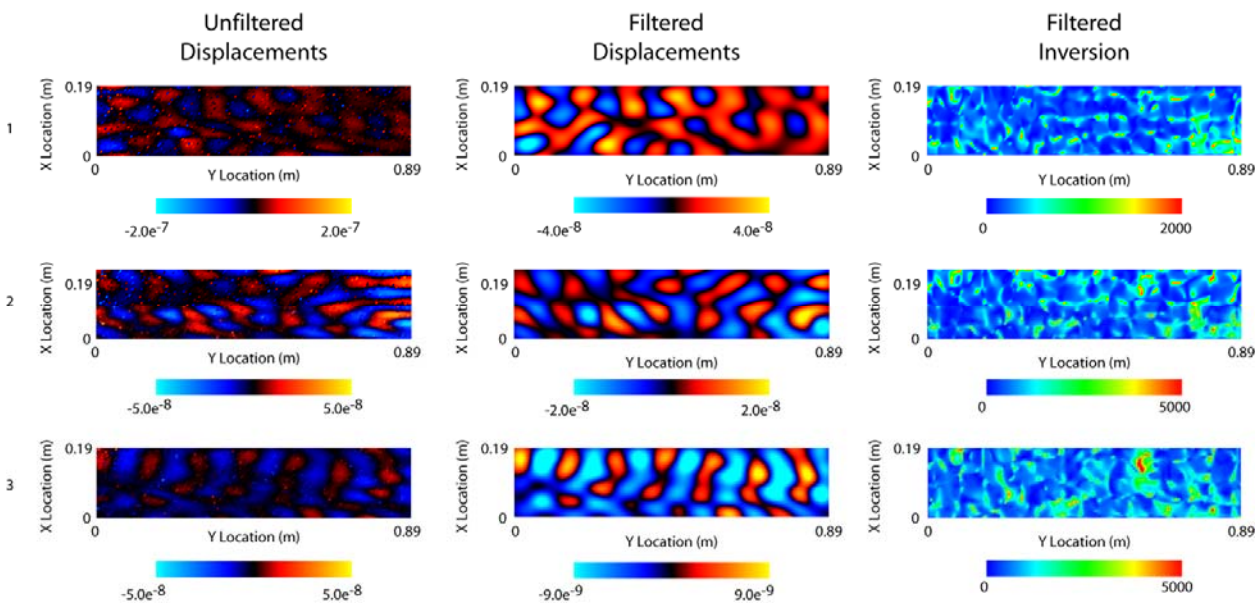

Figure 41. Displacement (left) and filtered displacement (middle) for the three shaker positions. Orthotropic inversion of displacement data for (right) for D_x/ph, D_{xy}/ph, and D_y/ph on top, center, and bottom, respectively.

Conclusions

The multi-pronged progress in this SEED effort detailed above represents a significant advance in the capability and applicability of our structural acoustics-based fault detection and localization approach using laser measured surface vibration. In particular:

The successful numerical studies on plates of differing materials – plaster, steel, concrete, and wood – indicate that our approach can be effective on structures and fabrics made of various materials in an historic building.

In the particular case of wood, our numerical studies confirm that our orthotropic inversion operators are valid. This, together with earlier results we had obtained experimentally on framed graphite-epoxy composite plates indicates that our technique can also be effective on more complex orthotropic and anisotropic materials and structures.

Again for wood, our experimental study on a Douglas fir wooden support beam demonstrated the ability of direct observation of laser measured surface vibration to detect and locate an internal defect simulating termite damage. The inversion operator, however, produced a beam stiffness spatial map with large fluctuations. Further work is required to validate that these variations are indeed correct.

The successful numerical study on thick plates with various fault depths demonstrates that at least up to modest thicknesses, we can detect both flaws close to the surface as well as much deeper defects. Heuristic post analysis can allow one to infer the defect depth, but further work should be done to develop algorithms that can do so directly.

Two powerful advances were achieved in adaptive inversion. The first was achieved by operating two algorithms in sequence to overcome incomplete knowledge of the equations of motion for the structure. In a numerical demonstration for the case of a thick plate for which the thin plate equations were no longer valid, application first of the thin plate inversion operator on the displacement data followed by the application of the generalized force operator with the material parameters as determined by the inversion first inserted produced very clear maps showing the internal flaws. The second approach introduces general high order equations of motion with unknown coefficients which are adaptively identified using the measured displacement data and a normalized variance test. We validated this approach using existing magnetic resonance elastography data on agar tissue phantoms and numerical data on isotropic and orthotropic plates. The next step here would be an experimental demonstration on a general structure.

There was insufficient time available to explore the potential for modern day classifiers such as relevance vector machines and hidden Markov models to detect the presence of a flaw based on robust features present in the displacement signals. Our original plan was to carry out this study using the numerically generated data bases. Subsequently we realized that a superior way to study this time-frequency feature-based problem is using broadband displacement data. Given that our advanced finite element codes are frequency-based, such a study would be prosecuted most efficiently using experimentally generated broadband data.

The plaster dome ceiling study was very productive. We have provided the first (to our knowledge) models allowing one to predict flaw size detectability or to generalize to different conditions for our general surface vibration approach. We have demonstrated that even relatively small defects result in large displacement levels which stand out against those of the healthy plaster and that even away from defect resonances, practical levels of speaker excitation produce easily measured defect surface vibration. Defects as small as 0.07 m (2a for the circular defect) should have displacement levels which are detectable with commercially available laser vibrometers. Unlike the use of locally applied shaker excitation, when using speakers the architectural acoustics of the room (walls and ceilings) must be taken into account. In the frequency range studied here, the spatial structure in the displacement maps beneath the defect may provide a wavenumber-based feature which could separate plaster detachment from the other types of defects such as deconsolidation.

We have now developed a powerful new method which enables two-dimensional spatial Fourier decompositions on parameterized C^1 surfaces. This new, general transform capability can be applied directly to our fault detection and localization method as it allows us to analyze dispersion behavior on a surface or structure irrespective of its shape. This leads to an important augmentation of our ω - k mapping technique in which local differences in the dispersion curves from those observed or expected in unflawed structures indicate variations in wave types or in their speeds which are directly related to material parameter variations associated with the development of flaws. We also anticipate that this new transform approach will lead to heretofore unexploited spectral features for classification and vibration analysis. In this regard, we applied this new transform to the spatial displacement maps associated with the two flaw types studied in the elliptical dome plaster ceiling study.

In the concluding laboratory-based study for this SEED program, we successfully detected an interior defect (thin, small sawdust-filled cavity) in a 2" × 10" wooden ceiling support beam by direct observation of the laser measured surface displacement maps. Subsequent inversions of the displacement maps indicated large fluctuations in the beam stiffness properties, and these results are still under investigation.

References:

1. J.A. Bucaro, J. Vignola, B. H. Houston, and A. J. Romano, "Preliminary Observations Regarding LDV Scans of Panels Excited by Broadband Actuators at the U.S. Capitol," NRL Memo Report 7130--03-865, 2003.
2. J. A. Bucaro, J. F. Vignola, and A.J. Romano, "Fault Detection and Localization Using Laser-Measured Surface Vibration," NRL Review, 81-89, 2005.
3. J.F. Vignola, J. A. Bucaro, B. R. Lemon, G.W. Adams, A.J. Kurdila, B Marchetti, E. Esposito, E. Tomasini, H.J. Simpson, and B.H. Houston, "Locating Faults in Wall Paintings at the U.S. Capitol by Shaker-Based Laser Vibrometry," APT Bulletin, The J. Preservation. Tech. 36, 25-33, 2005.

4. J.A. Bucaro, A.J. Romano, P. Abraham, and S. Dey, "Detection and Localization of inclusions in plates using inversion of Point Actuated Surface Displacements," J. Acoust. Am. 115, 201-206, 2004.
5. E. G. Williams, Fourier Acoustics: *Sound Radiation and Nearfiled Acoustic Holography*, Academic Press, San Diego, CA, 1999.
6. B. A. Wolanin, *Constantino Brumidi: Artist of the Capitol*, U.S, Government Printing Office, Washington, DC, 1998.
7. A.J. Romano, J.A. Bucaro, J.F. Vignola, and P.B. Abraham, "Detection and Localization of Rib Detachment in Thin Metal and Composites Plates by Inversion of Laser Doppler Vibrometry Scans," J. Acoust. Soc. Am., 121, 2667-2672, 2007.
8. A.J. Romano, J.A. Bucaro, R.L. Ehman, and J. J. Shirron, "Evaluation of a Material Parameter Extraction Algorithm Using MRI-Based Displacement Measurements," IEEE Tran. Ultrason. Ferroelectr. Freq. Control 47, 1575-1581, 2000.
9. A.J. Romano, J.A. Bucaro, B.H. Houston, J.L. Kugel, P.J. Rossman, R.C. Grimm, and R.L. Ehman, "On the Feasiblity of Elastic Wave Visualization Within Polymeric Solids Using Magnetic Resonance Elastography," J. Acoust. Soc. Am. 116, 125-132, 2004.
10. J. A. Bucaro, B. H. Houston, H. J. Simpson, and T. J. Yoder, "Exploitation of Acoustic Target Characteristics for Mine Classification and Identification," J. Underwater Acous., 47 (2), pp. 775–794, Apr 1997.
11. L. Carin, H. Liu, T. Yoder, L. Couchman, B. Houston and J. Bucaro, "Wideband Time-reversal Imaging of an Elastic Target in an Acoustic Waveguide," J. Acous. Soc. Am. 115(1 2), January 004
12. N. Dasgupta, P. Runkle, L. Carin, L. Couchman, T. Yoder, J. Bucaro, and G. Dobeck, "Class–based Target Identification with Multi–Aspect Scattering Data," IEEE Journal of Oceanic Engineering, May 21, 2001
13. P. Runkle, L. Carin, L. Couchman, T. Yoder, and J. Bucaro, "Multi–aspect Identification of Submerged Elastic Targets via Wave–based Matching Pursuits and Hidden Markov Models," J. Acous. Soc. Am.,. 106, pp. 605–616, Aug. 1999
14. P. Runkle, L. Carin, L. Couchman, T.J. Yoder, and J.A. Bucaro, "Multi–aspect Target Identification with Wave-based Matching Pursuits and Continuous Hidden Markov Models," IEEE Trans. Pattern Analysis and Machine Intelligence, 21, pp. 1371–1378, Dec. 1999.
15. P. Castellini, N. Paone, and E.P.Tomasini, "Application of a laser Doppler vibrometer to nonintrusive diagnostic of fresco damage," Proc. of the First International Conference on Vibration Measurements by Laser Techniques: Advances and Applications, Ancona, Italy,SPIE, Vol. 2358, 70-77, 1994.
16. V. Tornari, A. Bonarou, P. Castellini, E. Esposito, W. Osten, M. Kalms, N. Smyrnakis, and S. Sasinopulos, "Laser-based systems for the structural diagnostics of artworks: An application to XVII –century Byzantine Icons," Proceedings of Laser Techniques and Systems in Art Conservation Conference, 172-183, 2001.
17. A.J. Romano, P.B. Abraham, N.P.Valdivia, B.H. Houston, J.A. Bucaro, and S. Dey, "Conformal Fourier Wavenumber Decompositions on Paramatrizable C^1 Surfaces," Accepted for Publication, J. Acoust. Soc. Am., 2009.
18. A. Leissa, "*Vibration of Plates*," Acoust. Soc. Am. Pub. ISBN-1-56396-294-2, 1993.
19. P.C. Hansen, "*Rank-Deficient and Discrete Ill-Posed Problems*," SIAM, Philadelphia, PA., 1998.

20. D.W. Green, J.E. Winandy, and D.E. Kretschmann, "Mechanical properties of wood," in Wood Handbook:Wood as an Engineering Material, USDA Forest Service, Forest Products Laboratory,GTR-**113**, Chap. 4, 1-45, 1999.
21. B. Hosten, B."Reflection and transmission of acoustic plane waves on an immersed orthotropic and viscoelastic solid layer," J. Acoust. Soc. Am. **89**, 2745-2752, 1991.
22. V.Bucur, "Acoustics as a Tool for the Nondestructive Testing of Wood," 1999. NDTISS'99 Int. Symp. on NDT Contribution to the Infrastructure Safety Systems.
23. R. Kerlin, "Internal Friction Studies on Bell Metal and Wood," Technical Memorandum No. TM603.2811-05, Penn. State Univ., 28-50, 1966.
24. S. Dey and D.K. Datta, "A parallel hp-FEM intrastructure for three-dimensional structural acoustics," Int. J. Num. Meth. Eng., **68**, 583-603, 2006.
25. E. Skudrzyk, E., "*Simple and Complex Vibratory Systems*," The Pennsylvania State University Press, University Park, PA, 200-214, 1968.
26. L. Cremer and M. Heckl, M., "*Structure-Borne Sound*," Springer-Verlag, New York, 109-115, 1988.
27. S. Dey, J.J. Shirron, and L.S. Couchman, "Mid-frequency structural acoustic and vibration analysis in arbitrary, curved three-dimensional domains," Computers and Structures, 79, 617-629, 2001.
28. Warren C. Young, "Roark's formulas for stress and strain," McGraw-Hill, 1989.
29. A.J. Romano, P.B. Abraham, P. J. Rossman, J.A. Bucaro, and R.L. Ehman, "Determination and Analysis of Guided Wave Propagation Using Magnetic Resonance Elastography," Magn Reson Med., 54, 893-900, 2005.

X. Appendices

(A) Supporting Data - NA

(B) List of Technical Publications

Anthony J. Romano, Joseph A. Bucaro, and Saikat Dey, "Defect detection and localization in orthotropic wood slabs by inversion of dynamic surface displacements," J. Acoust. Soc. Am., 124, 918-925, 2008.

A.J. Romano, P.B. Abraham, N.P.Valdivia, B.H. Houston, J.A. Bucaro, and S. Dey, "Conformal Fourier Wavenumber Decompositions on Paramatrizable C^1 Surfaces," Accepted for Publication, J. Acoust. Soc. Am., 2009.

J.A. Bucaro, A.J. Romano, N. Valdivia, B.H. Houston, and S. Dey, "A numerical study of defect detection in a plaster dome ceiling using structural acoustics, in review, J. Acoust. Soc. Am.

(C) Other Technical Material- NA